The Influence of Surface Films on Interfacial Flow Dynamics

by

Sean Patrick McKenna

B.S. Mechanical Engineering, Rensselaer Polytechnic Institute (1993)

Submitted to the Department of Applied Ocean Physics and Engineering, WHOI
and the
Department of Ocean Engineering, MIT
in partial fulfillment of the requirements for the degree of

MASTER OF SCIENCE IN OCEANOGRAPHIC ENGINEERING

at the

MASSACHUSETTS INSTITUTE OF TECHNOLOGY

and the

WOODS HOLE OCEANOGRAPHIC INSTITUTION

June 1997

© Massachusetts Institute of Technology, 1997.
All rights reserved.

Author .....
Department of Applied Ocean Physics and Engineering, WHOI
Department of Ocean Engineering, MIT
May 9, 1997

Certified by .....
Dr. Erik J. Bock
Associate Scientist, WHOI
Thesis Supervisor

Accepted by .....
Prof. Henrik Schmidt
Chairman, Joint Committee for Oceanographic Engineering
Massachusetts Institute of Technology/Woods Hole Oceanographic Institution

JUL 15 1997 Eng.

The Influence of Surface Films on Interfacial Flow Dynamics

by

Sean Patrick McKenna

Submitted to the Department of Applied Ocean Physics and Engineering, WHOI
and the
Department of Ocean Engineering, MIT
on May 9, 1997, in partial fulfillment of the
requirements for the degree of
Master of Science in Oceanographic Engineering

Abstract

Surface films, or surfactants, are ubiquitous in the ocean environment. In light of this fact, a firm understanding of how these films affect near-surface ocean processes is desirable. A surface film exhibits viscoelastic properties when subjected to dynamic compression and dilation. This viscoelastic response manifests itself by modifying the interfacial boundary conditions leading to a modification of the underlying bulk flow. In this thesis, the influence of surface films on capillary–gravity waves and near-surface vortex flow is studied. An uncontaminated free surface, several monolayers, and a solid boundary were selected for investigation. In the case of wave dynamics, a two-phase dispersion relation is derived that governs the propagation of capillary and capillary–gravity waves at an interface between two viscous media with a finite interfacial dilational elastic modulus. We present theoretical results that show wave damping enhancement for surfactant adsorbed water surfaces over that of a perfectly clean water condition. A complimentary experimental investigation making use of laboratory measurements of wavenumber and spatial wave decay for a range of surfaces yields results that are consistent with theory. In the case of a vortex flow impinging onto an interface, experimental work is performed that reveals, quantitatively, the effects of surface films on near-surface vortical motions. The behavior of the flow is dramatically altered due to the production of near-surface vorticity that arises from the absence of a free-slip interfacial condition.

Thesis Supervisor: Dr. Erik J. Bock
Title: Associate Scientist, WHOI

Acknowledgments

During the course of this thesis work, this author was supported as an Office of Naval Research Graduate Fellow. This assistance has proved to be invaluable, both financially and in terms of freedom of academic pursuit, and is gratefully acknowledged.

I am extremely thankful to have as my thesis advisor, Dr. Erik Bock. He has been a tremendous help to me in every aspect of my research activities. Beyond that, Erik has made this experience a rewarding one, and my time spent with him, both in and out of the lab, has been enjoyable. I am also grateful to have worked with Dr. Wade McGillis on many aspects of the DPIV technique used in this thesis. His time and effort are wholeheartedly appreciated.

I would like to thank Prof. Jerome Milgram of MIT for lending our lab an electro-balance that was used for the surface tension measurements. Additional thanks go to Dr. Nelson Frew of WHOI for supplying certain figures that appear in this text.

My fellow students have also been very helpful during my time spent at MIT and in the WHOI Joint Program. I value the friendships I have made here greatly. I would like to especially thank Steven Jayne for assistance with editing the final draft. Additionally, Jason Gobat has been a key source of information on a wide range of topics (usually computer related) that has been invaluable to me.

The support and love of my family has enabled me to accomplish all I have. For this I am very grateful. Lastly, I thank the person who carried me through the final weeks of this thesis. Without Jessica Rowcroft, my life would not be what it is today. I thank her dearly for all she has given and done for me.

Contents

List of Figures

List of Tables

Chapter 1

Introduction

1.1 Overview

The influence of surface films on the dynamics of near-surface vortex interaction has intrigued many researchers over the past two decades. Much effort, both experimental and numerical, has been directed toward better understanding this complex problem. This thesis adds to these efforts with experimental measurements of vortex-induced velocity fields in the presence of a free surface with finite viscoelasticity. Several different topics of research including ripple dynamics, vortex ring dynamics, and a still evolving flow measurement technique have been synthesized in order to relate the observed hydrodynamics to the surface rheology.

This contribution is a work in progress; significant effort has gone into the development and verification of the experimental techniques employed in this study. In this regard, data analysis is not the primary focus of the work presented here. Rather, it is the effective combination of several lines of experimental investigation that has formed the basis of this thesis.

1.2 Motivation

Surface-active agents, or surfactants, are ubiquitous in the ocean environment. Surfactants can be introduced into the marine surface layer through marine biological activity, petroleum

leaks or spills, coastal run-off, and offshore atmospheric deposition. The primary source is production by marine organisms, most notably phytoplankton, which exude natural surfactants as metabolic by-products. Additional surface-active materials are contributed via the degradation of deceased organisms and subsequent chemical and biological transformations. Figure 1-1 shows the distribution of ocean color in the North Atlantic. Ocean color is often used as an indicator of phytoplankton populations. Areas of green, yellow and orange are indicative of increasingly higher chlorophyll concentration. This figure attempts to make clear the nontrivial degree to which biogenic surfactants are present in the global oceans. The specific composition and concentration of surfactants in the marine microlayer is dependent upon several mechanisms such as local biological productivity, subsurface currents, internal waves, wind stress, wave state, and wave breaking [10].

Surface films, surface excesses of surface-active materials that preferentially exist at the air–water interface, have a profound impact on the dynamics of interfacial flows. The influence of surface films on both near-surface vortical flows and surface wave dynamics has been well studied. In both cases, it is the modification of the free-surface boundary condition due to the surfactant that is paramount to explaining the observed hydrodynamic behavior.

Characterizing the effects of surface films on wave motion, specifically capillary and capillary–gravity waves (or ripples), is important to many aspects of air–sea interaction because of the pivotal role these short waves play. Fluxes of heat, mass, and momentum across the air–sea interface are all influenced by surface waves. Estimating the transfer velocities of gases such as carbon dioxide and other climatically important gases, for example, has been the thrust of several research endeavors (*e.g.*, Frew *et al.* [23]; DeGrandpre *et al.* [16]). Figure 1-2 from the experimental work of Frew *et al.* [22] illustrates the role of surface film concentration on the mechanism of gas transfer.

Capillary–gravity waves also contribute to the effective surface roughness for the turbulent air-side flow above thereby affecting the air–sea momentum flux [48]. Hara [29] reports good correlation between mean-square wave slope, an indicator of surface roughness, and gas-transfer coefficients for waves on clean water surfaces. Another area in which capillary–gravity waves play a role is remote sensing of the ocean environment. Current remote

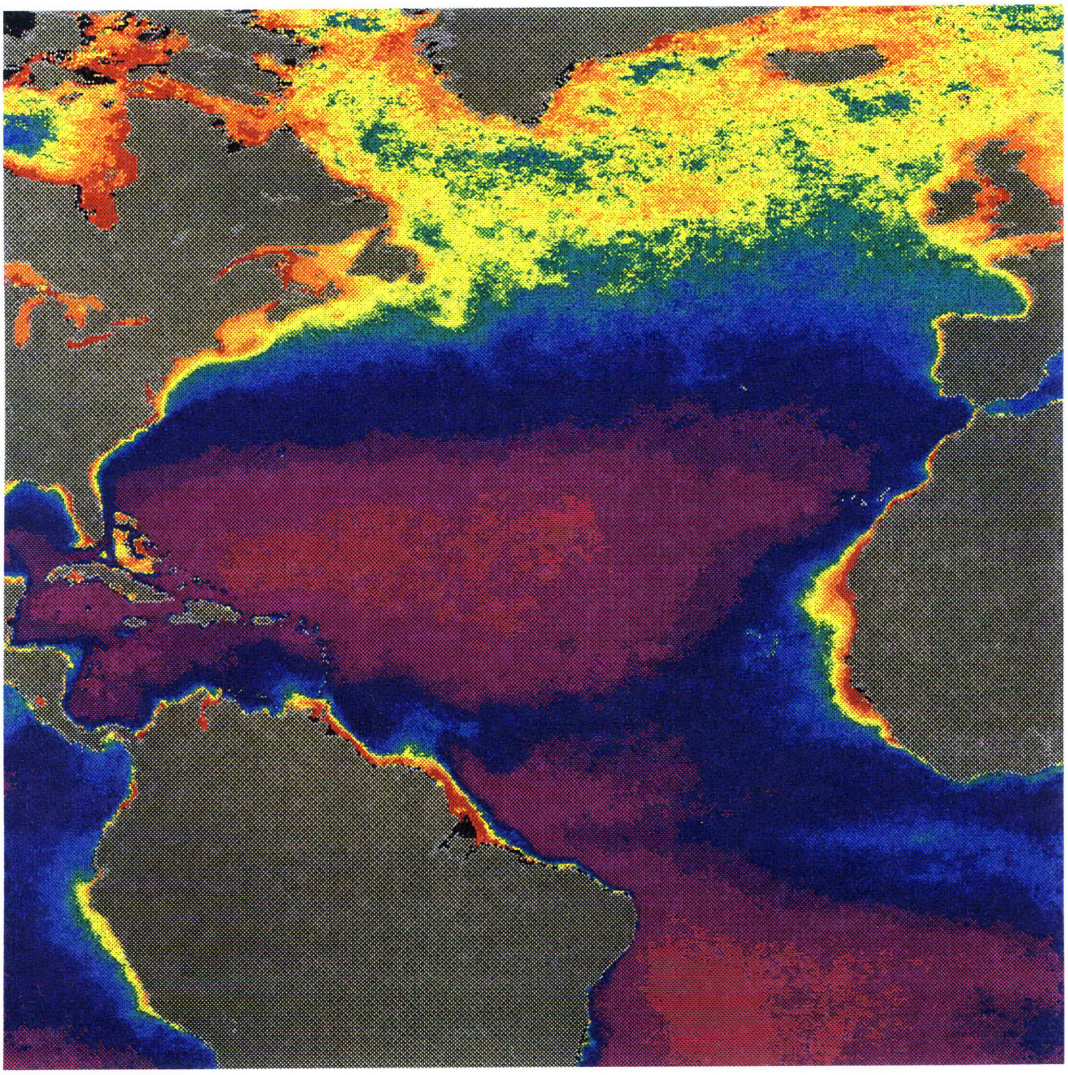

Figure 1-1: Map of ocean color for the North Atlantic. Image shown reflects a composite of all Nimbus-7 Coastal Zone Color Scanner data acquired between November 1978 and June 1986. Source: G. C. Feldman. "Nimbus-7 Coastal Zone Color Scanner Data: NORTH ATLANTIC OCEAN." *SeaWiFS Project.* 18 May 1994. `http://seawifs.gsfc.nasa.gov/SEAWIFS/CZCS_DATA/north_atlantic.html` (15 April 1997).

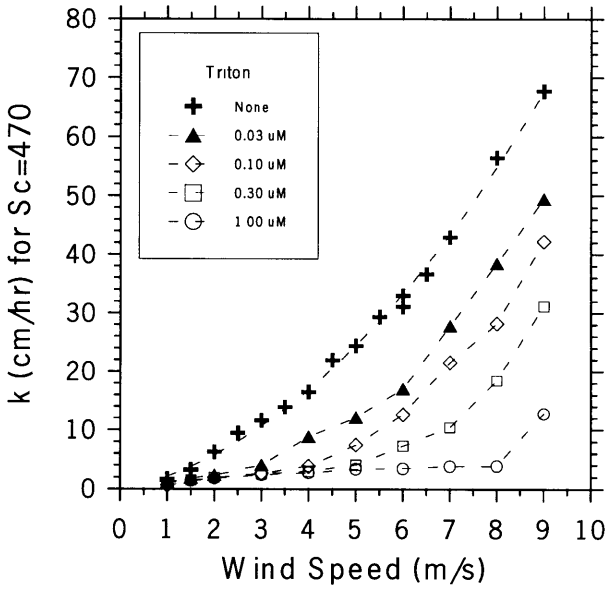

Figure 1-2: Dependence of gas-transfer velocity, k, on wind speed for clean water and dilute solutions of Triton-X-100. Source: Frew *et al.* [22].

sensing techniques for the ocean surface employ real and synthetic aperture radars that rely on backscatter of electromagnetic waves from capillary–gravity waves. Remote sensing of the wave spectra is then used, for example, to determine wind speed and direction, to locate natural and man-made ocean slicks (*e.g.*, Cini *et al.* [13]), and to observe modulation of short surface waves by internal waves.

Recent numerical and experimental studies (*e.g.*, Tsai and Yue [52]) have shown that the presence of surface-active agents can also measurably affect near-surface vorticity production. These results would seem to indicate a significant role of surface films on near-surface mixing processes. Such processes are closely related to the replenishment of the oceanic diffusive sublayer, which is a limiting rate mechanism in air–sea heat and mass transfer. In light of the work documenting surfactant effects, and with the knowledge of surfactant predominance in the open ocean, the need to properly account for surface rheology in any study probing air–sea exchange or near-surface mixing is well justified.

1.3 Basic elements of surface rheology

Before we consider the hydrodynamics of waves and vortex flow near an interface, it is beneficial to understand some fundamental properties of fluid interfaces. We restrict our attention to the case of a free surface where the upper fluid is taken to be air. We will examine the properties that are unique to film-covered surfaces and that manifest themselves in the observed phenomena discussed in § 1.2.

1.3.1 Surface tension

Of the many properties of an interface, surface tension is perhaps the most widely recognized. The concept of surface tension is actually a construct of convenience that is used in lieu of the surface free energy [1]. That there exists free energy associated with a surface is revealed by its natural tendency to contract spontaneously. This is the reason for the spherical shape assumed by bubbles and droplets, the 'beading' of droplets on a solid surface, and the phenomenon of capillarity. Surface free energy, or surface tension, can be rationalized by considering the molecular attraction forces in a liquid. In the fluid bulk, individual molecules are surrounded by neighboring molecules on all sides, and therefore experience attractive forces omnidirectionally, which on average are uniform in all directions. However, at a surface, molecules tend to be pulled inwards (toward the bulk) and laterally because the forces of attraction outwards are much less owing to the fewer number of molecules outward (*i.e.*, the molecular bonds formed between surface molecules and their surface/subsurface neighbors are enhanced). Consequently, the area of the surface will diminish and the fluid will contract until the smallest possible area for the given fluid volume is reached (hence the spherical shape in the absence of external forces). It therefore requires a finite amount of work to bring molecules from the bulk to the surface against the inward attractive forces. The required work is proportional to the increase in surface area. This work is expressed in terms of energy per unit area, or force per unit length and is called surface tension, denoted σ. A common misconception associated with surface tension is the notion that a free surface possesses a 'skin' containing a physical tension acting parallel to the interface: no such skin exists, but rather, it is simply mathematically advantageous to

treat a free surface as if it were a thin membrane under uniform tension.

An interfacial tension will exist whenever two fluids of different densities are in contact. Vanishing of the surface tension between two fluids is the condition of complete miscibility. The magnitude of σ will depend on the phases of the two fluids, and in general is a function of pressure, temperature, and composition [43].

Surface tension is very useful in describing the force balance at a curved fluid interface. Young (1805) and Laplace (1806) independently used the idea of positive surface free energy to obtain the fundamental equation of capillarity:[1]

$$p_\ell - p_a = \sigma \left(\frac{1}{R_1} + \frac{1}{R_2} \right), \tag{1.1}$$

where p_ℓ refers to the liquid-side pressure, p_a the air-side pressure, and R_1 and R_2 are the principle radii of curvature of the surface. This pressure difference is the direct consequence of the increased surface area due to the local curvature of the interface. The energy needed to effect such an increase in area is supplied by the pressure work; an interfacial pressure jump will therefore not exist for surfaces lacking curvature.

There are several different methods for experimentally determining surface tension. The technique used in this study is known as the Wilhelmy plate method [15]. In this technique, a thin plate is vertically suspended from a weighing balance and is gently brought in contact with a free surface (refer to figure 1-3). When the fluid wets the plate an additional force will be detected by the balance, this force being directly related to the surface tension by the expression

$$F = \sigma P \approx 2\sigma L, \tag{1.2}$$

where F is the force and P is the plate perimeter, which for very thin plates is well approximated by twice the plate length, L. Higher order corrections can be made for plate end effects and buoyancy effects. Equation (1.2) is only valid when the contact angle between the fluid and the plate is zero (perfect wetting). In all other cases, a multiplicative cosine factor must be incorporated to account for a finite wetting angle. To insure proper wetting, the plate should be finely roughened. A platinum plate of negligible thickness is used in the

[1] The pressure difference in (1.1) is often referred to as the Laplace pressure.

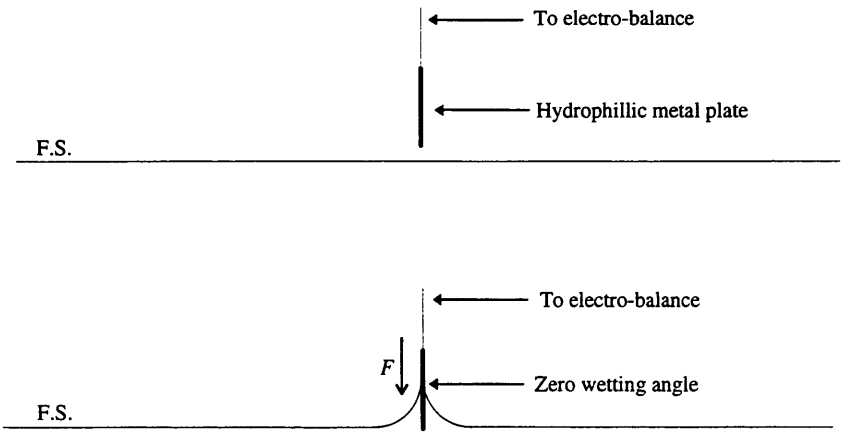

Figure 1-3: Diagram of Wilhelmy plate technique. In the upper sketch, the plate is shown suspended from an electro-balance. In the lower sketch, the plate is in contact with the fluid and a zero wetting angle has formed. The force F measured by the balance can be related to the surface tension.

present work. The plate has been sandblasted and is cleaned before each measurement by flaming in a propane/air flame.

1.3.2 Surfactants

It is well known that the surface tension of an interface is significantly reduced by the presence of a surface-active agent, or surfactant. Surfactants may possess several different names: detergent, wetting agent, emulsifier, demulsifier, or dispersing agent [19]. Surfactants are the active ingredient in most household soaps and detergents. Typically large molecules (mol wt $\simeq$ 200–2000), surfactants are bipolar in structure being comprised of a hydrophobic (water-'hating') part and a hydrophyllic (water-'loving') part. Consequently, surfactants seek an equilibrium state at an interface between aqueous and non-aqueous phases, *e.g.*, the air–water interface.

Figure 1-4 shows a surfactant molecule of oleic acid. Oleic acid molecules are composed of a hydrophobic hydrocarbon chain, or 'tail,' and a hydrophyllic polar –COOH acid group, the 'head.' The low degree of polarity in these molecules render them insoluble and they adopt a preferential orientation on the surface (taken here to be water) as shown in the lower sketch of figure 1-4. Highly insoluble surfactants form insoluble *monolayers* at the surface.

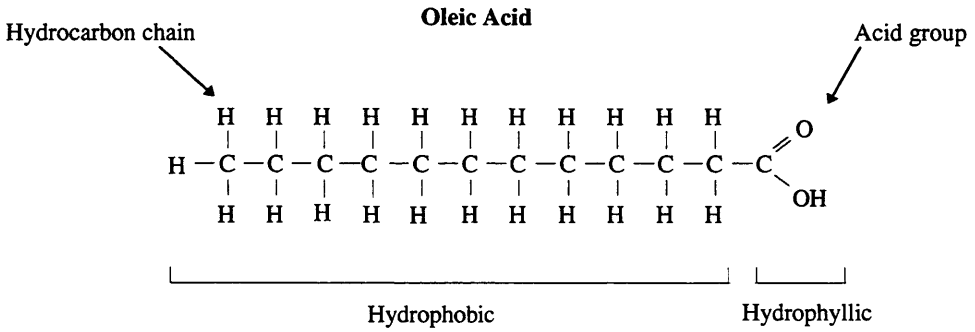

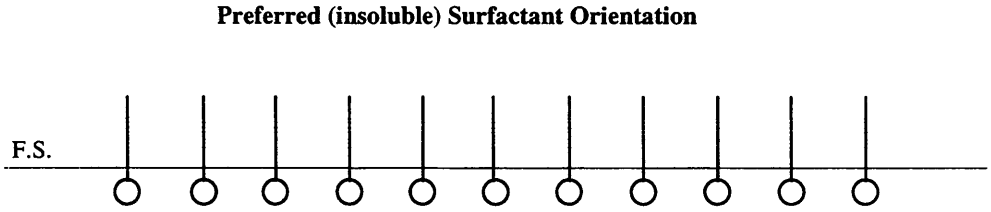

Figure 1-4: Molecule of oleic acid and preferred surfactant orientation. In the lower sketch, the O symbol represents the polar 'head,' and the ——— symbol corresponds to the hydrocarbon 'tail.'

Molecules with shorter hydrocarbon chains and/or head groups with greater polarity may be soluble in the aqueous phase.

When a surface film that exhibits surface-active properties is present on a free surface it will tend to lower the surface free energy, thus lowering the surface tension. The amount by which the surface tension is reduced is termed the surface pressure, π, and is defined as

$$\pi = \sigma_o - \sigma, \tag{1.3}$$

where σ_o is the surface tension under surfactant-free equilibrium conditions. The dependence of surface tension on surfactant concentration for insoluble surfactants may be determined experimentally using a Langmuir trough. Data from such experiments are typically reported as adsorption isotherms, or π–A isotherms, which plot surface pressure versus area per molecule. Two illustrative π–A isotherms are shown in figure 1-5. π–A isotherms provide useful information regarding surfactant molecular interactions and can be utilized to determine the Gibbs elasticity.

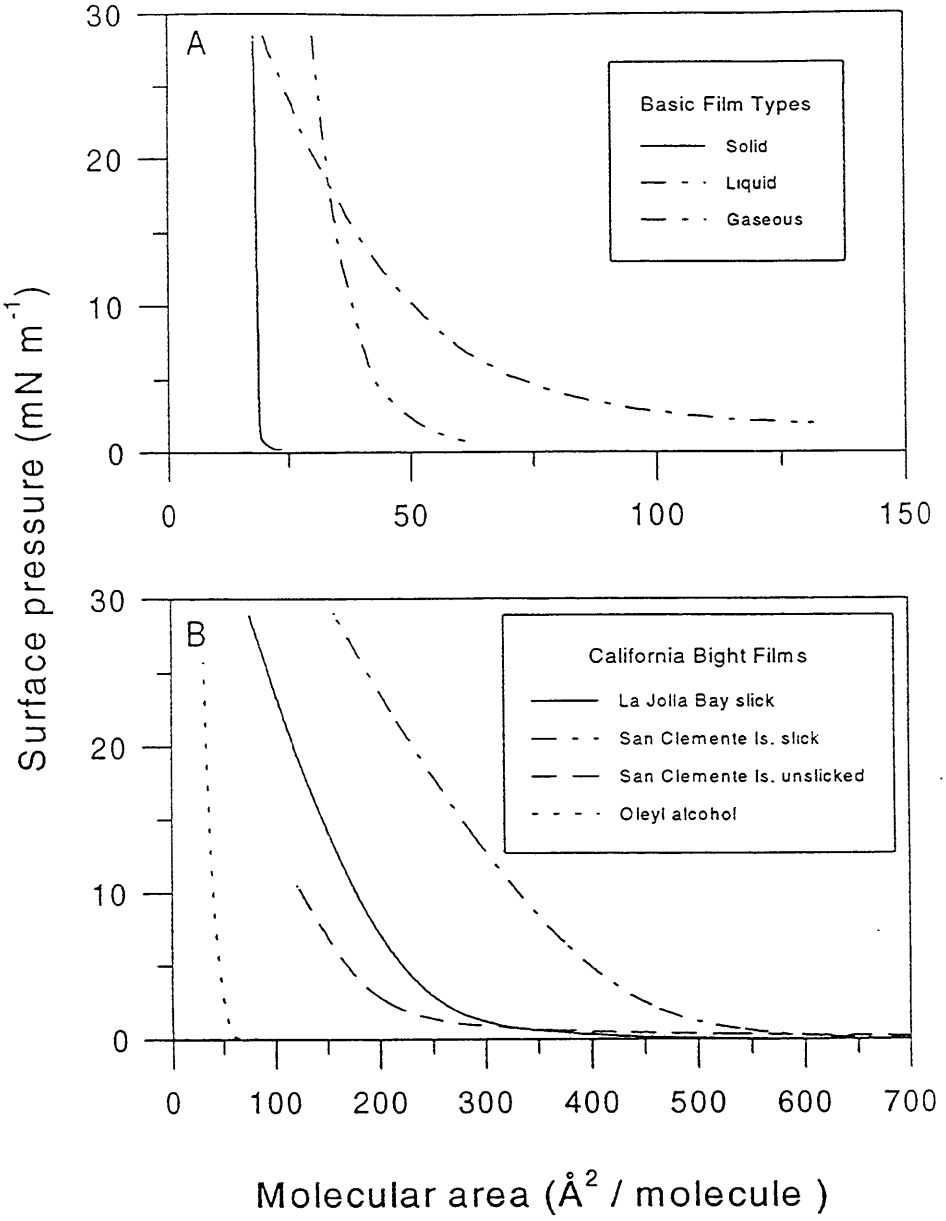

Figure 1-5: π–A isotherms for representative laboratory and ocean surface films. (A) surface pressure–area isotherms for three general monolayer films types: solid-like films represented by stearyl alcohol, liquid-like films represented by oleyl alcohol, and gas-like films represented by polyethylene glycol (300) monolaurate. (B) Isotherms for sea-surface microlayer films from the California Bight. The π–A isotherm for oleyl alcohol is shown for comparison. Source: Frew [21].

1.3.3 Marangoni forces

Based on π–A isotherm data, the surface tension of a surfactant adsorbed interface will depend on the surfactant concentration. Spatial variations in concentration necessarily result in variations in surface tension that manifest themselves as *surface tension gradients*. Gradients in σ, or equivalently, in π, can drive surface flows as well as have implications for the bulk flow below. These effects were observed by Marangoni (1871), and are generally referred to as Marangoni effects or forces. The Marangoni effect is the source of many intriguing surface flow phenomena; for example, if a highly viscous monolayer constrained on two sides by a channel is subjected to a surface tension gradient parallel to the channel walls, a two-dimensional *surface* Poiseuille flow will develop that is completely analogous to its three-dimensional counterpart (see Edwards *et al.* [19] for the derivation). Instead of being proportional to the pressure gradient, the fluid velocity is proportional to the gradient in surface tension. Marangoni forces, the result of inhomogeneities in surfactant concentration, are largely responsible for the modification of the free-surface tangential boundary condition that is of consequence for near-surface diverging flows and capillary wave dynamics. The problem becomes quite complex when the stress balance at the surface modifies the hydrodynamic flow in the bulk, which in turn redistributes the film and leads to new surface stresses. There is, in effect, a closed-loop interaction between the surface forces and the bulk hydrodynamics [52].

1.3.4 Static and dynamic surface dilational properties

Under static or quasi-static conditions, a surfactant-adsorbed surface will exhibit a surface elasticity often called the equilibrium, or Gibbs, elasticity. This elasticity acts to resist in-plane compression/dilation of the surface. The static elastic modulus, ϵ_o, is defined as

$$\epsilon_o = \frac{d\sigma}{d\ln A}, \tag{1.4}$$

which relates the dilational strain to the surface stress. This quantity is helpful in understanding the compressional behavior of a surface when the rates of compression/dilation are on the order of an hour or greater [10]. Data from adsorption isotherms are typically

used to estimate ϵ_o.

Under certain dynamical conditions, a surface may exhibit *rate-dependent* resistance to in-plane compression and dilation. The passage of a wave, for instance, will compress a surface film near the front of the wave, while dilating it on the downward moving surface behind the wave [50]. When the time scales associated with the dynamic perturbations are comparable to the time scales involved with the film adsorption/desorption and molecular re-orientation processes, the elastic modulus is modeled as having a viscous component. Additionally, if the *rate* of surface strain is non-zero, the elasticity of the film may deviate from its equilibrium value. The resulting (dynamic) viscoelastic modulus for compression/dilation can be expressed as the complex quantity

$$\epsilon_d^* = \epsilon_d + i\omega\eta_d, \tag{1.5}$$

where ω denotes radial frequency, and i is the imaginary unit. The real part of this expression corresponds to the surface dilational elasticity.[2] The quantity η_d appearing in the imaginary part of the dilational modulus is the surface dilational viscosity,[3] which accounts for the frequency-dependent response of the surface (diffusional interchange, for example). Note that ϵ_d is in general a function of frequency as well, and should not therefore be considered equivalent to Gibbs' elasticity (*cf.* Mass [37]). When the dilational modulus is real-valued the surface acts as a purely elastic film. For pure water, the viscoelastic modulus vanishes entirely and the interface is stress-free. The dilational modulus for typical samples of sea water, however, is found to be complex owing to the presence of a complex mixture of natural surfactants.

1.3.5 Dynamic surface shear properties

When a surface is subject to dynamic deformation which alters the shape of elements of free-surface area in a sense that is not purely dilational, the surface response is dictated by

[2]The surface dilational elasticity may be called the Gibbs elasticity under quasi-static conditions or the Marangoni elasticity under more dynamic conditions [19].

[3]Equation (1.5) is not strictly correct: the imaginary part of ϵ_d^* is intended to account for dissipative effects which may not be attributed to viscosity alone, but can also derive from adsorption/desorption processes and relaxation of the surface film.

the viscoelastic shear modulus, ϵ_s^*, given by

$$\epsilon_s^* = \eta_s - i\epsilon_s/\omega. \tag{1.6}$$

In this case, ϵ_s is the surface shear elasticity, and η_s is the surface shear viscosity, sometimes referred to as simply "surface viscosity." The surface shear viscosity is the most extensively studied of all rheological properties of film-covered surfaces, and is analogous to the familiar Newtonian fluid viscosity, μ.

In summary, the viscoelastic dilational modulus and the viscoelastic shear modulus comprise the formal surface stress tensor that is found in classical rheological treatments [28]. These four rheological coefficients govern the response of a surface undergoing changes in area (dilation) and/or shape (shear). A simplifying assumption often made is to neglect the shear coefficients compared to the dilational coefficients. Neglecting the shear modulus allows us to abandon the full stress tensor and characterize the surface behavior with a single viscoelastic dilational modulus. In the present study, this assumption is made, and we will hereafter consider only the surface viscoelastic dilational modulus, ϵ, defined as

$$\epsilon = \epsilon_d + i\omega\eta_d = \frac{\partial\sigma}{\partial \ln A}(\omega). \tag{1.7}$$

1.3.6 Implications of surface rheology for oceanic processes

With this new understanding of surface film properties, we will now revisit some of the physics of the air–sea interface discussed in § 1.2. As eluded to earlier, a surface film under dynamical conditions exerts a tangential stress at the interface, which in the case of pure water is nonexistent. This new stress will act to oppose surface divergences that may, for example, be the result of turbulent eddy motion. This mechanism is illustrated by figure 1-6. Consequently, surface renewal is inhibited and the resultant air–water gas transfer is moderated.

For capillary and capillary–gravity waves, a surface film will act to damp the wave motion. The heuristic reasoning behind this is that the new tangential stress modifies the hydrodynamics below resulting in more *rotational* flow in the surface boundary layer (with

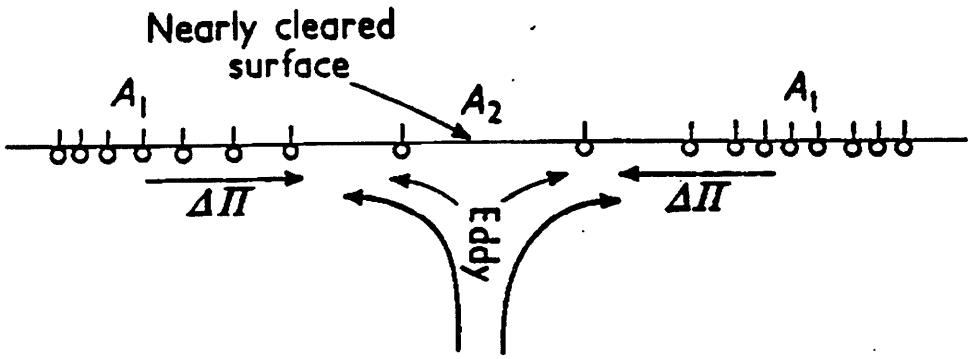

Figure 1-6: Conceptualization of surface renewal by a turbulent eddy in the presence of a surface film. The eddy upwells 'clean' fluid to the surface, while the differential spreading pressure, $\Delta\Pi$, opposes the transport of new fluid to the interface. Source: Davies and Rideal [15].

stronger velocity gradients) that is dissipated rapidly due to viscosity. Another effect, which recent studies [18] have begun to reveal, is the dynamic coupling between the transverse waves and the longitudinal (film density) waves, or Marangoni waves, that are highly dependent on the surface viscoelastic behavior. The suppression of wave slope manifests itself as a reduction in surface roughness which impacts both the air–sea momentum flux and the air–sea gas flux. Additionally, the surface signature is altered; remote sensing techniques that measure the electromagnetic backscatter from the ocean surface must therefore correct the observed wave spectra for the presence of films and slicks.

1.4 Focus of the present studies

The long-term goal of this work is to better understand and quantify the effects of surface films on near-surface mixing processes. As a model for mixing, a canonical vortex flow was chosen (an axisymmetric vortex ring impinging onto a free surface). The present contribution combines the study of capillary–gravity waves with near-surface vortical motion in an effort to link the near-surface hydrodynamics with the interfacial rheology. Such a connection is critical to modeling the physics of this problem.

The physicochemical hydrodynamics of capillary–gravity waves in the presence of surfactant is well documented and can be formulated mathematically in a straightforward

manner. Such waves are also amenable to laboratory study. By studying these short waves, the salient surface properties for small perturbations can be extracted. Concurrently, we study the free-surface interactions of a vortex flow in the presence of an insoluble surfactant. The dynamics of a vortex ring interacting with a free surface are not unlike those of wave motion; both processes involve local areas of surface compression and dilation that, in light of § 1.3, result in a viscoelastic behavior of the interface. Previous researchers have invoked simple equations of state to relate the dilational response of the surface to surfactant concentration (*e.g.*, Tsai and Yue [52]). An analytical solution to this problem, however, does not exist on the horizon. Until one does, or until the equation of state can be measured directly, it seems appropriate that experimental observations of near-surface vortex flow, characteristic of small perturbations, will provide insight as to whether small perturbation theory, so successful in describing the propagation of capillary waves, can be used to describe vortical flow at a surfactant-adsorbed free surface.

1.5 Chapter outline

In § 1, we have motivated the present work by reviewing some of the oceanographic processes that are influenced by surface films. Basic properties of surface films were introduced, and their impact of near-surface hydrodynamics was briefly explained. Chapter 2 focuses entirely on capillary–gravity waves. The early portion of this chapter is an interesting review of the rich history of the subject of wave damping by surface films. After a short survey of some of the more recent literature, the hydrodynamic problem is introduced. A complete, two-phase dispersion relation for capillary–gravity waves in the presence of a finite surface viscoelasticity is then derived. Theoretical results are subsequently presented which show some of the key relationships governing short wave propagation and dispersion. The remainder of § 2 is experimental. A system designed to measure the complex wavenumber is described and experimental results are shown. With these results, estimates of the surface viscoelasticity are made.

Chapter 3 is devoted to vortex rings. After some fundamental fluid dynamical quantities are defined, the method of vortex ring generation used in this study is explained.

Results showing the system repeatability are presented. Chapter 4 deals with the optical flow measurement technique known as digital particle image velocimetry (DPIV). A brief historical review is provided, and the system utilized presently is described in detail. The theory underlying the method of analysis for DPIV images is discussed, and the computer code written to perform this analysis is briefly explained. The chapter concludes with a discussion of the resolution and uncertainty associated with the DPIV technique.

Results from experiments with vortex rings interacting with various surfaces are presented in § 5. Free surfaces with varying viscoelasticities and a rigid boundary are investigated. Analysis of the velocity and vorticity fields begins to reveal, in a semi-quantitative sense, the different interaction behavior associated with the various interfacial conditions. Chapter 6 summarizes the results and findings of this thesis and concludes with a brief discussion.

Chapter 2

Capillary–gravity waves

2.1 Preliminary remarks

Capillary–gravity waves, sometimes referred to as "ripples," are water waves in which the restoring force for the free-surface perturbation is intermediate between that of gravity waves (where the restoring force in due to gravity) and capillary waves (where surface tension provides the restoring mechanism). Experiments with capillary–gravity waves (frequency, $f = 30$ Hz) are used in this work to parameterize the rheology of a surfactant-adsorbed surface. These measurements are then used to characterize the near-surface interaction of a vortex ring impinging at the interface.

2.2 Historical background

2.2.1 Ancient accounts

The fascination with films on water dates back to the early civilizations of man. Archaeological evidence has determined that in the fertile region between the Tigris and Euphrates Rivers known to the ancient Greeks as Mesopotamia, surface rheology was, in effect, an element of culture [49]. During the period of Hammurabi, famous for his Code (1758 B.C.), there was a great prevalence of divination, or in familiar language, fortune-telling, in the Mesopotamian region. One of the more obscure forms of divination practiced by these ancients involved pouring oil on water (or vice versa) and observing the ensuing spread-

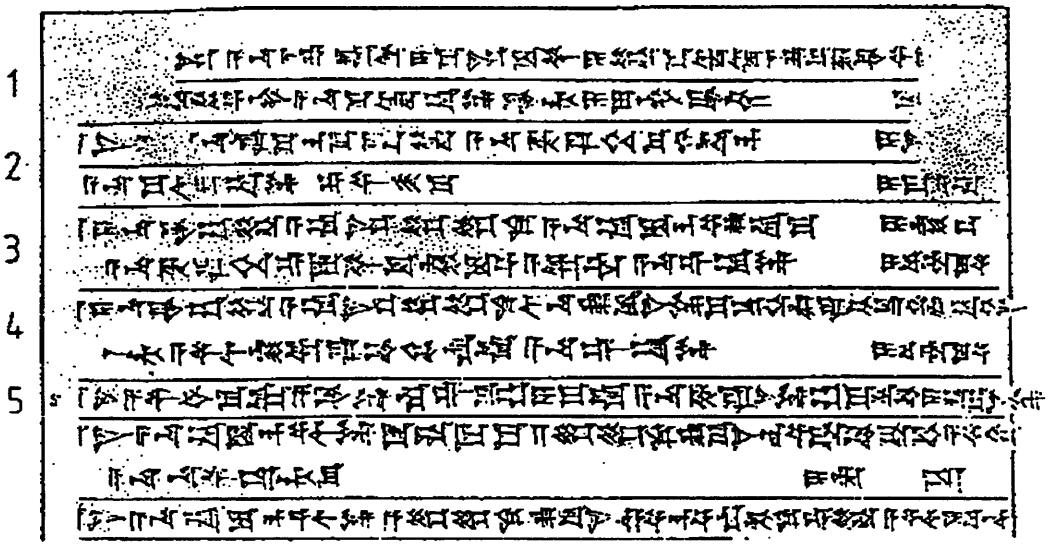

Figure 2-1: Portion of a clay cuneiform text dealing with the art of lecanomancy. The tablet dates back to the eighteenth century B.C. The omens numbered 1 through 5 discuss the spreading of oil on water. Briefly their messages follow: (1) If the oil sinks, then rises, and spreads round the water: for the campaign—unfavorable consequences; for the sick—divine punishment. (2) If the oil splits in two: for the campaign—both camps should march together; for the sick—death. (3) If a drop emerges in the east and remains stationary: for the campaign—booty; for the sick—recovery. (4) If two drops emerge, one large, one small: a male child will be born; for the sick—recovery. (5) If the oil fills the bowl: for the sick—death; for the campaign—defeat for the leader. Source: Tabor [49].

ing behavior. The Greeks later called this practice lecanomancy, meaning "divination by examining a liquid in a bowl."

Several cuneiform tablets were unearthed during the nineteenth and twentieth centuries that describe this ancient art of lecanomancy. Six tablets exist in all, the first dating from the first Babylonian dynasty (1894–1595 B.C.) [49]. A portion of one such tablet is shown in figure 2-1. From the text in this tablet, it would appear that the Babylonians of this time were most concerned with topics of health and warfare ("the campaign"). Tabor [49] has conjectured on some of the details of this divination practice: the water was most likely rain water, and the oils used by the *baru*, the 'soothsayer,' were most likely vegetable oils, thus possessing some polar constituents.

Many centuries later, the effect of oils on the damping of water waves was recorded.

In the first century A.D., Caius Plinius Secundus[1] (Pliny the Elder) wrote about this phenomenon in his *Historia Naturalis*, a vast encyclopedia of ancient knowledge and belief upon virtually every known subject at the time. In Book II, which is an account of the world and its elements, found in § 106 is the text:[2]

...omen oleo tranquillari, et ob id urinantes ore spargere quoniam mitiget naturam asperam lucemque deportet ...	...that all sea water is made smooth by oil and so divers sprinkle oil from their mouths because it calms the rough element and carries light down with them ....

The fact that ancient divers used oil to smooth the wind-roughened ocean surface so that they might see more clearly was reported by other early men of science and philosophy. In *Moralia* ("Ethical Essays"), Plutarch also notes, and endeavors to explain, the damping effects of oil on water. In § XII of the essays, *Quaestiones Naturales* ("Causes of Natural Phenomena"), Plutarch writes,

> What is the reason for the clearness and calm produced when the sea is sprinkled with oil?
>
> Is it, as Aristotle says, that the wind, slipping over the smoothness so caused, makes no impression and raises no swell?
>
> Or does this plausibly explain the external phenomena only? They say that when divers take oil into their mouths and blow it out in the depths, they get illumination and can see through the water. Surely it is impossible to adduce slipping of the wind as the cause there? Consider then whether the oil does not by reason of its density push and force aside the sea, which is earthy and irregular: subsequently when it flows back to its former position and draws together, intermediate passages are left in it, which offer transparency and clear visibility to the organs of sight [41].

Plutarch's ideas, although certainly intriguing, were misguided, and it would be hundreds of years later before this phenomenon was properly described.

[1]Born in Como, Italy in 23 A.D., Pliny's writings provided a vivid picture of ancient Roman life. Interestingly, Pliny's ultimate demise came while trying to catch a close-up glimpse of the famous eruption of Mount Vesuvius at Pompeii in 79 A.D.

[2]On the left is the original Latin, and on the right is the translation by Rackham [47].

2.2.2 Benjamin Franklin

Perhaps the most celebrated historical account of wave damping by oils was that by Benjamin Franklin [20]. In a letter to Dr. William Brownrigg, Franklin relates his prior knowledge of, and personal experience with, wave damping by oils:

> I had, when a youth, read and smiled at Pliny's account of a practice among the seaman of his time, to still the waves in a storm by pouring oil into the sea; which he mentions, as well as the use made of oil by the divers ....
>
> At length being at Clapham [London] where there is, on the common, a large pond, which I observed to be one day very rough with the wind, I fetched out a cruet of oil, and dropt a little of it on the water. I saw it spread itself with surprising swiftness upon the surface; but the effect of smoothing the waves was not produced; for I had applied it first on the leeward side of the pond, where the waves were largest, and the wind drove my oil back upon the shore. I then went to the windward side, where they began to form; and there the oil, though not more than a teaspoonful, produced an instant calm over a space several yards square, which spread amazingly, and extended itself gradually till it reached the lee side, making all that quarter of the pond, perhaps half an acre, as smooth as a looking-glass [20].

This account is, according to Giles [25], the first recorded scientific experiment in surface chemistry. In his letter, Franklin also recounts the stories of others who had observed this phenomenon as well. It was said that the Bermudans would use oil to smooth the "ruffled" ocean surface so that they could spear fish in the water more easily. Another story told of the fisherman of Lisbon who, when encountering a violent surf upon returning home, would "...empty a bottle or two of oil into the sea which would suppress the breakers, and allow them to pass safely ...." In his explanation of the damping effect, Franklin imagines, "...the wind blowing over water thus covered with a film of oil, cannot easily catch upon it, so as to raise the first wrinkles, but slides over it, and leaves it smooth as it finds it." Franklin continues, "...[the oil] prevents friction, as oil does between those parts of a machine ...."

Intrigued by the Clapham pond events, we set out to recreate the famed experiment of Franklin. Several attempts at replicating the results recorded in the Brownrigg letter were made; difficulties very much like that mentioned by Franklin were encountered. Specifically, the results observed when the oil (in this case, olive oil) was deposited at a location where

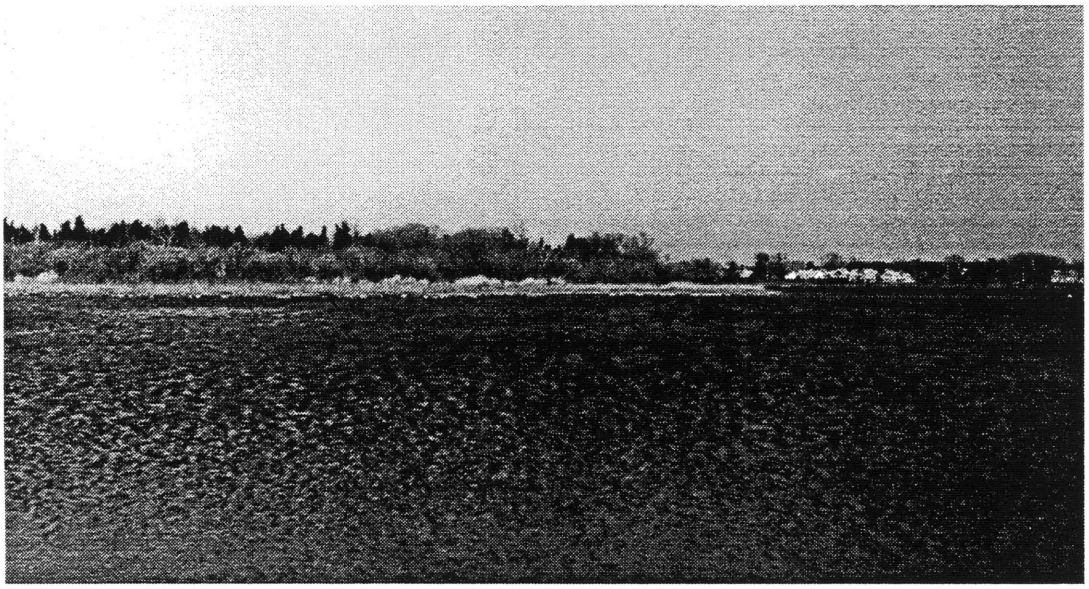

Figure 2-2: Photograph of Salt Pond showing water surface condition prior to the addition of oil.

the wind was blowing in an almost cross-shore sense were far more prominent than in other instances. Also, fetch limitations made for difficulties in distinguishing the true effects of the oil. Nonetheless, the phenomena observed when the oil is allowed to spread properly (*e.g.*, taking advantage of wave-induced Stokes drift) is fascinating. On certain occasions, Reynolds ridges (see [46]) were easily noticeable on the pond surface as the film spread. The experiments were performed on Salt Pond in Falmouth, Massachusetts. Figures 2-2 and 2-3 show photographs that were taken during a particular experiment. The amount of oil used in this case was approximately 25 ml. The area that was observed to be 'smoothed' by the film was estimated at 10000 m^2. Based on the volume of oil added, and the approximate spreading area, a crude estimate for the film thickness can be made—in this case, 25 Å. Giles carried out a similar calculation based on the text of Franklin and estimated the Clapham film to be 9.9 Å in thickness. Similar experiments by others have yielded results that are in qualitative agreement with these two values [25].

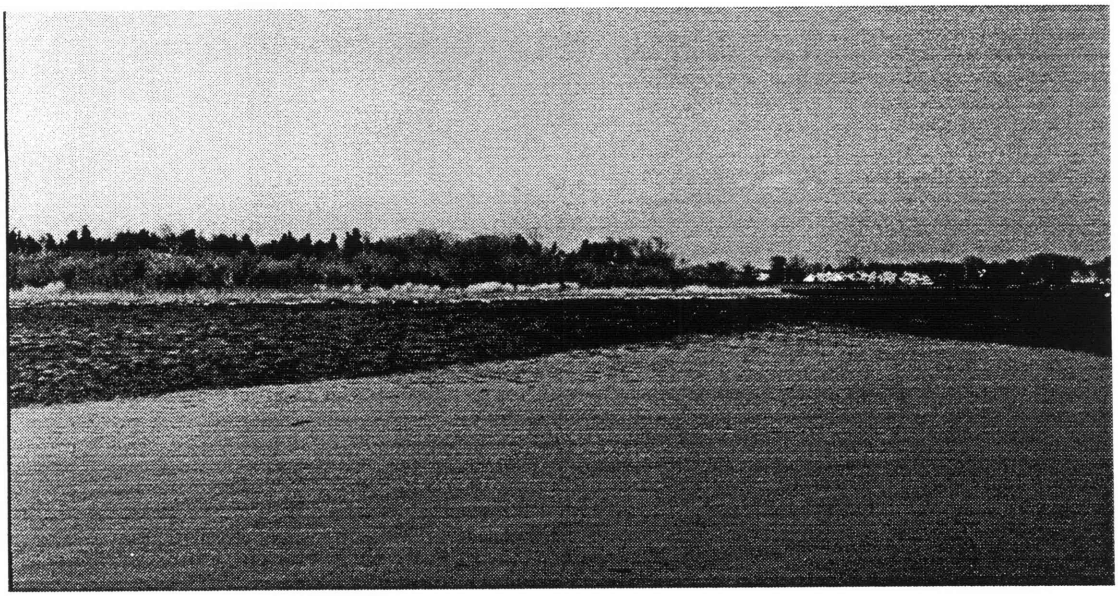

Figure 2-3: Photograph of Salt Pond showing water surface condition after the addition of oil.

2.2.3 Modern treatments of the wave damping problem

In 1883, through systematic laboratory experiments, Aitken [3] gave a qualitative explanation for the wave damping phenomena using the idea of variations in surface tension. Years later, Pockels [42] reported on her pioneering experiments using a device much like the modern Langmuir trough. The first formal mathematical treatment of the physics of damping of short water waves was provided by Lamb [32]. Lamb considered the two limiting cases of zero surface elasticity and infinite surface elasticity. In the former, damping is due only to viscosity. In the latter situation, a zero horizontal velocity at the surface is enforced that enhances the wave damping. Levich [33] carried out a similar analysis, allowing the wave frequency to assume a complex form to account for damping.

In the absence of films, the clean water result for ripples was given by Stokes in 1845 as

$$\beta = \frac{4\kappa^2 \mu \omega}{\rho g + 3\sigma\kappa^2}. \tag{2.1}$$

Here, β is the *spatial* wave damping parameter, κ is the real wavenumber ($2\pi/\lambda$, where λ is wavelength), μ is the fluid viscosity, ρ the fluid density, and ω the wave frequency.

Equation 2.1 can be used with the Kelvin dispersion relation for capillary–gravity waves,

$$\omega^2 = \frac{\sigma\kappa^3}{\rho} + g\kappa, \tag{2.2}$$

to predict the the damping coefficient for ripples on liquids with *low* viscosity.

An important result was shown by Dorrestein in 1951 [17] when he considered the mathematical problem for non-limiting values of elasticity. It was found that the damping coefficient passes through a maximum for some *intermediate* value of surface elasticity. Many other treatments have focused on this damping maximum (*e.g.*, van den Tempel and Riet [50]; Cini and Lombardini [12]). The 1969 work of Lucassen-Reynders and Lucassen [36] is one of the most comprehensive formulations of the linearized capillary–gravity wave problem. In their work, the modulus of elasticity is not assumed to be a function of only equilibrium quantities as had been assumed by earlier researchers. Working with a dynamic elasticity, Lucassen-Reynders and Lucassen derived a two-phase dispersion relation governing the propagation of capillary and capillary–gravity waves. This dispersion relation predicted the existence of two types of waves: the familiar transverse wave (Laplace wave), and a more subtle longitudinal wave (Marangoni wave). The latter wave involves the dilational oscillations of the surface film density that are resultant from the transverse wave motion. These longitudinal waves were observed experimentally under high frequency conditions [34]. In reality, these wave modes are not independent and the actual physics is some combination of the two. A recent study which has investigated the dynamic coupling of these two wave modes has been performed by Earnshaw and McLaughlin [18].

A refined dispersion relation, which ignores the air-side coupling, is given by Bock and Mann [11]. This relation corrects for the non-physical roots that had been previously predicted. Theoretical predictions based on the relation in [11] were demonstrated to correlate well with experimental observation [8]. There is an abundance of literature on the topic of capillary and capillary–gravity waves and their inclination to modification by a surface-active layer; a complete account of these works would provide for an excellent review paper. Here we have chosen to only mention a few. In the following section, a dispersion relation that incorporates the general formulation of Lucassen-Reynders and Lucassen with the

additions of Bock and Mann is derived.

2.3 A dispersion relation for capillary–gravity waves

We set out to derive a complete dispersion relation that relates various measurable quantities of capillary–gravity waves to the propagation characteristics of such waves. We include the effects of bulk viscosity and a viscoelastic free surface. The present formulation follows closely to that of Lucassen-Reynders and Lucassen.

2.3.1 Mathematical formulation

We consider the case of two-dimensional plane progressive waves in the (x, z)-plane where z is taken to be positive upward. The waves are assumed to be long-crested, *viz.*, they are independent of the y coordinate. We will account for the spatial damping of wave amplitude through a complex wavenumber, k, given as

$$k = \kappa + i\beta, \tag{2.3}$$

where κ is the real part of the wavenumber, $2\pi/\lambda$, and β is the distance damping coefficient ($\beta \geq 0$). This choice corresponds to the case of *stationary waves* [36].

In the fluid domain, mass conservation is maintained through the continuity equation

$$\nabla \cdot \mathbf{u} = \frac{\partial u}{\partial x} + \frac{\partial w}{\partial z} = 0. \tag{2.4}$$

For small wave slope (*i.e.*, $a/\lambda \ll 1$, where a is characteristic of the wave amplitude), the fluid motion can be described by the linearized Navier–Stokes equations,[3]

$$\rho \frac{\partial u}{\partial t} = -\frac{\partial p}{\partial x} + \mu \left[\frac{\partial^2 u}{\partial x^2} + \frac{\partial^2 u}{\partial z^2} \right], \tag{2.5}$$

$$\rho \frac{\partial w}{\partial t} = -\frac{\partial p}{\partial z} + \mu \left[\frac{\partial^2 w}{\partial x^2} + \frac{\partial^2 w}{\partial z^2} \right] - \rho g, \tag{2.6}$$

[3]The nonlinear term in the Navier–Stokes equations, $(\mathbf{u} \cdot \nabla)\mathbf{u}$, is second order in wave amplitude, while the remaining terms are $\mathcal{O}(a)$. For small wave amplitude, the second order terms can be neglected.

for the x and z directions respectively. In these expressions, p is the fluid pressure. A general solution for (2.4)–(2.6) is sought by postulating a velocity, $\mathbf{u}$, such that

$$\mathbf{u} = \mathbf{u_1} + \mathbf{u_2}, \tag{2.7}$$

where

$$\mathbf{u_1} = -\nabla\phi, \tag{2.8}$$

$$\mathbf{u_2} = -\nabla \times \psi. \tag{2.9}$$

The fluid velocity will therefore be described by the linear superposition of an irrotational field, characterized by the scalar potential function, ϕ, and a divergence-free field, characterized by the vorticity, or stream, function ψ. The components of velocity can now be cast in terms of these two functions as

$$u = -\frac{\partial\phi}{\partial x} - \frac{\partial\psi}{\partial z}, \tag{2.10}$$

$$w = -\frac{\partial\phi}{\partial z} + \frac{\partial\psi}{\partial x}. \tag{2.11}$$

Substituting (2.10) and (2.11) into (2.4) yields Laplace's equation,

$$\nabla^2\phi = 0. \tag{2.12}$$

The same substitution into (2.5) and (2.6) yields

$$\frac{\partial}{\partial x}\left[-\rho\frac{\partial\phi}{\partial t} + p\right] + \frac{\partial}{\partial z}\left[-\rho\frac{\partial\psi}{\partial t} + \mu\nabla^2\psi\right] = 0, \tag{2.13}$$

$$\frac{\partial}{\partial z}\left[-\rho\frac{\partial\phi}{\partial t} + p + \rho g z\right] - \frac{\partial}{\partial x}\left[-\rho\frac{\partial\psi}{\partial t} + \mu\nabla^2\psi\right] = 0, \tag{2.14}$$

where the condition (2.12) has been used. Equations (2.13) and (2.14) may be satisfied simultaneously if the following is true:

$$-\rho\frac{\partial\phi}{\partial t} + p + \rho g z = C_1, \tag{2.15}$$

and

$$-\rho\frac{\partial\psi}{\partial t}+\mu\nabla^2\psi=C_2. \tag{2.16}$$

The conditions at zero motion allow us to prescribe $C_1=p_o$ (the reference pressure at the free surface) and $C_2=0$. Equations (2.15) and (2.16) then become

$$-\rho\frac{\partial\phi}{\partial t}+(p-p_o)+\rho gz=0, \tag{2.17}$$

and

$$-\rho\frac{\partial\psi}{\partial t}+\mu\nabla^2\psi=0 \tag{2.18}$$

Equations (2.12), (2.17), and (2.18) are satisfied by the simple harmonic functions

$$\phi=Z_1(z)e^{i(kx-\omega t)} \tag{2.19}$$

and,

$$\psi=Z_2(z)e^{i(kx-\omega t)}, \tag{2.20}$$

where Z_1 and Z_2 express the vertical dependence of ϕ and ψ respectively. Here we have deviated from Lucassen-Reynders and Lucassen by arbitrarily choosing the waves to propagate in the $+x$ direction. Substitution of (2.19) and (2.20) into (2.12) and (2.18) yields two ordinary differential equations for Z_1 and Z_2:

$$\frac{d^2Z_1}{dz^2} = k^2Z_1, \tag{2.21}$$

$$\frac{d^2Z_2}{dz^2} = \left[k^2-i\omega\rho/\mu\right]Z_2. \tag{2.22}$$

It is trivial to show that

$$Z_1 = Ae^{\ell z}, \tag{2.23}$$

$$Z_2 = Be^{mz}, \tag{2.24}$$

where, in following Bock and Mann,

$$l\equiv\sqrt[+]{k^2} \tag{2.25}$$

and,

$$m \equiv \sqrt[+]{k^2 - i\omega\rho/\mu}. \tag{2.26}$$

The terms proportional to e^{-z} in (2.23) and (2.24) have been discarded to ensure a bounded solution at depth where all motion vanishes. In light of these results, (2.19) and (2.20) become

$$\phi = Ae^{\ell z}e^{i(kx-\omega t)} \tag{2.27}$$

and,

$$\psi = Be^{mz}e^{i(kx-\omega t)}. \tag{2.28}$$

The parameters l and m therefore measure the penetration depths of the potential and stream functions respectively. Using (2.27) and (2.28) in (2.10), (2.11), and (2.17) give the expressions for the velocity and pressure in the lower fluid:

$$\begin{aligned} u &= \left[-ikAe^{\ell z} - Bme^{mz}\right] e^{i(kx-wt)}, && (2.29)\\ w &= \left[-\ell Ae^{kz} + ikBme^{mz}\right] e^{i(kx-wt)}, && (2.30)\\ p - p_o &= -\rho gz - i\omega\rho Ae^{\ell z}e^{i(kx-wt)}. && (2.31) \end{aligned}$$

For the upper fluid, which extends to $+\infty$, we denote properties using prime symbols. They follow as:

$$\begin{aligned} u' &= \left[-ikA'e^{-\ell z} - B'm'e^{-m'z}\right] e^{i(kx-wt)}, && (2.32)\\ w' &= \left[-\ell A'e^{-kz} + ikB'me^{-m'z}\right] e^{i(kx-wt)}, && (2.33)\\ p' - p_o &= -\rho' gz - i\omega\rho' A'e^{-\ell z}e^{i(kx-wt)}, && (2.34) \end{aligned}$$

where

$$m' \equiv \sqrt[+]{k^2 - i\omega\rho'/\mu'}. \tag{2.35}$$

Equations (2.32)–(2.34) are obtained by using the forms of ϕ and ψ as given by (2.27) and (2.28) but with a change of sign in the z exponential term:

$$\phi' = A'e^{-\ell z}e^{i(kx-\omega t)}, \tag{2.36}$$

$$\psi' = B' e^{-m'z} e^{i(kx-\omega t)}. \tag{2.37}$$

The constants, A, A', B, and B', which are in general complex, are made unambiguous through proper boundary conditions. In deriving the final relation between w and k, these constants are eliminated.

The only task remaining is the specification of the appropriate stress boundary conditions at the interface between the upper and lower fluids. The reader is encouraged to consult [36] for a rigorous treatment of the interfacial stress balance. Here, we will simply state that a force balance[4] at the interface, which accounts for both the stress due to the bulk fluid and to the non-ideal behavior of the surface, yields the following:

$$\frac{\partial \sigma}{\partial x} + (p'_{zx} - p_{zx}) = 0, \tag{2.38}$$

$$\sigma \frac{\partial^2 \zeta}{\partial x^2} + (p'_{zz} - p_{zz}) = 0, \tag{2.39}$$

for the x direction (tangential to the interface) and the z direction (normal to the interface), respectively. Several notes of clarification are in order. In (2.38) and (2.39), ζ is the vertical displacement of the free surface measured from equilibrium, σ is the familiar surface tension from § 2,[5] and p_{ij}, p'_{ij} are given by

$$p_{zx} = \mu \left[\frac{\partial w}{\partial x} + \frac{\partial u}{\partial z} \right], \tag{2.40}$$

$$p'_{zx} = \mu' \left[\frac{\partial w'}{\partial x} + \frac{\partial u'}{\partial z} \right], \tag{2.41}$$

$$p_{zz} = -p + 2\mu \frac{\partial w}{\partial z}, \tag{2.42}$$

$$p'_{zz} = -p' + 2\mu' \frac{\partial w'}{\partial z}. \tag{2.43}$$

It is noteworthy to point out that (2.39) is the equation for the Laplace pressure given by (1.1) for the case of an inviscid fluid. In that regard, we identify (2.39) as the normal stress boundary condition, and (2.38) as the tangential stress boundary condition.

[4]The exact force balance is made more tractable by Taylor expansion and retaining only the first two terms in each series.

[5]The use of the *scalar* surface tension here is a consequence of the assumption that the shear modulus contribution is negligibly small, giving an isotropic surface stress tensor [36].

Our goal here is to derive an equation that will relate the wave frequency and wavenumber in terms of physically measurable quantities. In that vein, we begin by recalling our definition for the surface elasticity in (1.7), $\epsilon = \frac{\partial \sigma}{\partial \ln A}$, and rewrite this expression as

$$\epsilon \frac{\partial A}{\partial x}\frac{1}{A} = \frac{\partial \sigma}{\partial x}. \tag{2.44}$$

Recognizing that $\Delta A/A = \partial \xi/\partial x$, (where ξ is the horizontal deviation of the free surface from equilibrium) the surface tension gradient can be replaced by

$$\frac{\partial \sigma}{\partial x} = \epsilon \frac{\partial^2 \xi}{\partial x^2}. \tag{2.45}$$

For small amplitudes, the displacements about equilibrium, ξ and ζ, can be obtained from the linearized expressions:

$$\frac{\partial \xi}{\partial t} \approx u|_{z=\zeta} \tag{2.46}$$

and,

$$\frac{\partial \zeta}{\partial t} \approx w|_{z=\zeta}. \tag{2.47}$$

These expressions can then be integrated and, consistent with the previous linearization, evaluated at $\zeta = 0$ to yield:

$$\xi = \frac{iAk + Bm}{i\omega} e^{i(kx-\omega t)}, \tag{2.48}$$

$$\zeta = \frac{A\ell - iBk}{i\omega} e^{i(kx-\omega t)}. \tag{2.49}$$

We then substitute (2.40), (2.41), and (2.45) into (2.38) using (2.29)–(2.34) and (2.48) to obtain a new form of the normal boundary condition:

$$\overbrace{A\left[\frac{i\sigma k^2 \ell}{\omega} + \frac{i\rho g \ell}{\omega} - i\rho\omega + 2\mu\ell^2\right]}^{a_1} + \overbrace{A'\left[\frac{i\rho' g\ell}{\omega} + i\omega\rho' - 2\mu'\ell^2\right]}^{a_2} + \underbrace{B\left[\frac{\sigma k^3}{\omega} + \frac{\rho g k}{\omega} - 2i\mu k m\right]}_{a_3} + \underbrace{B'\left[-\frac{\rho' g k}{\omega} - 2i\mu' k m'\right]}_{a_4} = 0. \tag{2.50}$$

In a similar fashion, the tangential boundary condition at the interface can now be written:

$$A\overbrace{\left[-\frac{\epsilon k^3}{\omega}+2i\mu k\ell\right]}^{b_1}+A'\overbrace{\left[2i\mu' k\ell\right]}^{b_2}+$$
$$B\underbrace{\left[\frac{i\epsilon k^2 m}{\omega}+\mu(k^2+m^2)\right]}_{b_3}+B'\underbrace{\left[-\mu'(k^2+m'^2)\right]}_{b_4} = 0. \tag{2.51}$$

Note, that in arriving at (2.50) and (2.51), terms other than those involving the gravitational contributions, ρgz and $\rho' gz$, were evaluated on $z = 0$ consistent with this level of linearization. Not shown here, but also necessary are expressions for ξ and ζ in terms of the upper-phase parameters; these can be derived from relations identical to (2.46) and (2.47) with the modification that the upper-phase fluid velocities are used. This last statement implies that the lower-fluid velocity and the upper-fluid velocity are equivalent at the interface; this condition is, in fact, another boundary condition that we must impose in order to close the problem (*i.e.*, we presently have four unknowns and only two equations). Equating the two components of velocity at the surface, $u|_{z=0} = u'|_{z=0}$ and $v|_{z=0} = v'|_{z=0}$ we find:

$$-A\underbrace{[ik]}_{c_1}+A'\underbrace{[ik]}_{c_2}-B\underbrace{[m]}_{c_3}-B'\underbrace{[m']}_{c_4}=0 \tag{2.52}$$

and,

$$-A\underbrace{[\ell]}_{d_1}-A'\underbrace{[\ell]}_{d_2}+B\underbrace{[ik]}_{d_3}-B'\underbrace{[ik]}_{d_4}=0. \tag{2.53}$$

Because equations (2.50)–(2.53) are linear and homogeneous in A, A', B, and B', a nontrivial solution to the set can be found by equating the determinant formed by the respective coefficients (a_i, b_i, c_i, d_i, $i = 1 \ldots 4$), to zero:

$$\mathcal{D} \equiv \det \begin{vmatrix} a_1 & a_2 & a_3 & a_4 \\ b_1 & b_2 & b_3 & b_4 \\ c_1 & c_2 & c_3 & c_4 \\ d_1 & d_2 & d_3 & d_4 \end{vmatrix} = 0. \tag{2.54}$$

Air-side density, ρ'	0.001 g/cm^3
Air-side viscosity, μ'	0.0002 mN s/cm^2
Water-side density, ρ	1.00 g/cm^3
Water-side viscosity, μ	0.01 mN s/cm^2
Surface tension, σ	72.5 mN/m

Table 2.1: Fluid properties used in theoretical treatment. Values are those for room temperature conditions.

The result of (2.54) is an expression that relates the complex wave number, k, to the wave frequency, ω, in terms of the physical parameters of the upper and lower fluids.

Comparing equations (2.50)–(2.53) with the result obtained by Lucassen-Reynders and Lucassen, we observe that they are identical save for an opposite sign in all terms involving viscosity. This is an artifact of the convention adopted in the present formulation for waves propagating in the $+x$ direction (*cf.* (2.26) with (28) in [36]). When the determinant formed by (2.50)–(2.53) is evaluated and the upper-fluid properties are set to zero, the result reduces to the Bock and Mann relation ((10) in [11]). Also, we point out that in the absence of bulk viscosity ($\mu \to 0$), and with zero surface elasticity ($\epsilon \to 0$), the determinant formed by considering only the water-side properties degenerates to the familiar dispersion relation of Kelvin given by 2.2 (examine the term multiplying A in (2.50)).

2.3.2 Theoretical predictions for capillary–gravity wave propagation

The dispersion relation derived in the previous section can be used to predict theoretical values for the key physical quantities involved in the propagation of capillary–gravity waves. The theoretical results shown here were computed by solving the dispersion relation (2.54) numerically with a Newton–Raphson solver. For instance, figure 2-4 shows the wavenumber solution to the dispersion relation for the case of zero elastic modulus. The upper- and lower-phase fluid properties are summarized in table 2.1.

The roots of $\mathcal{D} = 0$ in figure 2-4 pertain to Laplace waves propagating both 'forward' ($+x$) and 'backward' ($-x$). For finite elasticity, figure 2-5 illustrates the presence of Laplace *and* Marangoni waves. In the case of nonzero elasticity, we observe that the Laplace waves are more damped than the case for $\epsilon = 0$. The wavelength is not changed significantly,

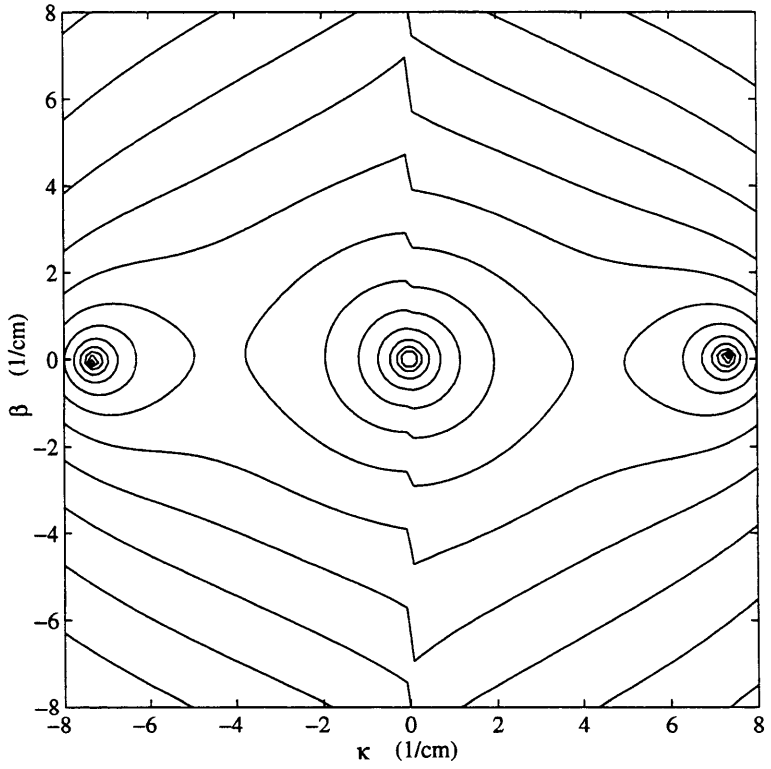

Figure 2-4: Wavenumber solution for zero elastic modulus. Wave frequency is 30 Hz. Plotted are contours of the logarithm of the magnitude of $\mathcal{D}$ showing locations of the roots. The solutions to $\mathcal{D} = 0$ correspond to $k = \pm 7.3193 \pm 0.032468i$. The root at $k = 0$ is a trivial solution. Fluid properties are given in table 2.1.

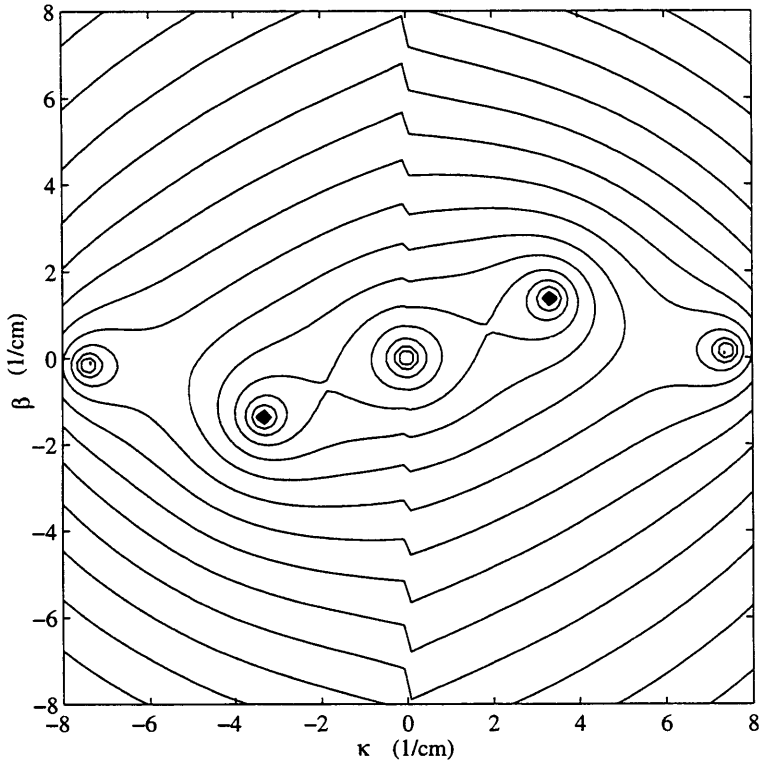

Figure 2-5: Wavenumber solution for finite elastic modulus: $\epsilon = 20$ mN/m. Wave frequency is 30 Hz. Plotted are contours of the logarithm of the magnitude of $\mathcal{D}$ showing locations of the roots. The solutions to $\mathcal{D} = 0$ correspond to $k_L = \pm 7.4193 \pm 0.153566i$ for the Laplace mode, and $k_M = \pm 3.3331 \pm 1.37024i$ for the Marangoni mode. The root at $k = 0$ is a trivial solution. Fluid properties are given in table 2.1.

Formulation	κ (1/cm)	β (1/cm)
KELVIN–STOKES	7.3131	0.031970
EQUATION (2.54) WITH AIR	$\pm$7.3193	$\pm$0.032469
EQUATION (2.54) WITHOUT AIR	$\pm$7.3141	$\pm$0.030781

Table 2.2: Root locations for $\epsilon = 0$ and $f = 30$ Hz. See text for explanation of formulations. Fluid properties are given in table 2.1.

however (κ is relatively insensitive to variations in surface viscoelasticity). The Marangoni wave solution possesses wavenumber components that are of the same order. These waves are longer, and more importantly, are damped much faster than the Laplace waves. It is these waves that are the cause of the increased wave damping for surfaces exhibiting elastic moduli.

For clean water where $\epsilon = 0$, the root locations as predicted by three different formulations are summarized in table 2.2 for the case of 30 Hz waves. The KELVIN–STOKES formulation corresponds to the the theoretical prediction of κ by (2.2) and β via (2.1) using the Kelvin wavenumber result. The EQUATION (2.54) WITH AIR formulation corresponds to the solution of $\mathcal{D} = 0$ when air-side effects are included. The EQUATION (2.54) WITHOUT AIR formulation corresponds to the solution of $\mathcal{D} = 0$ when the air-side properties are set to zero. For this case of clean water, the simple Kelvin–Stokes result is exceptionally good for both the real and imaginary parts of the wavenumber (discrepancy $< 0.1\%$ for κ, $< 2\%$ for β). The discrepancy involved with ignoring the upper phase is approximately 5% for β, at this particular frequency. While the magnitude of this discrepancy decreases with lower frequency, the relative discrepancy increases.

The real part of the wavenumber, which reflects wavelength, is related to the wave frequency via the dispersion relation, $\mathcal{D} = 0$. Figure 2-6 shows the theoretical dispersion curve for clean water at room temperature. Corresponding curves for viscoelastic surfaces are nearly identical. The damping coefficient is also highly dependent upon wave frequency. This is shown by figure 2-7 for a clean water case. The three formulations described above are plotted.

The impact of an surface elastic modulus on damping coefficient is shown by figure 2-

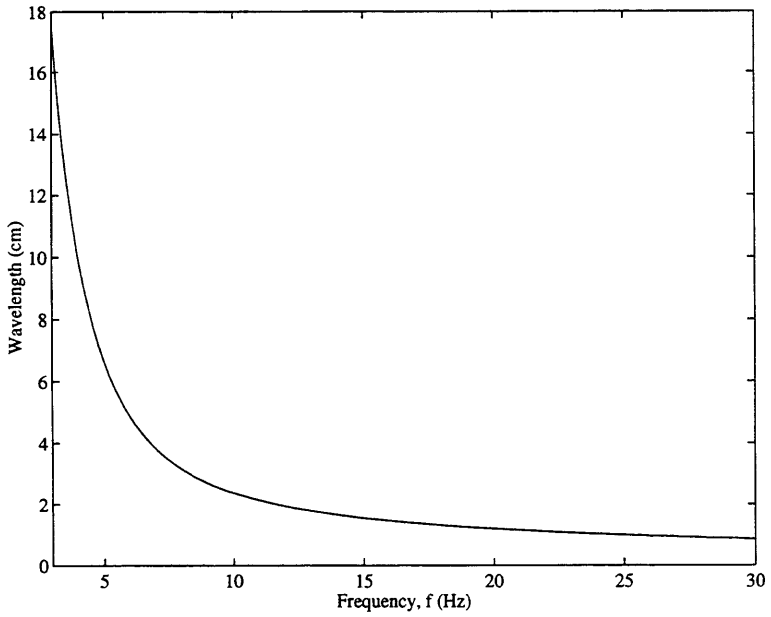

Figure 2-6: Theoretical dispersion curve for clean water ($\epsilon = 0$). Fluid properties are given in table 2.1.

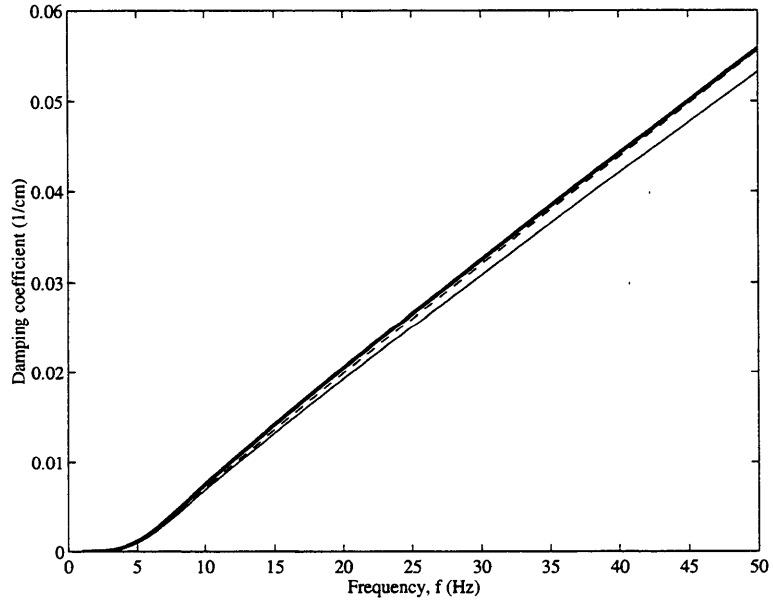

Figure 2-7: Damping coefficient as a function of frequency for clean water ($\epsilon = 0$). Three formulations shown: EQUATION (2.54) WITH AIR, (heavy); EQUATION (2.54) WITHOUT AIR, (thin); KELVIN–STOKES (broken). Fluid properties are given in table 2.1.

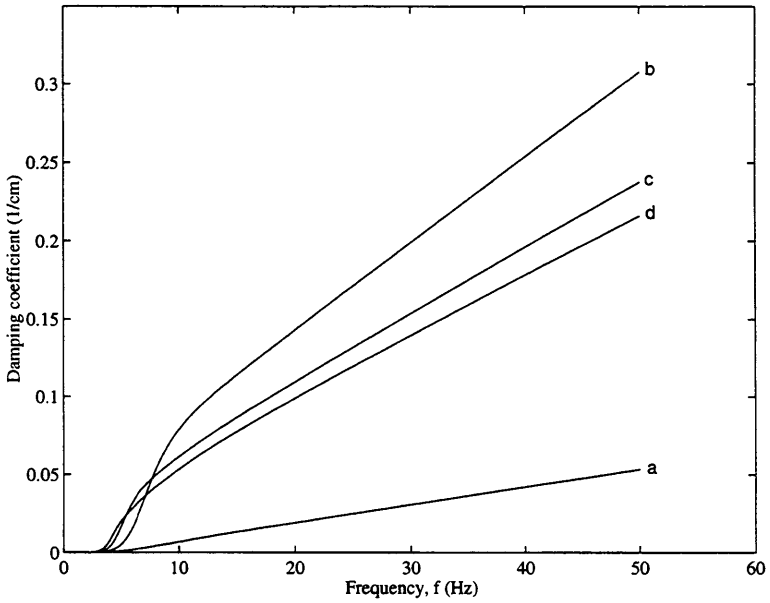

Figure 2-8: Damping coefficient as a function of frequency for varying dilational elasticity ($\eta_d = 0$). (a) $\epsilon = 0$ mN/m; (b) $\epsilon = 10$ mN/m; (c) $\epsilon = 20$ mN/m; (d) $\epsilon = 30$ mN/m. Fluid properties are given in table 2.1.

8. Here, the simple KELVIN–STOKES formulation cannot be considered valid, and the full (2.54) dispersion relation is necessary to predict wave propagation. To better illustrate the damping enhancement due to surface-active materials, plotted in figure 2-9 are normalized damping coefficients. In this figure, values of β are normalized by β_o, the damping coefficient for clean water as determined by (2.54) with $\epsilon = 0$. Finally, the dependence of damping enhancement on surface viscoelastic modulus is shown in figure 2-10. This figure illustrates the phenomena that was realized by Dorrestein in 1951: wave damping passes through a maximum at intermediate values of surface elasticity.

The waves studied in this work are radial in geometry rather than planar. It was shown by Bock [9] that cylindrical capillary–gravity waves propagate according to the same dispersion relation obtained for two-dimensional planar waves. The potential and stream functions take the form of Hankel functions of the second kind rather than the sinusoidal form in (2.19) and (2.20). The derivation given in the previous section was chosen rather than a radial formulation in order to conform with other previously published works.

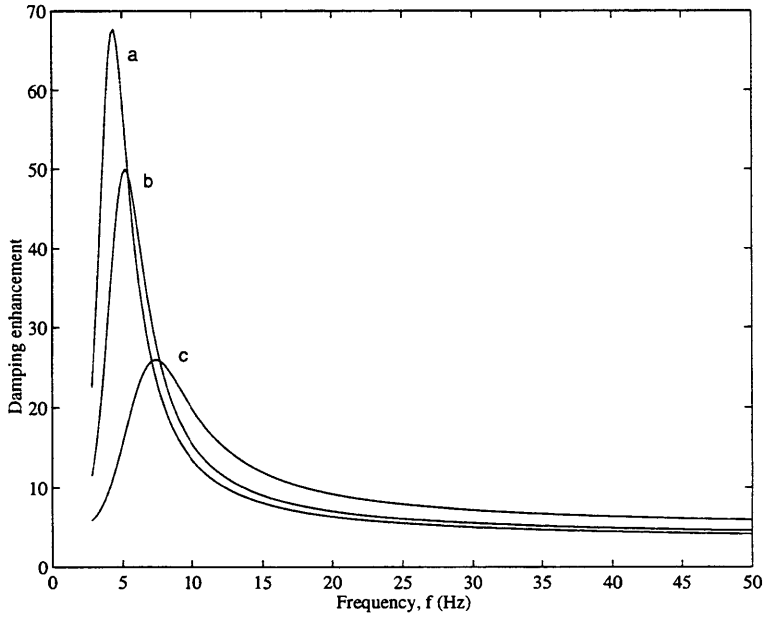

Figure 2-9: Damping enhancement (normalized damping coefficient) as a function of frequency for varying dilational elasticity ($\eta_d = 0$). (a) $\epsilon = 10$ mN/m; (b) $\epsilon = 20$ mN/m; (c) $\epsilon = 30$ mN/m. Values of β have been normalized by β_o, the damping coefficient for clean water. Fluid properties are given in table 2.1.

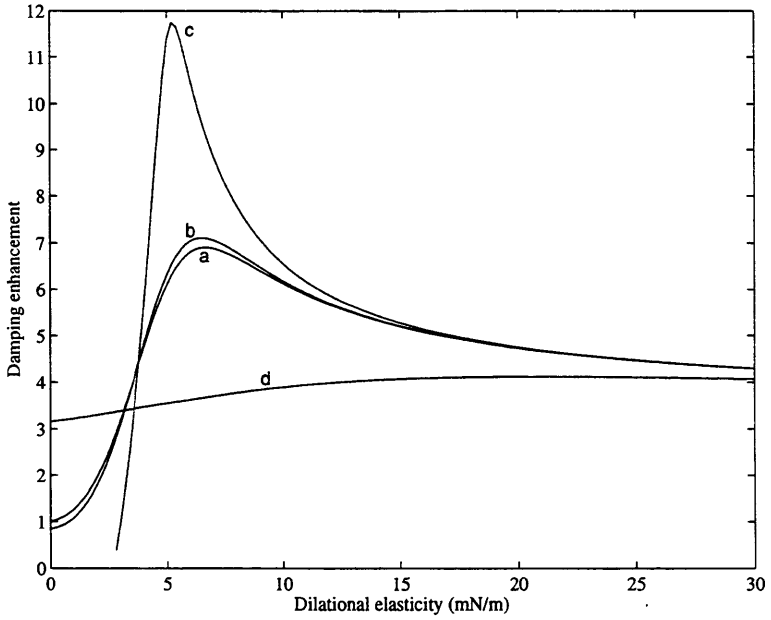

Figure 2-10: Effect of dilational elasticity on damping enhancement (β/β_o), for varying dilational viscosity, η_d. (a) $\eta_d = 0$, (b) $\eta_d = 0.001$, (c) $\eta_d = 0.01$, (d) $\eta_d = 0.1$. Wave frequency is 30 Hz; fluid properties are given in table 2.1.

2.4 Laboratory measurements of capillary–gravity waves

2.4.1 Experimental set-up

Typical wave measurements of the kind discussed here are made in long, narrow wave tanks where plane waves can be generated mechanically with relative ease. Because a key goal of this work is to concurrently study the effects of surface properties on the dynamics of both capillary–gravity waves and vortex rings, such a tank arrangement was not plausible. An experimental set-up that allows for the generation of capillary–gravity waves in the *same* tank that is used for vortex ring study was therefore developed. Wave measurements were conducted immediately subsequent to each vortex ring experiment. This marks an improvement over previous workers who have used separate tanks for characterizing free-surface properties. The glass-walled tank used in these experiments has dimensions 54.6 cm $\times$ 54.6 cm $\times$ 40.6 cm deep and has a 1.27 cm thick polycarbonate bottom. A second polycarbonate sheet is used as a tank cover to prevent airborne contamination. A stand pipe drain is located in one corner of the tank to maintain the desired water level and drain unwanted free-surface matter.

Radial capillary–gravity waves are studied experimentally in the present work to elucidate the characteristics of the free surface. Radial waves were selected for measurement because of their desirable axial symmetry. While planar waves are more commonly studied, such waves would have been difficult to produce properly in the tank described above. Because of the tank dimensions, a long, exceptionally straight wavemaker, positioned along one wall, would have been necessary to ensure perfectly plane waves. A 'point source' device that generates radially propagating waves was more easily implemented in the tank and offers greater assurance of the proper wave field.

Mechanically generated radial wave packets were produced using an audio loudspeaker as the driving mechanism. A 4 mm diameter glass rod was attached to the loudspeaker cone and suspended vertically in the tank as shown in figure 2-11. The loudspeaker was actuated using a computer generated waveform; the driving signal for the wavemaker was an enveloped 30 Hz sinusoid. Two successive Hanning windows were applied to the sinusoid to create the packet envelope. Measurements of the surface slope of each wave packet were

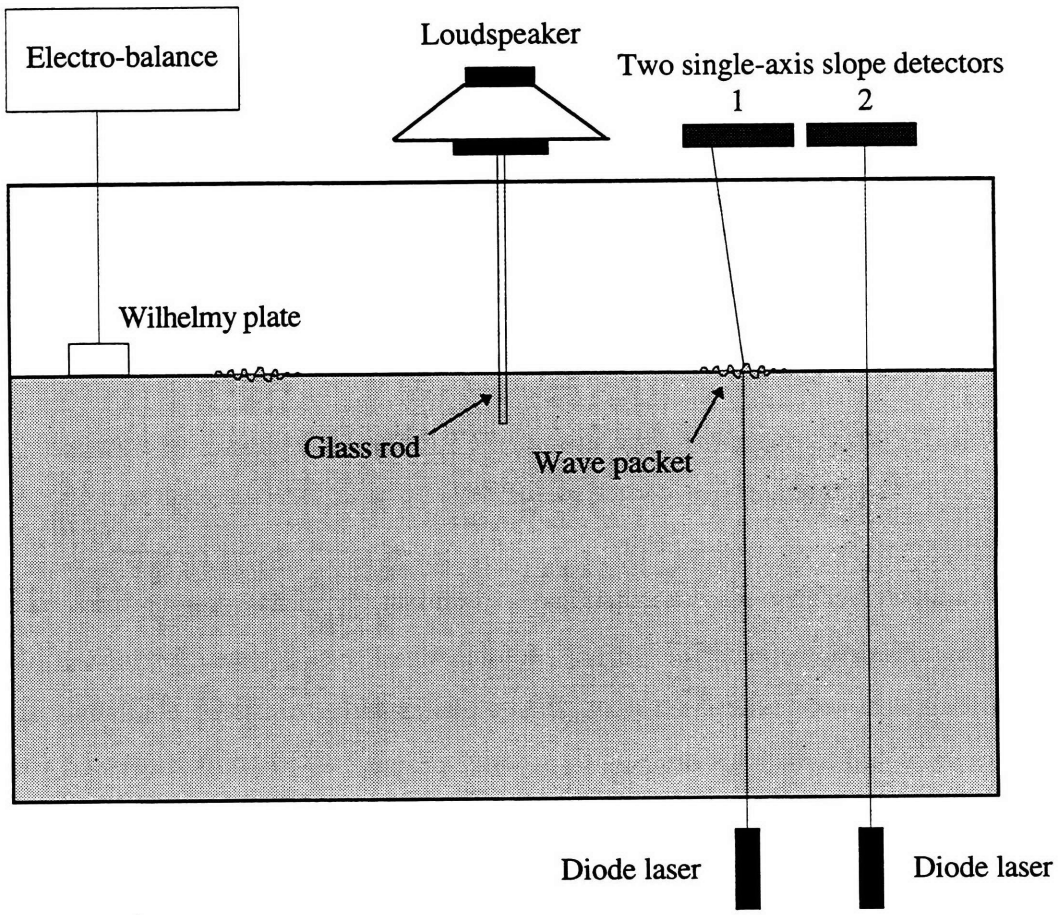

Figure 2-11: Diagram of wave measurement set-up. The distance from the wavemaker rod to detector 1 is 9.5 cm. The distance between detectors is 8.3 cm. In addition to the wave set-up, the Wilhelmy plate and electro-balance used for the surface tension measurements is also illustrated.

made using an optical technique. Two 3 mW diode lasers (670 nm) were positioned below the tank and oriented such that each beam was normal to the free surface. Two separate one-dimensional position sensitive detectors (PSDs) were used to measure the positions of the two diode laser beams during the passage of a wave packet. These detectors are opto-electronic sensors that provide signals proportional to the position of the centroid of a light spot traveling over their photosensitive surfaces. Each PSD has an active photodiode sensing area of 2.5 mm $\times$ 34 mm. The deviation of beam position from the static location yields information on wave slope so long as the distance between the free surface and the detector is constant and known. The signals from both detectors were passed through an amplification circuit and then sampled by a digitizing oscilloscope at 10 kHz. For each wave slope time series measurement, 10 runs were performed. The spacing between each run was 10 s; within this time interval, residual wave activity had completely subsided. The oscilloscope was used to sample the 10 runs of wave slope time series and compute their mean, which was then stored for analysis.

Two measurements of wave slope time series are convenient to determine the complex wavenumber, $k = \kappa + i\beta$. Specifically, it is the spatial damping parameter, β, that benefits most from measurements at two separate locations. The real part of the wavenumber, κ, can be determined from measurements of the change in phase of the wave packet over distance. In order to obtain measurements of wave slope time series for several different *closely spaced* positions, an opto-mechanical arrangement depicted in figure 2-12 was employed. The extremely close spacing is necessary to avoid phase wrap-around ambiguity. The beam incident upon detector 1 (that nearest the wavemaker) is optically 'jogged' by passing it through a rectangular prism that can be oriented precisely (0.001° resolution) at any angle. The prism angle is manipulated with a stepper motor rotation stage interfaced to a PC with a companion motion control unit. The vertically incident beam from the diode laser is initially refracted when it encounters the prism. When the beam exits the prism it is refracted once again back to vertical. Although the beam is maintained vertical, it has been horizontally shifted in space by a distance that is a function of only the prism angle and index of refraction for a given prism thickness. The prism used is a borosilicate optical glass (BK7) blank with dimensions 5.0 cm $\times$ 3.0 cm $\times$ 1.27 cm thick, and is coated with a

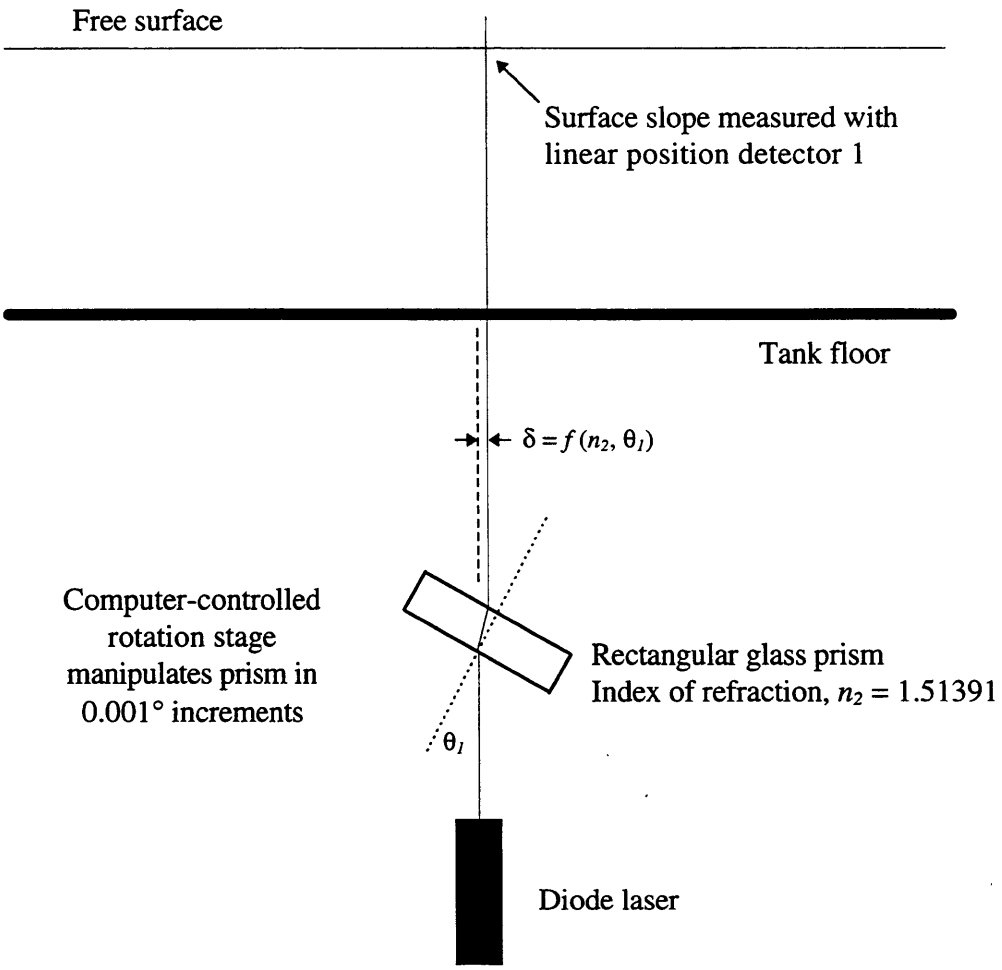

Figure 2-12: Diagram of linear positioning scheme used for phase measurements. Linear positioning resolution is 0.01 mm.

broadband antireflection coating.

The relationship between the rotation angle of the prism and the linear horizontal displacement is governed by Snell's law,

$$n_1 \sin\theta_1 = n_2 \sin\theta_2, \tag{2.55}$$

where, for this application, n_1 is the index of refraction for air (1.00), n_2 is the index of refraction of the BK7 glass, θ_1 is the angle formed by the incident beam and the prism normal, and θ_2 is the angle between the refracted beam within the prism and the prism normal. Analysis of the geometry gives an expression for the beam horizontal displacement, δ, as a function of prism angle:

$$\delta = L\frac{\sin\left[\theta_1 - \sin^{-1}\left(\frac{\sin\theta_1}{n_2}\right)\right]}{\cos\left[\sin^{-1}\left(\frac{\sin\theta_1}{n_2}\right)\right]}, \tag{2.56}$$

where L is the prism thickness. Figure 2-13 shows the relationship between the prism angle and the resulting horizontal displacement of the laser beam. The appropriate angles needed to effect relative beam displacements in increments of 0.5 mm (which lead to distinct measurement locations, each separated by 0.5 mm) were determined and used for each measurement of wave packet phase; five locations were used in all. The position of the second laser (farthest from the wavemaker) is fixed at all times and is only used for the determination of wave damping.

To summarize the experimental procedure, a single wave packet is generated by the wavemaker, and both detectors record the wave slope time series as the packet propagates radially outward. This same measurement is repeated 10 times, and the mean time series is computed and stored. The rotation stage is then actuated to translate the beam at detector 1 by 0.5 mm. The process outlined above is then repeated, and the data logged. In exactly the same manner, the remaining slope measurements at the other three 0.5 mm incremental locations are made.

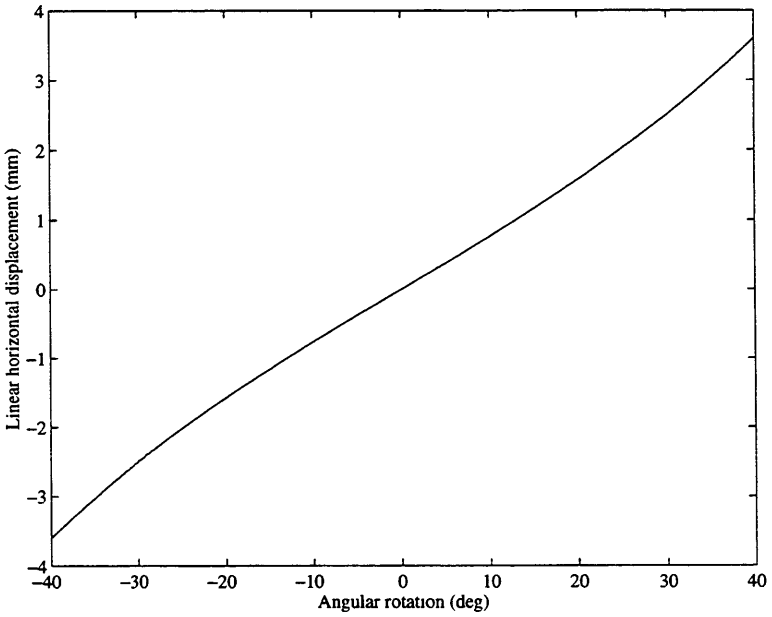

Figure 2-13: Theoretical relationship between prism angle, θ_1, and linear horizontal displacement, δ. Curve computed from (2.56).

2.4.2 Wave measurement results

Several different surfaces were investigated over the course of the present work: 'clean' free surfaces, and surfaces with varying degrees of adsorbed monolayer concentrations. Monolayers of stearic acid (octadecanoic acid, $CH_3(CH_2)_{16}COOH$, mol wt 284.47) were studied at the following surface concentrations: 1.8×10^{-10} mol/cm^2, 3.5×10^{-10} mol/cm^2, and 4.4×10^{-10}mol/cm^2. The monolayers were spread by adding solutions of stearic acid in hexane to the tank water. The concentration of each solution was chosen such that the desired surfactant concentration in the tank was achieved. Upon application, the monolayer was observed to immediately spread; the hexane quickly evaporated off.

Shown in figure 2-14 is a representative set of wave slope times series collected by detectors 1 and 2. Each trace plotted reflects the ensemble mean of 10 individual wave slope times series (all collected at the same phase measurement position in the case of detector 1). Once the wave packet encounters the tank wall, it reflects and is sensed again by both slope detectors. The wave slope associated with the reflections was not used in the

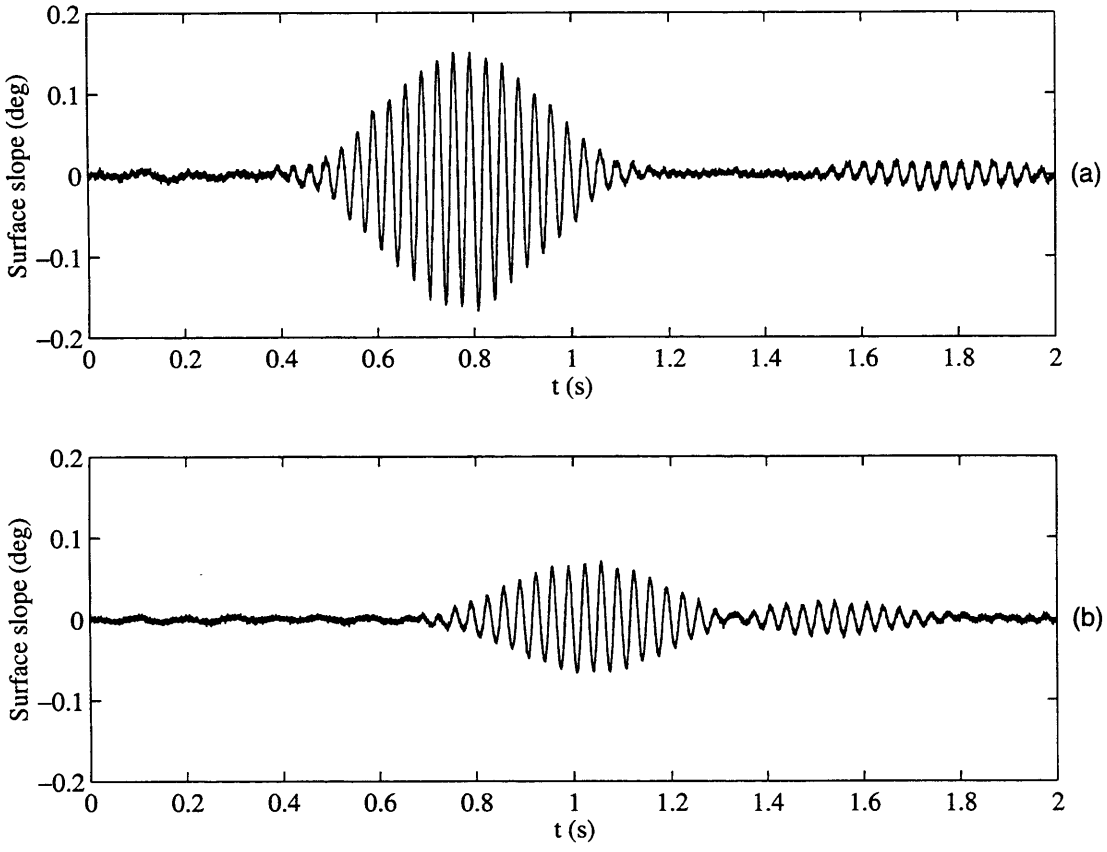

Figure 2-14: Representative surface slope time series: (a) time series from detector 1, (b) time series from detector 2. The surface is 'clean.' The reflected packet can be seen near $t = 1.8$ s in (a) and near $t = 1.6$ s in (b). The fact that the surface slope is extremely small justifies the linearized formulation in § 2.3.

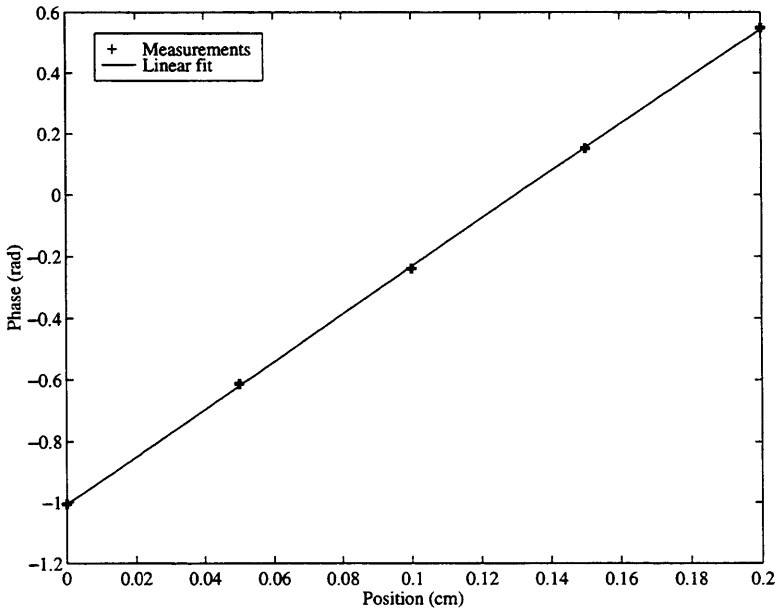

Figure 2-15: Representative phase measurement results for a monolayer surface using wave slope data from detector 1. Positions are in an arbitrary relative coordinate system. The slope of the linear fit represents the experimental calculation of the real part of the wavenumber, κ.

analysis. Wave slope can be used as a proxy for the actual wave amplitude since the two quantities are linearly proportional, only differing by a constant amount of phase.

The real part of the wavenumber can be expressed as $\kappa = \partial\phi/\partial x$, where ϕ represents the phase of the dominant wave packet frequency. In order to determine packet phase, each time series was numerically Fourier transformed, and the arctangent of the ratio of the imaginary component to the real component of the complex Fourier amplitude at the peak packet frequency (30 Hz) was computed. Measurements of packet phase at five locations (using the rotational stage arrangement) were made to determine $\Delta\phi/\Delta x$. A sample result is shown in figure 2-15.

The imaginary component of the wavenumber, β, which represents the spatial decay of wave amplitude is determined through analysis of the time series collected by both detectors. In the case of damping, only the relative magnitudes of the respective wave packets as observed by the two detectors is important. Similarly to the packet phase analysis, both

times series are Fourier transformed, and the magnitudes of the Fourier components at the peak packet frequency are used to estimate damping. This analysis can be done in frequency space since the Fourier transform is simply a linear transformation from the wave slope time series. Since by way of (2.49) with (2.3), we expect an amplitude decay of the form $e^{-\beta x}$, where x acts as the radial distance from the wave source. As such, we can express β as

$$\beta = -\frac{1}{d_{1,2}} \ln \frac{\mathcal{A}_2}{\mathcal{A}_1}. \tag{2.57}$$

In (2.57), $\mathcal{A}_1$ and $\mathcal{A}_2$ represent the *corrected* peak frequency Fourier magnitudes obtained at detectors 1 and 2 respectively. They are corrected in the order to remove the inherent amplitude decay associated with radial wave propagation; for sufficiently large x, the wave amplitude decays as approximately $\frac{1}{\sqrt{x}}$. In this analysis, the exact amplitude decay due to radial propagation was determined using the appropriate Hankel functions, and this effect was systematically removed from the damping measurements to isolate the decay due to fluid dynamical effects. The parameter $d_{1,2}$ in (2.57) is the distance between slope measurements at detectors 1 and 2.

A compilation of the wave measurement results collected during the present group of experiments is tabulated in table 2.3. The uncertainty associated with each measurement is reported; in the case of wavenumber results, the uncertainty reflects the standard deviation of the linear fit parameter. Errors associated with κ are on the order of 2%; those associated with β are approximately 9%. To further clarify table 2.3, 'clean' refers to a surface which has not been contaminated intentionally; some contaminants may be present due to the imperfect nature of the tank, the water, and the experimental apparatus. The water used in all of the experiments described in this work was commercially available spring water. This water was selected over other alternatives (*e.g.*, distilled water) because it was found to contain the least amount of biological contamination. The surfaces denoted "'clean' with particles" in table 2.3 are 'uncontaminated' surfaces of water containing seed particles that are integral to measuring the bulk fluid velocity field with the technique discussed in § 4. These surfaces are specified as unique since it was believed that the particles (acrylic spheres impregnated with fluorescent dyes; see § 4.3.1) may have imparted surface-active materials

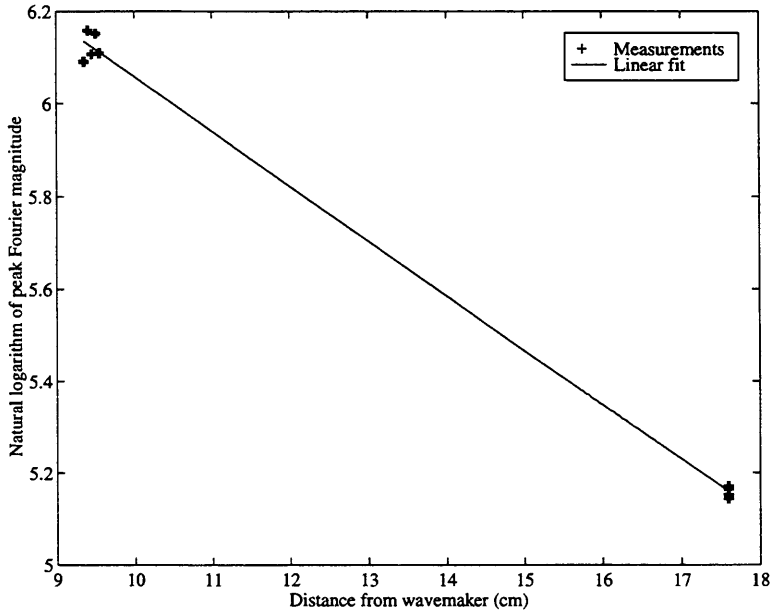

Figure 2-16: Representative damping measurement results for a monolayer surface using wave slope data collected by detectors 1 and 2. The magnitude of the slope of the linear fit represents the experimental calculation of the imaginary part of the wavenumber, β.

Surface condition/ monolayer concentration	σ (mN/m)	κ (1/cm)	β (1/cm)
'Clean'	73.37 ± 0.60	7.4932 ± 0.0709	0.0635 ± 0.0017
'Clean' with particles	72.74 ± 0.60	7.5300 ± 0.5069	0.0277 ± 0.0055
'Clean' with particles	72.82 ± 0.60	7.5826 ± 0.0754	0.0325 ± 0.0040
'Clean' with particles	72.70 ± 0.60	7.4073 ± 0.1836	0.0303 ± 0.0060
$c = 1.8\times10^{-10}$ mol/cm^2	72.49 ± 0.60	7.1777 ± 0.1936	0.0393 ± 0.0017
$c = 1.8\times10^{-10}$ mol/cm^2	72.47 ± 0.60	7.4030 ± 0.1427	0.0446 ± 0.0035
$c = 3.5\times10^{-10}$ mol/cm^2	71.79 ± 0.60	7.4867 ± 0.1433	0.1156 ± 0.0021
$c = 4.4\times10^{-10}$ mol/cm^2	70.93 ± 0.60	7.7429 ± 0.0428	0.1176 ± 0.0019

Table 2.3: Experimental wave measurement results for several different surfaces. Refer to text for explanation of surface conditions.

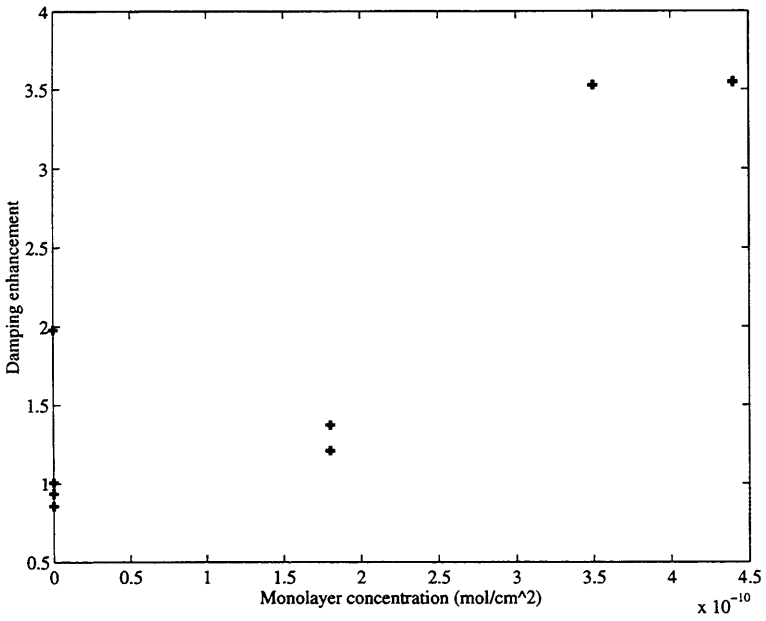

Figure 2-17: Experimental results showing the effect of monolayer surface concentration on damping enhancement, β/β_o.

to the water.

The suspect spatial damping parameter that was computed for the 'clean' case is thought to be attributable to an undetermined experimental error. The remaining results show consistent behavior with what would be theoretically expected; values are generally near those that would be predicted using (2.54) particularly when the estimated uncertainty is taken into account. Lowering of the surface tension due to increasingly higher concentrations of stearic acid monolayers is evident, as is the notable increase in wave damping; alternatively, the wavenumber changes little. We point out that at $c = 3.5\times10^{-10}$ mol/cm^2, the monolayer concentration is theoretically saturated. This is revealed by the marginal increase in wave damping at the concentration beyond this saturation limit. In order to relate these data to the work of others, the damping results of table 2.3 are plotted in figure 2-17. Damping enhancement is shown as a function of increasing monolayer concentration. We also present a published result of Lucassen and Hansen [35] in figure 2-18 for comparison. The data obtained in the present work agree well with the Lucassen and Hansen results both

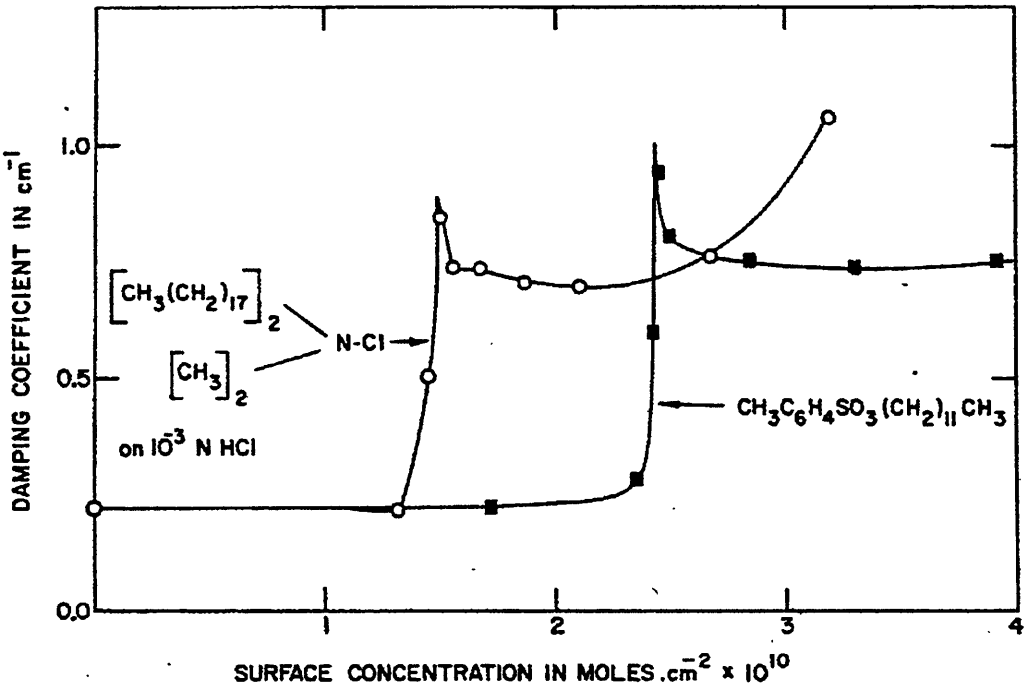

Figure 2-18: Dependence of damping coefficient on surface concentration of spread monolayers of distearyl dimethyl ammonium chloride and *N*-dodecyl-*p*-toluyl sulfonate. Source: Lucassen and Hansen [35].

Surface condition	ϵ_d (mN/m)	Uncertainty limits on ϵ_d (mN/m)	η_d (mN/m)	Uncertainty limits on η_d (mN/m)
'Clean'	1.1666	[-9.0563 2.7570]	0.0466	[0.0341 0.0571]
'Clean' with particles	0.9162	[0.2337 3.2852]	0.0380	[0.0115 0.0399]
'Clean' with particles	2.0414	[-0.5811 2.7236]	0.0344	[0.0291 0.0416]
'Clean' with particles	-4.2634	[-4.8316 2.3482]	0.0180	[-0.0033 0.0357]
$c = 1.8\times10^{-10}$ mol/cm^2	2.5962	[-4.2683 3.4284]	0.0069	[-0.0021 0.0131]
$c = 1.8\times10^{-10}$ mol/cm^2	-5.3002	[-6.3516 2.0378]	0.0096	[-0.0002 0.0422]
$c = 3.5\times10^{-10}$ mol/cm^2	4.8662	[2.1322 7.9585]	0.1009	[-0.0235 0.1771]
$c = 4.4\times10^{-10}$ mol/cm^2	3.0422	[3.3083 3.5395]	0.0290	[0.0264 0.0330]

Table 2.4: Dilational elastic modulus estimates for several different surfaces. Values for the dilational elastic modulus, $\epsilon = \epsilon_d + i\omega\eta_d$, were computed by solving (2.54) using the experimental results of table 2.3 with the physical parameters found in table 2.1.

qualitatively and in magnitude. In both cases, a trend of enhanced damping is observed as monolayer concentration is increased until, beyond some saturation limit, the damping no longer increases.

Using the results of table 2.3, and solving the dispersion relation for the elastic modulus, estimates of the dilational surface elasticities and viscosities for the surfaces investigated here were obtained (see table 2.4). Based on the uncertainties in the values of surface tension and complex wavenumber, the corresponding uncertainty limits for the individual components of the elastic modulus were computed. These limits are quite large, revealing the highly nonlinear nature of the dispersion relation (2.54). These data show, in at least a qualitative sense, the relative increase in the surface dilational elasticity with increasing monolayer presence.

2.5 Summary

In this chapter, we have demonstrated the influence of surface films on capillary–gravity wave dynamics. This topic has an exceptionally long history and currently remains a focus of interest. Upon review of the historical perspective, we present our formulation of the wave problem. We derive a complete two-phase dispersion relation that governs the propagation of capillary and capillary–gravity waves at the interface of two viscous media

having an interfacial dilational elastic modulus. This relation is then used to predict ripple propagation under various interfacial conditions. It is shown that the presence of a surface elasticity promotes enhanced wave damping, and that the maximum damping occurs at an intermediate value of elasticity. Experimental results collected for this study seem to reflect this phenomenon. More importantly, these results provide *in vitro* measurement of the damping enhancement characteristics of the various surfaces used during the vortex ring experiments.

Chapter 3

Vortex rings

3.1 The vortex ring as a topic of fluid dynamical study

Vortex rings are not uncommon in nature. Perhaps the most familiar example of a vortex ring is a smoke ring. As a self-contained, coherent fluid structure consisting of circular vortex lines, the vortex ring lends itself to both experimental and computational study. In the present work, a vortex ring flow was selected as a model for the rotational mixing and turbulent processes near the ocean surface. A vortex ring is created by an impulse of linear momentum having axial symmetry [6]. A fluid particle at the bounding edge of this radially symmetric impulse will be acted upon by the induced shear causing it to spin (see figure 3-1). Viscosity transmits this motion throughout the neighboring fluid, and a toroid of vortical flow develops.

When a vortex ring is observed in a plane passing through its axis of symmetry, it appears as two counter-rotating vortices, resembling a pair of vortex tubes. The results and analysis presented in § 5 refer to this plane (which, because of the flow symmetry, is representative of any cross-section chosen), and consequently a two-dimensional frame of reference is employed hereafter; the coordinate system is such that z is the vertical coordinate and r the radial coordinate with components of velocity w and u, respectively. The discussion of § 5 will focus on several fluid dynamical properties of vortex rings. The

most fundamental of these is the vorticity, defined as

$$\boldsymbol{\omega} = \nabla \times \mathbf{u}. \tag{3.1}$$

In our reference frame, we will only consider the out-of-plane, or azimuthal, component of the vorticity vector, which takes the simple form

$$\omega = \frac{\partial u}{\partial z} - \frac{\partial w}{\partial r}. \tag{3.2}$$

The circulation can be defined in terms of the fluid vorticity by

$$\Gamma = \int_A \boldsymbol{\omega} \cdot \mathbf{n}\, dA, \tag{3.3}$$

where the region A is the surface bounded by any closed curve C and $\mathbf{n}$ is the local surface normal. Alternatively, Stoke's theorem can be invoked to yield an equivalent expression for circulation involving the line integral of the fluid velocity tangent to the curve C,

$$\Gamma = \oint_C \mathbf{u} \cdot d\boldsymbol{\ell}. \tag{3.4}$$

In our analysis we will use (3.4) to compute circulation, and assuming two-dimensional flow in the (r, z)-plane, we will simplify (3.3) to

$$\omega = \frac{\Gamma}{A}. \tag{3.5}$$

The last quantity of interest we will consider is enstrophy. Enstrophy is defined as

$$\varepsilon = \int_A \omega^2 dA, \tag{3.6}$$

and can be thought of as a measure of the *rotational* energy associated with the flow.

3.2 Previous investigations

Vortex rings and vortex pairs have been studied extensively. Their popularity with experimentalists is no doubt a consequence of their relative ease of formation. The early work with these flow structures was limited to understanding the interaction of a vortex pair with a boundary (*e.g.*, Walker *et al.* [53]). Recent work has begun to attack much more complex problems such as vortex connection processes and quantifying surfactant effects.

The motivation for vortex studies has been varied. Barker and Crow [5] investigated the interaction of a pair of line vortices with a solid boundary and a free surface in order to gain insight into the trailing vortex pair that is shed from aircraft wings. Sarpkaya and Henderson [45] studied the surface deformations resulting from the free-surface interaction of a trailing vortex pair that was generated by towing a submerged delta wing at a negative angle of attack. Their particular interest was to better understand the surface signature of ship wakes with direct application to remote sensing (see also the more recent work of Yu and Tryggvason [58]). Years later, studies began to focus on the field of near-surface turbulence and its role in gas and heat exchange across the air–sea interface (Ohring and Lugt [40]; Hirsa and Willmarth [31]; Hirsa *et al.* [30]). These few examples begin to illustrate the diverse history of this subject; for a more thorough summary of the early literature on the subject of vortex rings and pairs, see Tryggvason *et al.* [51].

A critical turning point in the scientific study of vortex pairs interacting with a free surface was reached when Bernal *et al.* [7] discovered that the degree of surface contamination had a direct impact on the dynamics of the vortex pair at the surface. Specifically, they observed that the vortex pair *rebounded away* from even a slightly contaminated surface. Interestingly, it should be noted that this observation of rebounding was actually first reported by Barker and Crow, however they failed to provide a reasonable explanation for its occurrence. Bernal *et al.* also noted the formation of secondary and tertiary vortices as a result of surface contamination. They found that both the rebounding effect and the ancillary vortex formation was less evident when a cleaner surface was tested. They concluded that the presence of a surface film generates secondary vorticity as the vortex pair reaches the surface resulting in a reduction of the outward motion of the primary vortices causing them to rebound.

With this new realization of the effects of contamination on vortical motion at the surface, more recent studies have been conducted in an effort to begin to quantify these phenomena. The experimental work of Hirsa and Willmarth [31] which is complemented by the numerical analysis of Tryggvason *et al.* [51] is related to the present study of a vortex ring impinging on a free surface. Hirsa and Willmarth present their observations of the surface features (scars and striations) and their measurements of the subsurface flow field (using the particle image velocimetry (PIV) technique) that result from the interaction of a vortex pair with a free surface. Their study involved experiments that were performed using a clean surface as well as experiments that were conducted with a known insoluble surfactant (oleyl alcohol) present. The numerical analysis of Tryggvason *et al.*, which assumed a flat interface and used a simple model for surface contamination, is in good agreement with the laboratory work of Hirsa and Willmarth. Both groups observed that the presence of surface contamination results in the production of secondary, opposite signed, vorticity outboard of the primary vortices. This causes the primary vortices to rebound from the surface in a manner similar to that of a vortex pair colliding with a solid wall (no-slip boundary). Further numerical studies have been carried out by Wang and Leighton [54] and Tsai and Yue [52] who included effects of soluble surfactant.

Some of the most recent experimental work dealing with vortex rings has focused on understanding the mechanisms of vortex connection to a free surface. The work of Gharib and Weigand [24] considered obliquely approaching laminar rings with "clean" and "semi-clean" surfaces. In a similar investigation by Weigand and Gharib [55], turbulent vortex rings were examined. Using the digital PIV technique, both of these studies were able to outline the stages associated with the disconnection and subsequent reconnection of vortex filaments in the near-surface region.

In a very recent vortex flow study, Hirsa *et al.* [30] present time series data from second harmonic generation (SHG) measurements of hemicyanine concentration at the surface in order to estimate the dilational and shear components of the surface viscosity. However, experimental values for these viscosities were not reported. A key contribution of the present study is the addition of surface viscoelasticity measurements to the vortex ring problem. It is evident that models of the interaction between a vortex flow and a film-covered surface

require a fine understanding of the surface response characteristics. The results of § 5 begin to develop such an understanding. With better knowledge of surface properties and surface behavior, improved models of the surface equation of state may be constructed.

3.3 Vortex ring generation

A review of the literature reveals that the canonical method employed to generate vortex rings in the laboratory relies on the ejection of a small slug of fluid from a sharp-edged orifice. Variations in technique are therefore usually limited to the means by which the fluid is set in motion. In a highly mechanical set-up, Maxworthy [38] used a cam and follower arrangement that drove a horizontally mounted piston inside a variable cross-section nozzle. The effect of this apparatus was to eject a slug of fluid from the nozzle where it then rolled up into an axisymmetric ring and propagated downstream through a visualization tank. Another piston-driven vortex ring generator is described by Willert and Gharib [57]. Devices that have used an imposed pressure gradient to force fluid out an orifice are reported by Glezer and Coles [26], Bernal *et al.* [7], and McKenna *et al.* [39]. Each of these arrangements used a valving mechanism that was opened for a fraction of a second allowing a slug of fluid to be ejected from the orifice.

The vortex ring generation scheme employed in the present set of experiments is piston-driven. The complete set-up is depicted in figure 3-1 and a photograph of the arrangement is shown in figure 3-2. The piston head is rigidly connected to a linear actuator that is driven by a lead screw–DC servo motor combination. The actuator is fully controllable through a PC interface. An O-ring is seated on the piston head which enables the piston to move freely in the tube but prohibits any fluid from escaping downward. When the piston is at its starting location, the distance from the piston head to the tube orifice is 17.6 cm. The tube is stainless steel and has an inner diameter of 3.5 cm. The upper edge of the tube possesses a 7° taper resulting in a knife-edged orifice that facilitates smooth vortex ring roll-up. The stainless tube protrudes into the center of the visualization tank described in § 2.4.1. The vertical distance from the tube orifice to the tank bottom is 11.4 cm.

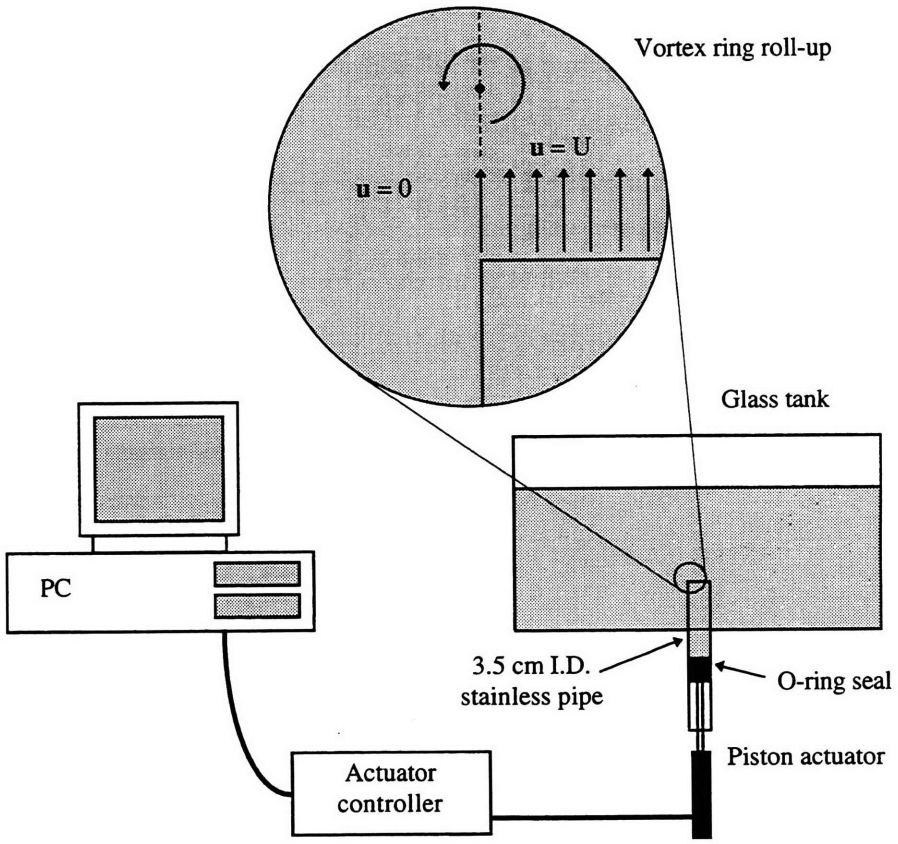

Figure 3-1: Vortex ring generation set-up. Roll-up process is shown by inset.

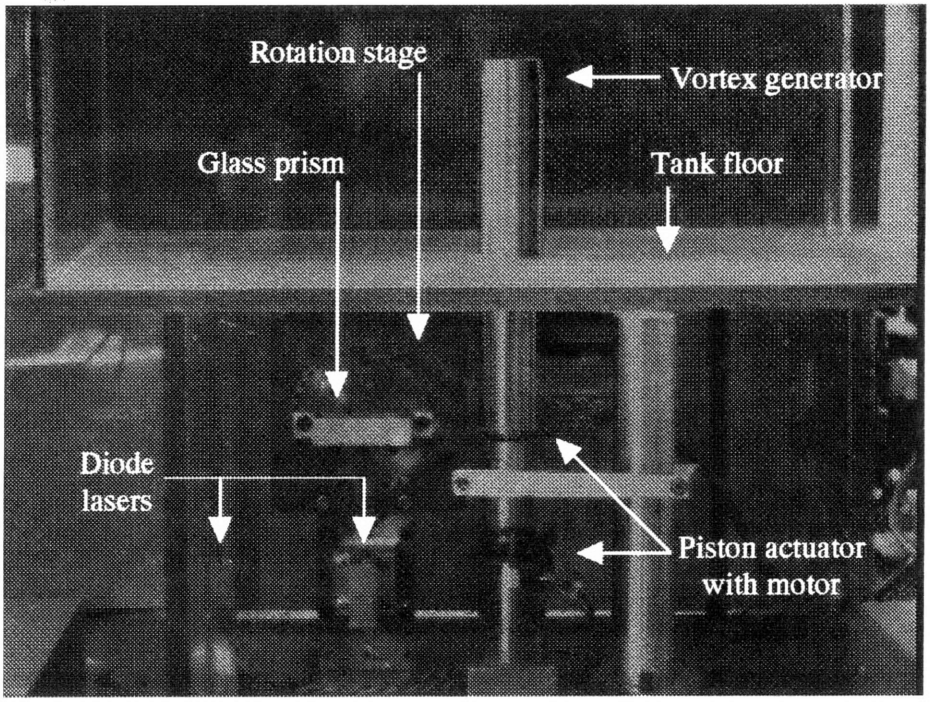

Figure 3-2: Photograph of vortex ring generator. Components associated with the wave measurements of § 2.4 are also shown.

3.4 Actuator response and repeatability

One of the goals of this work was to develop a vortex ring generation scheme that was repeatable. This section describes the response characteristics of the actuator device used in the present study and analyzes the device repeatability.

3.4.1 Actuator response to step and modified step inputs

As configured, the piston exhibits a maximum travel distance of approximately 4.3 cm. The vortex rings reported in § 5 were the result of a 3.0 cm piston excursion distance. In order to examine the response characteristics of the actuator, the step response of the actuator was determined experimentally. The actuator uses a precision linear potentiometer (0.1% linearity) for position feedback; this signal was used to monitor actuator position. A step input command of 3.1 cm was sent to the actuator controller and the resulting response was sampled using the digitizing oscilloscope. Twenty runs were collected and each run was median filtered to remove high frequency noise from the potentiometer output. The ensemble mean of the 20 runs was computed and is plotted in figure 3-3 along with the corresponding input command. The actuator system as a whole, which includes the tube/O-ring dynamics, appears to resemble a second order spring–mass–dashpot system that is slightly underdamped. The piston velocity was computed to be 24.6 cm/s.[1] The frequency of the observed overshoot was estimated to be roughly 20 Hz. A modified input command was then constructed by digitally filtering the step command with a 1 Hz low-pass filter so as to not excite resonant frequencies near 20 Hz. The resulting response (ensemble mean of 20 runs) using the filtered step command is shown in figure 3-4. Since the response was well-behaved, this input command waveform was deemed acceptable and was then examined for repeatability. Figure 3-5 shows the normalized standard deviation of these 20 actuator runs. The greatest variability is found during the latter half of the piston excursion. The normalized deviations increase monotonically during the time period $0.07 < t < 0.16$ s, reaching a maximum of approximately 1.5% the maximum excursion length. Such variability was considered acceptable for the experiments in this study.

[1] Under loading of 22–44 N, the actuator velocity is rated by the manufacturer at 25.9 cm/s.

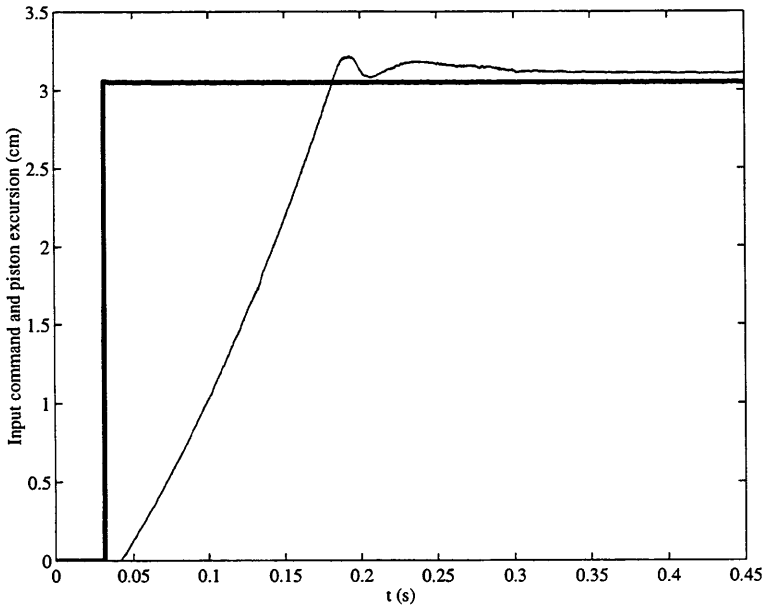

Figure 3-3: Mean piston response (thin) to a step input command (heavy).

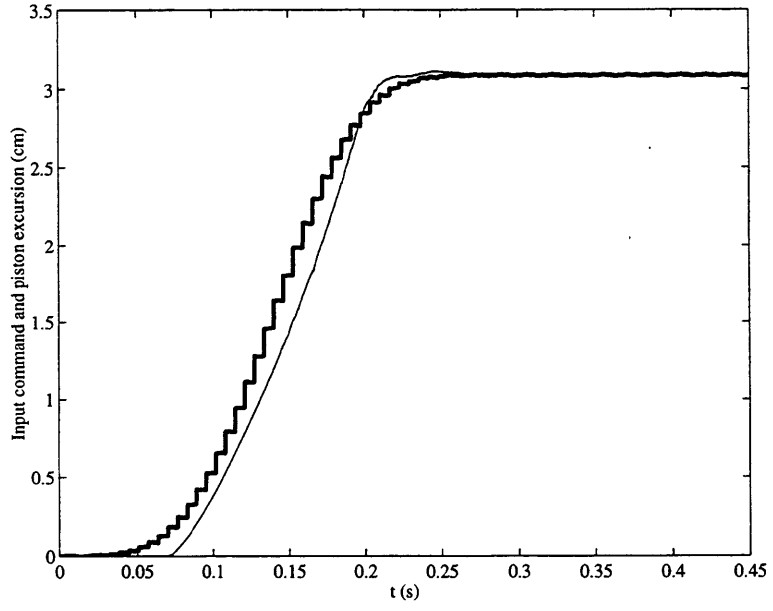

Figure 3-4: Mean piston response (thin) to modified step input command (heavy).

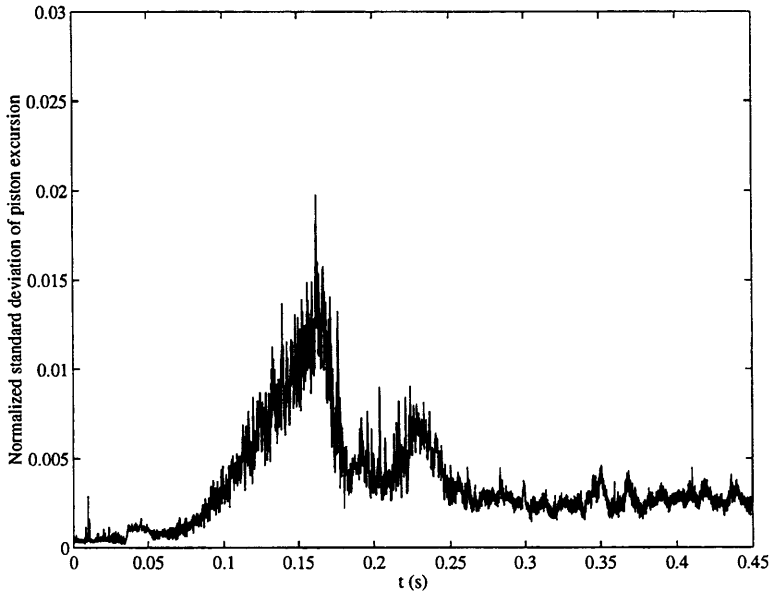

Figure 3-5: Variability of piston actuator using modified step input command. Standard deviation of piston excursion has been normalized by the full excursion length.

3.4.2 Actuator response to vortex ring generation commands

When the modified step command shown in figure 3-4 was used to generate vortex rings, the rings formed were too energetic to be suitable for the intended studies. Upon interaction with the free surface, these rings quickly broke up into turbulence. To remedy this, the input command was temporally expanded by a factor of 3 in order to reduce the piston velocity. (The stroke was also reduced from 3.1 cm to 3.0 cm.) The vortex rings produced with this new actuator displacement function were selected for repeatability study. Figure 3-6 shows the mean piston response for a series of 11 trials, and figure 3-7 shows the normalized standard deviation of this group of trials. The mean velocity of the piston, $\frac{\text{total travel}}{\text{total time}}$, was computed to be 4.7 cm/s. At its maximum, the piston velocity was 8.4 cm/s. Greater variability was observed under these conditions: the maximum deviation is approximately 3.5% the full excursion length, and occurs when the piston has reached it maximum velocity (at mid-stroke). Again, this level of deviation was considered acceptable for our application.

It was later determined that the vortex rings generated by the piston stroke shown in figure 3-6 were too weak to 'properly' interact with the free surface. These rings were also

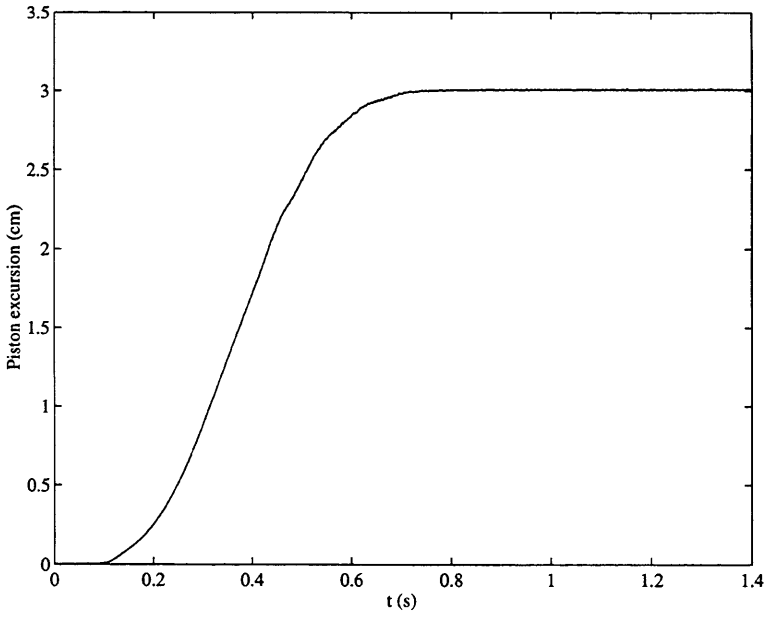

Figure 3-6: Mean response of piston actuator to vortex ring generation command.

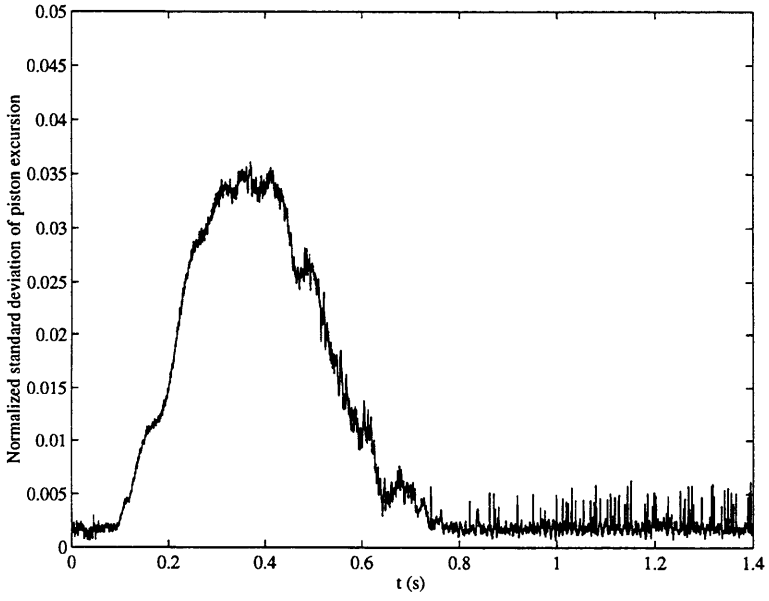

Figure 3-7: Variability of piston actuator under vortex ring generation conditions. Standard deviation of piston excursion has been normalized by the full excursion length.

observed to be heavily influenced by any ambient flow in the visualization tank. As such, these rings were generally not repeatable. A final piston command was therefore introduced which produced rings that were much less sensitive to tank initial conditions, and at the same time, were not overly energetic, thus preventing them from decaying precipitously at the free surface. The pertinent data for this piston stroke are: mean piston velocity = 8.8 cm/s, maximum piston velocity = 14.9 cm/s, normalized standard deviation of piston excursion $< 1.5\%$. The greatest variability occurred near the end of the piston stroke. Vortex rings generated using this piston command are reported in § 5.

3.5 Vortex ring generator repeatability

Measurements of the velocity field near the tube were obtained using the technique of digital particle image velocimetry (DPIV) (see § 4). These measurements provided a basis for assessing the repeatability of the vortex ring generation scheme outlined above. The two-dimensional velocity field in the vertical plane containing the axis of the tube was investigated using the DPIV technique. The piston was actuated yielding a response curve like that shown in figure 3-6. Ten trials were performed and piston response curves and corresponding velocity field evolutions (approximately 2.5 seconds of data) were collected. The maximum normalized standard deviation of the piston response for the 10 trials was 1.4% the maximum excursion.

Figure 3-8 contains a representative DPIV image with the computed velocity field overlaid. The tube orifice is clearly visible at the bottom of the image. An interesting feature to observe is the second ring that has formed near the tube opening. This smaller vortex ring is formed by the interaction of the main ring with the *outer* wall of the tube. Because of its opposite spin, relative to the main vortex ring, the smaller ring propagates downward into the tube and does not hinder the motion of the primary ring. The mean velocity field for the 10 trials at $t = 0.08$ s is shown in figure 3-9. The time, t, is defined to be the time elapsed since the onset of piston motion. The velocity field appears to show symmetry about the tube axis. The maximum velocity is roughly 4.3 cm/s; the discrepancy between this value and the mean piston velocity is most likely attributed to the attenuation of the

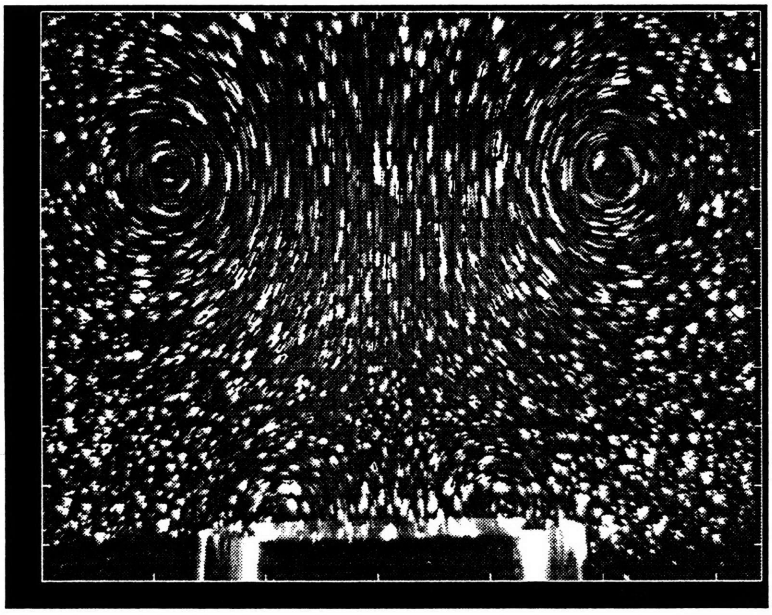

Figure 3-8: DPIV image of vortex ring roll-up. Computed velocity field is also displayed. Field shown corresponds to $t \approx 1.4$ s.

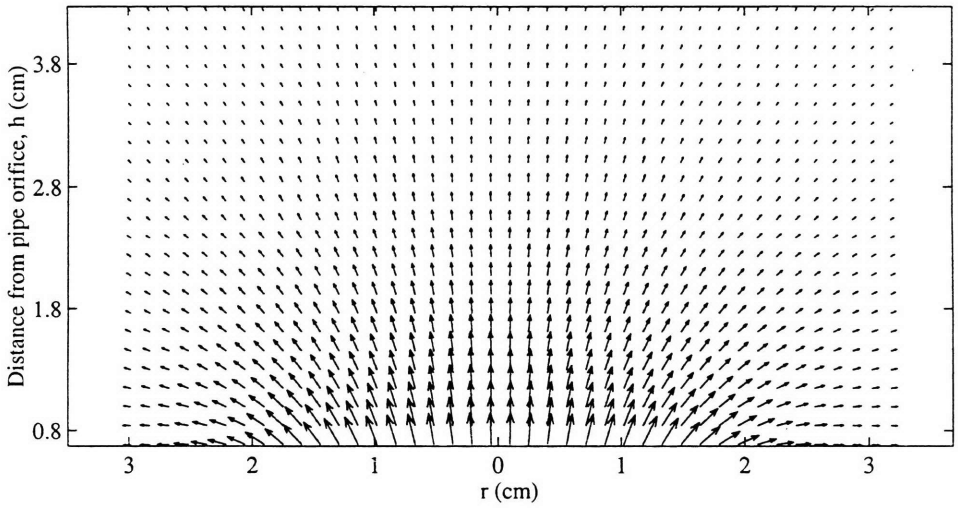

Figure 3-9: Velocity field near the tube orifice at $t = 0.08$ s. The magnitude of the largest velocity vector is 4.35 cm/s. Tube orifice extends to $r = 1.8$ cm.

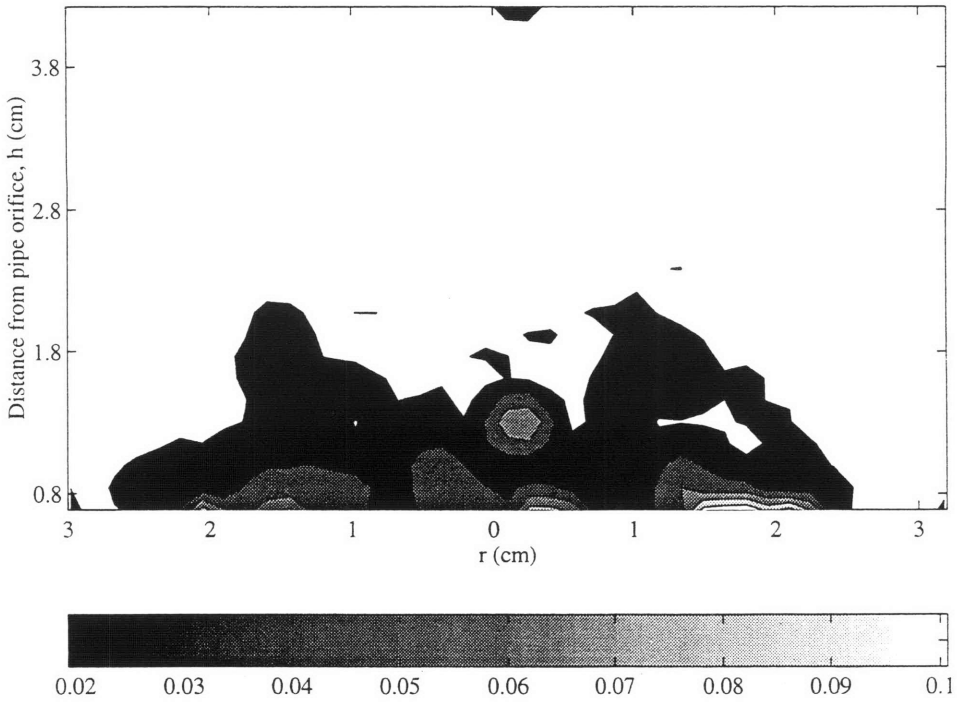

Figure 3-10: Normalized standard deviation of the velocity field near the tube orifice at $t =$ 0.08 s. Standard deviation had been normalized by the maximum flow velocity (4.35 cm/s). Contour levels are 0.02, 0.04, 0.06, 0.08, 0.1.

velocity profile by the shear stress acting at the tube inner wall. Contours of the normalized standard deviation for the velocity field of figure 3-9 are shown in figure 3-10. The standard deviation was normalized by the maximum velocity magnitude at that instant (4.35 cm/s). It appears that the typical deviation, or variability, of the burst is approximately 5% of the maximum flow velocity.

Plotted in figure 3-11 is the vertical component of velocity taken along a horizontal section at a distance $h = 0.68$ cm from the tube orifice. (This corresponds to the bottom row of velocity vectors in figure 3-9.) As expected, the profile has a crude top-hat profile. Also shown in figure 3-11 is the normalized standard deviation of this velocity profile. In this case, the deviation is normalized by the corresponding *local* vertical velocity. The variability observed along this horizontal section is on the order of 5%.

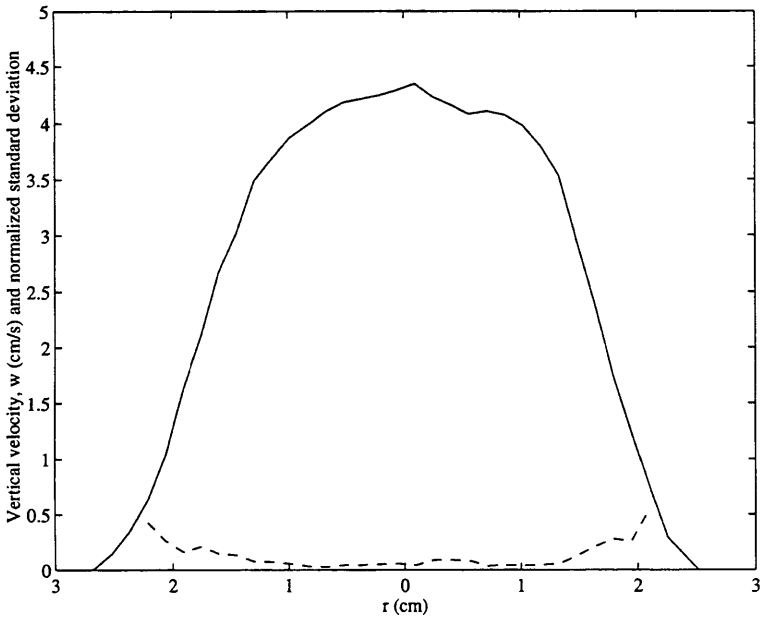

Figure 3-11: Vertical velocity profile (solid) and normalized standard deviation (dashed) for a horizontal section, $h = 0.68$ cm, above tube orifice. Standard deviation has been normalized by the corresponding local vertical velocity component.

3.6 Parameters describing the vortex ring and its surface interaction

The vortex rings studied in these experiments can be characterized by the Reynolds, Froude and Weber numbers. The initial Reynolds number can be arrived at by using the expression

$$Re_o \equiv \frac{U_p D_t}{\nu}, \tag{3.7}$$

where U_p is the mean piston velocity, D_t is the tube diameter, and ν is the dynamic viscosity of the fluid. Once the ring has evolved, a second definition of Re, based on the circulation, can be used,

$$Re \equiv \frac{\Gamma}{\nu}. \tag{3.8}$$

The Froude number is also defined in terms of the circulation,

$$Fr \equiv \frac{\Gamma}{\sqrt{gD^3}}, \tag{3.9}$$

where D is the distance between the vortex cores. For this flow, Fr provides a measure of the degree of surface disturbance due to the vortex ring impingement. A third dimensionless group, the Weber number, reflects the relative importance of the hydrodynamic forces associated with the vortex motion to the forces exerted by the free surface, and is defined as

$$We \equiv \frac{\rho\Gamma^2}{\sigma D}. \tag{3.10}$$

3.7 Summary

In this chapter, we have formally introduced the concept of a vortex ring. The equations set forth in § 3.1 will be used in the later of analysis of § 5. The vortex ring generation scheme has been described and aspects of its performance have been studied. The actuator exhibited variability well within the bounds required for the present study. Similarly, when the initial flow burst from the vortex generator was examined, repeatability was found to be quite acceptable. Finally, the relevant dimensionless parameters were introduced. Based

on the results of § 3.4, the rings examined in this study were of $Re_o \approx 3080$. Values for Re, Fr, and We are given in § 5.

Chapter 4

Digital particle image velocimetry

4.1 Preliminary remarks

Digital particle image velocimetry, or DPIV, is a relatively new flow measurement technique that has begun to receive a substantial amount of attention in recent years. Because of its ability to measure instantaneous two-dimensional velocity fields, the method is valuable to those studying fluid flow; for the engineer, DPIV offers a host of technical challenges, making it an exciting technique to develop and instrument. DPIV is a synergistic combination of different technologies, and consequently, the possible types of systems, as well as their capabilities, are wide ranging. The variety of possibilities aside, all DPIV systems are comprised of two major components: an experimental/hardware component and an analysis/software component. The DPIV technique has been used in the present work to quantify the near-surface velocity field during vortex ring interaction.

4.2 The technique of digital particle image velocimetry

4.2.1 DPIV as an alternative means of flow measurement

Experimental flow measurements are essential to the study of fluid motion. The most fundamental distinction between types of flow measurements is whether the measurement is qualitative or quantitative. Qualitative measurements are sometimes the less complicated of the two (and therefore possibly less costly), and provide a visual picture of the flow. Such

measurements typically yield valuable spatial information and can reveal structures in the flow, their sizes, orientations, variability, and relative speeds. Examples of qualitative flow measurement techniques include dye visualization, shadow graph, schlieren photography, hydrogen bubble wires, and lead precipitation methods.

When qualitative techniques are insufficient and/or physically measurable quantities are necessary, the experimentalist must resort to more quantitative methods. Quantitative measurements have historically tended to be localized point measurements. Pitot tubes and hot-wire or -film anemometers are excellent examples. Another point measurement technique, which has the advantage over the aforementioned methods of being non-invasive, is laser Doppler velocimetry (LDV). A strength of many of these point measurement methods is their very high sampling rate capability. While good temporal resolution point measurements are often perfectly adequate for many experiments, there are occasions when a quantitative velocity *field* measurement may be deemed more useful. The technique of DPIV is well suited for this task. DPIV is an optical flow measurement technique that uses pairs of digitized video frames to compute the instantaneous two-dimensional velocity field of the flow being imaged. Briefly, the method entails seeding the flow with reflective particles, illuminating these passive tracers using a strong, planar light source, and recording the resulting exposure with a high resolution CCD (charge coupled device) camera. Processing of the resulting image data involves statistical correlations between images to determine particle displacements.

The benefits of DPIV can be significant, depending on the particular application. Like other optical techniques, DPIV possesses the advantage of not disrupting the flow. The DPIV technique is particularly useful for studying unsteady flows, as opposed to single point measurements that typically only measure the mean flow and turbulent fluctuations. It has been recognized that the need to study instantaneous, unaveraged coherent turbulent structures was one of the primary motivations for the development of multi-point measurement methods like DPIV [2]. Additional utility of DPIV is revealed in instances where the purpose of an experiment is to gain information on the bulk pattern and structure of a cross-section of flow; the DPIV technique is able to provide this kind of information much

faster, or at least with less data collection time,[1] than conventional point methods. This time savings is realized because DPIV whole-field data acquisition proceeds at the real-time video rate of the camera (NTSC standard is 60 Hz field rate), and with the present ubiquity of fast computing resources, the computational processing of the individual image pairs can be done efficiently. For instance, while a conventional LDV experiment might require hours to generate an entire velocity field, DPIV has the ability to produce the same result in a matter of minutes.

4.2.2 Development of digital particle image velocimetry

Because digital particle image velocimetry is the digital counterpart of another technique known as particle image velocimetry (PIV), some discussion of this earlier method is warranted. PIV techniques are characterized by the recording of displacements undergone by small particles suspended in a fluid. The principle behind any PIV system is simple: a two-dimensional cross-section of the flow is illuminated with a strong light source, and particle positions are determined by imaging the light reflected from these tracers onto a recording medium such as a photographic film or plate. Changes in the positions of recorded particles allow for calculation of velocity vectors. While relying heavily on particle displacements, PIV is different from conventional particle tracking techniques; tracking methods involve tedious individual particle matching, whereas PIV does not require locating particle pairs by operating in a statistically based manner. As a result, a large portion of time consuming analysis is avoided.

Particle image velocimetry can be considered to be a consequence of the development of flow visualization techniques. Flow visualization has always played an important role in the study of fluid flow phenomena. But, as stated earlier, visualization techniques are qualitative, and in the past this limitation posed problems when the goal of an investigation was to evaluate a mathematical model, verify a theory, or provide true quantitative information. As a result of these difficulties, and with the advent of more sophisticated image processing techniques and computer hardware, flow visualization methods have been

[1] Often this reduction in measurement time can be of substantial economic import, especially in large flow facilities that are expensive to run.

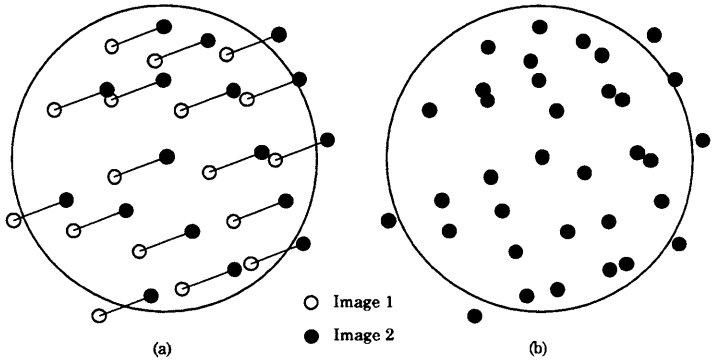

Figure 4-1: Local region of a double exposed PIV image showing particle pairs. (a) pairs are identified with a connecting line; (b) the pattern from (a) as recorded on a double exposure. Adapted from Adrian [2].

able to be extended to the acquisition of numerical data. For example, it is now possible by means of standard image processing techniques to identify structures in a turbulent flow and to follow these structures in time through processing of the digitized images. In this way, quantitative information on the development of the flow is obtained.

These newer methods, such as PIV, are not without difficulties. Because of the nature of the PIV (and DPIV) process, providing feedback on the quality of the data and results during an experiment is not as straightforward as more traditional point methods. Another drawback encountered by methods that still rely on photographic recording is the time consuming film development and processing involved.

Principles of particle image velocimetry

The basis for any PIV system was mentioned briefly above and is now covered in greater detail. PIV relies on double exposed images of the flow. Figure 4-1 shows a sketch of a PIV double exposure. Evident in this figure are some of the idiosyncrasies encountered with PIV images: some particles can appear to overlap and others may leave/enter the local processing region. To produce such images, the flow is illuminated with a pair of short light pulses (white light or, more often, laser light) with a known temporal separation. Light *pulses* are used in order to 'freeze' particles in space for the imaging medium. Unshuttered,

continuous illumination will result in unwanted particle streaking for all but the slowest flows. These light pulses are specially formed into thin, two-dimensional sheets so as to illuminate only a cross-section of the flow. The light reflected from seed particles present in the flow is recorded in an image format. Only those particles contained in the light sheet are detected. Entire images are processed using local sub-regions to measure the particle displacements between a pair of subsequent exposures. From that information, determining the velocity field is trivial. The appropriate relation for the local fluid velocity, $\mathbf{u}$, is simply

$$\mathbf{u} = \lim_{t_2 \to t_1} \frac{\mathbf{x_2} - \mathbf{x_1}}{t_2 - t_1},$$

which for closely spaced light pulses, tends to

$$\mathbf{u} = \frac{\mathbf{\Delta x}}{\Delta t}. \tag{4.1}$$

Here, $\mathbf{\Delta x}$ refers to the distance an ensemble of particles has moved from one image exposure to the next in the time interval given by Δt.

Under certain conditions, such as when the particle seeding density is so high that particles appear to overlap, a speckle pattern is recorded rather than individual particles. In such cases, we speak of the essentially identical technique, laser speckle velocimetry (LSV). The basic elements of a typical LSV/PIV system are laid out in figure 4-2. The arrangement consists of a light source, a device to modulate this light, a device to transform the light into a two-dimensional sheet, tracer particles in the fluid, a recording medium to capture the light reflected from the particles, and a system to analyze the information.

The manipulation of the light source, hereafter considered to be a laser, can be performed with various possible degrees of complexity. For example, the task of pulsing the light source may be accomplished in one of several ways. Since a large number of experimental facilities possess a continuous laser source, one such way is to employ a mechanical shutter or chopper. Another useful technique is to scan the laser beam through a cross-section of the flow by means of a rotating or vibrating mirror. This method provides both the shuttering mechanism and generates the two-dimensional light sheet simultaneously. When not using a scanning device to strobe the beam, transformation of the laser beam into a two-

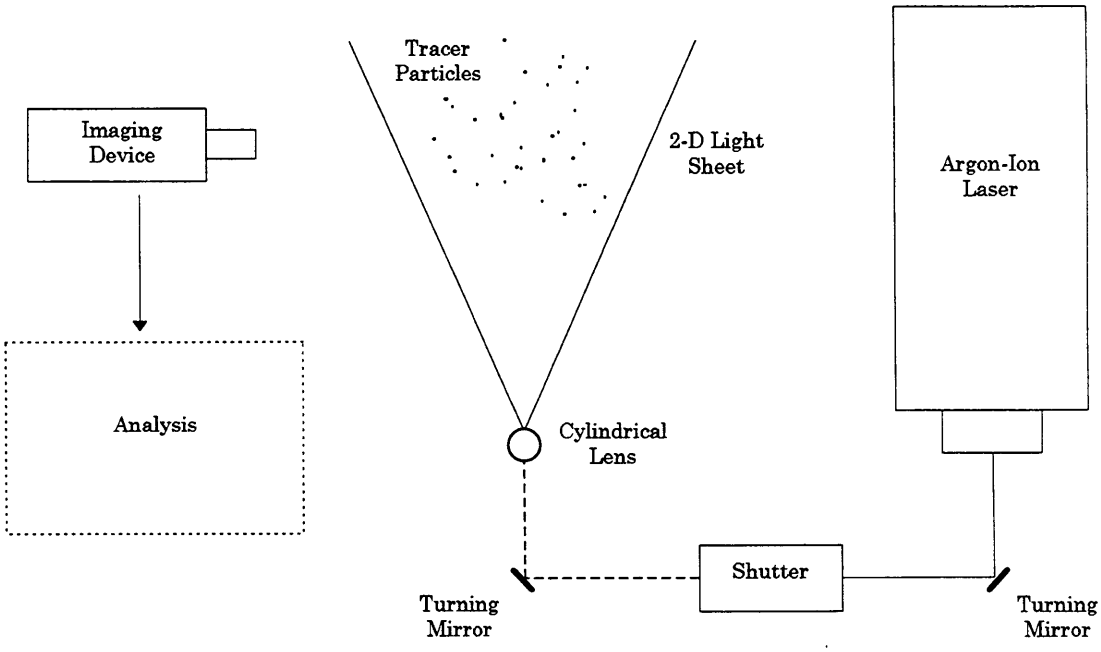

Figure 4-2: Basic elements of a LSV/PIV system. Shown are an argon-ion laser (light source), a hardware controlled mechanical shutter (light modulator), cylindrical lens (forming a two-dimensional laser sheet), flow seeded with reflective particles (flow tracers), and an imaging camera (recording medium).

dimensional laser sheet is typically accomplished by passing the beam through a cylindrical lens.

The utilization of an acousto-optic modulator, or AOM, is yet another option for laser pulsing. By sending the beam through an suitably controlled AOM,[2] the beam can be deflected such that it continues to travel through the primary optical arrangement only when desired. The disadvantage of this type of 'pulsing' is the inherent losses associated with passing the beam through an optical device. Recently, pulsed lasers have become available that can be modulated internally. Such a laser is used in the present set-up, and possible ways to exploit this feature are currently being explored.

Images resulting from the exposure of tracer particles can be stored on several types of media. Photographic plates and film were typical of the methods used a decade ago. The analysis of such images can be performed using a method known as Young's fringe analysis. This technique, statistical in nature, can be applied to both LSV and PIV images. A laser beam is used to mechanically interrogate the images at many locations. A Fourier transformed image of the illuminated region is obtained by passing the diffracted beam through a converging lens and projecting it onto a screen. If the region contains double exposed speckle or particle images, a Young's fringe pattern will be observed. The spacing and angle of these interference fringes correspond directly to the mean displacement vector of the speckle/particle images [57].

The use of double exposed images by LSV/PIV techniques introduces the possibility of directional ambiguity with each velocity measurement. This can become problematic in the case of reversing flows. While efforts to mitigate this difficulty, such as artificial image shifting, have been successfully implemented, they contribute unwanted additional complexity to the analysis. To make LSV/PIV methods more practical and reduce the amount of time involved in making measurements, researchers began exploring video-based techniques during the 1980s. These methods laid the conceptual foundation for a digital implementation of PIV.

[2] An acousto-optic modulator can be easily controlled with a PC equipped with I/O control hardware.

The digital implementation of particle image velocimetry

Digital particle image velocimetry is essentially a digital version of PIV that attempts to solve some of the problems associated with the conventional analog technique. Commonly attributed to Willert and Gharib [57], DPIV has a number of distinctive features: DPIV uses digitally stored video images (*single* exposed) rather than photographic media—by using pairs of single exposed images phase information is retained; proper image exposure is made possible by synchronizing the camera video signal to the laser shutter timing; the analysis is performed computationally, eliminating the arduous tasks of photographic processing and opto-mechanical interrogation of the images; local spatial cross-correlations are performed between the image pairs to yield displacement information directly; finally, a sub-pixel estimator is implemented to determine particle displacements more precisely in an attempt to mimic the intrinsically greater resolution of photographic film.

Quality DPIV measurements rely on the use of high resolution video camera technology. The camera used in the present system has a maximum spatial resolution of 1134 pixels $\times$ 486 pixels. More sophisticated cameras exist which have resolutions on the order of 2k $\times$ 2k pixels. With DPIV, the video from the camera must be digitized and then stored. There are numerous ways in which this may be accomplished. One method is to store the video real-time to VHS/Beta format or laser disc, and then digitize selected images with a PC frame grabbing board. This two-step process is necessary because of current limitations in frame grabber on-board memory. To illustrate this stumbling block, consider a 640 $\times$ 480 image, consisting of 307200 bytes. Since a pair of images is needed to compute each velocity field, 614400 bytes must be stored for each measurement. If standard NTSC video is used and whole *frames* are being correlated, we can expect 15 measurements per second. This yields 9.2 Mb of data for a single second of measurement. Many frame grabber boards can be outfitted (expensively!) with about 20–30 Mb of memory, allowing for only a few seconds of data. There are, however, alternatives to this method of storage. Recently, cost effective PCI (Peripheral Component Interconnect) bus frame grabbers have emerged which allow real-time image digitization and storage to PC system memory. With such a configuration, the number of images able to be stored is only limited by system RAM and is a function of image resolution. Details of such a system are discussed in § 4.3.4.

Once the images have been stored digitally, the remainder of effort is devoted to image analysis. A statistically based approach is undertaken. Local regions of the images are cross-correlated, and information from the peak correlation is used to infer the mean displacement of particles in that region. Implementing the cross-correlation computationally can be done in either the spatial domain or the Fourier domain. Refinements to the measurement can be made by using sub-pixel peak location estimators and data filtering/smoothing routines.

4.3 Experimental set-up and methods

In this section, the DPIV experimental system developed at the Woods Hole Oceanographic Institution (WHOI) is described. There are several novel aspects of this system: optical filtering is used to enhance image quality; a full-frame integrating camera is employed that preserves high imaging resolution; an alternative approach to generating sheets of laser light is adopted; and recent advances in frame grabber technology are exploited to ease the task of image digitization and storage. The entire set-up, which includes the DPIV equipment and visualization tank, resides on a 1.2 m $\times$ 1.8 m optical table.

4.3.1 Particle seeding

The type of tracer particles selected for an experiment affects the ultimate quality of the recorded images. In the present work, the flow was seeded with acrylic spheres that have been impregnated with fluorescent dyes (Rhodamine 6G and fluorescein). These particles, approximately 20–45 μm in diameter, have a specific gravity very near 1.0, and are therefore practically neutrally buoyant.[3] When illuminated with 556 nm light, these particles fluoresce at 576 nm. This property is extremely useful when dealing with near-surface flows because when a light sheet interacts with the surface, significant reflection and interference occur. This results in a portion of the imaged area appearing 'washed out,' or saturated. Using fluorescent particles, this problem can be moderated. An optical filter is used on the camera to block all wavelengths of light except those near the wavelength at which the

[3]In order to achieve a density near 1.0 g/cm^3, air is foamed into the dissolved acrylic during the manufacturing process.

particles fluoresce. Use of such a filter eliminates most of the laser light and its reflections from being imaged by the camera, leaving only particle images to be recorded.

The issue of seeding density was not investigated. Particle seeding can be largely a trial and error process. The ideal seeding density depends on particle size, camera magnification, and size of the camera imaging area. Particle density in the recorded images influences the cross-correlation processing of the image pairs. Depending on circumstances, the processing may dictate seeding, or vice versa.

4.3.2 Illumination and optics

At the center of the WHOI optical system is a diode-laser-pumped Nd:YLF laser which serves as the light source. One of the attractive features of this newly developed laser is its portability; the complete system is powered by standard 110 VAC, is self-cooling, and can be conveniently transported. Conventional multi-watt continuous lasers, such as the argon-ion, are bulky (several feet in length) and require water cooling that needs to be provided from building infrastructure. These strict needs render such lasers practically immovable once installed. The present laser system consists of a floor-standing main control unit (resembling a portable refrigerator in size), a small remote control unit, and the laser head. The main control unit provides power to the pair of 20 W diode-laser bars as well as temperature control for the laser head. Thermal regulation is achieved with a *closed-loop* water-to-air heat exchanger. The controller also provides RF (radio frequency) power to the intercavity AOM for Q-switching. The laser head is connected to the main controller via a 3 m long umbilical. The head unit and supporting DPIV optics are mounted on a 61.0 cm $\times$ 91.4 cm optical bread board. In order to protect the laser head and optics from the imperfect environment of the lab, a laser housing was designed and constructed at WHOI. The housing is just large enough to contain the optical bread board. Three anti-reflective optical ports in the housing allow for beam transmission. The entire unit is sealed and is designed to accept a positive gas pressure input.

The Nd:YLF is a pulsed type laser and is designed to operate in a pulsed mode. The internal pulse rate, or 'rep rate,' of the laser is user-selectable and ranges from approximately 20 kHz to 100 kHz. Greatest power is realized when the laser is operated at the lower

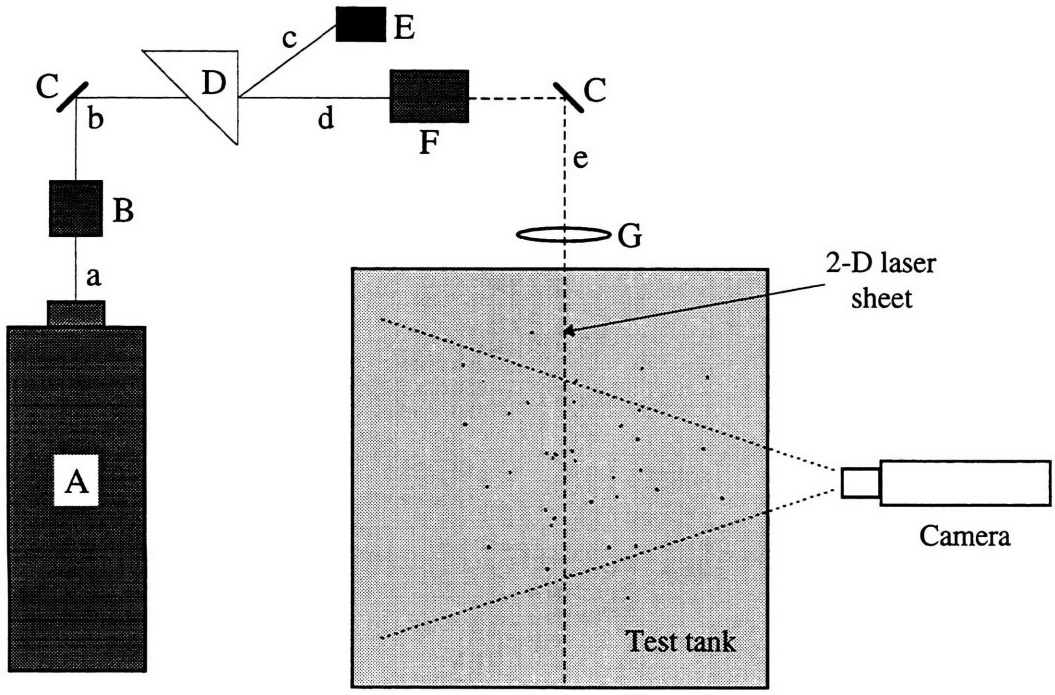

Figure 4-3: Layout of DPIV optics. A: Nd:YLF laser, B: LBO crystal, C: turning mirror, D: prism (refraction angles exaggerated), E: beam dump, F: mechanical shutter, G: Powell lens. Lowercase letters denote different wavelengths and stages of light. a: IR (12 W), b: IR (6 W) and green (6 W), c: IR, d: green, e: shuttered 6 W green.

frequencies. Because the frequencies associated with DPIV are governed by the camera video rate ($\mathcal{O}$(10–10k Hz)), the higher frequency pulsed laser output appears continuous for DPIV application.

The Nd:YLF laser outputs infra-red (IR) light at a wavelength of 1047 nm. At this wavelength, the output power is estimated at 12 W. Since this wavelength of light is absorbed by water and provides zero particle illumination, the beam is frequency-doubled before entering the visualization tank. A complete diagram of the optical set-up is shown in figure 4-3. This figure depicts the complete optical path traversed by the laser beam. After emission from the laser head unit, the IR beam is passed through an LBO (Lithium Borate) crystal which, through nonlinear interaction, excites the beam second harmonic, doubling its frequency and halving its wavelength to 523.5 nm. The optical conversion efficiency of the LBO crystal is approximately 50% and is a function of temperature. Consequently, the crystal is housed in an oven which maintains an optimum temperature of 173.5±1°F. The beam, now composed of both visible green and IR light, is sent through a prism causing

the light to refract. Because their wavelengths are different, the IR and green refract by different amounts. Taking advantage of this behavior, the IR portion of the beam is sent to a beam dump and the green is allowed to continue. The green light is then directed, using wavelength-sensitive turning mirrors, through a computer-controlled mechanical shutter. Discussion of the shutter timing control is covered in § 4.3.3. Once shuttered, the beam is directed to the visualization tank at which point it is transformed into a 1–2 mm thick light sheet. Conversion of the beam to a sheet is accomplished using a Powell lens. Unlike a traditional cylindrical lens which yields a two-dimensional sheet with a Gaussian intensity distribution, the Powell lens is specifically designed to produce a uniformly distributed sheet. This feature is desirable since the Powell lens causes all particles in the sheet to be equally illuminated.

4.3.3 Shutter timing control

Modulation of the laser beam is achieved using a simple computer-controlled mechanical shutter. The shutter requires a TTL level input signal to control its opening/closing operation. The device has a rise time of 0.2 ms and a fall time of 0.4 ms. As eluded to earlier, the key to the shutter timing lies with synchronization to the camera video. A few words on the camera used in the present system are in order. The WHOI set-up utilizes a high resolution (1134 pixels × 486 pixels × 8 bits) black and white video camera with a standard f1.7 lens. This camera has several modes of operation; for our purposes, it is operated in a 'dual-field mode.' In this simultaneous field[4] capture mode, the entire CCD image sensor is exposed for 1/30 of a second. Both fields are exposed simultaneously, stored on-chip and, after readout, form a *frame* having true interlace without the time-dependent image offset that occurs in standard field-mode operation. In terms of DPIV application, this means that rather than correlating two video fields, where the vertical resolution of the images is half that of the camera, two frames are able to be used, preserving the high resolution video and eliminating interlace offset.

The goal of laser shuttering is to place single light pulses in each video frame with a

[4]In standard NTSC video, two fields are vertically interlaced to form a complete frame. Camera video having a pixel resolution of 640 × 480 is composed of two 640 × 240 fields. Fields are acquired and displayed at 60 Hz, making the frame rate of the camera 30 Hz.

specified regularity. The duration of each pulse, as well as the spacing between pulses, are functions of flow speed, particle seeding, and camera magnification. Typical shuttering patterns rely on two closely spaced pulses that straddle the video frame transfer marker. Pulse lengths and separation are on the order of 2–20 ms. A canonical scenario is shown in figure 4-4. There are two features illustrated in this figure. The first is the video–shuttering synchronization. The vertical drive signal from the camera is sent to an I/O board in a PC. This signal contains the frame transfer marker information. Simple computer code is used to locate the beginning of each new frame and generate the proper output signal for the mechanical shutter based on the desired timing pattern. The second feature depicted in figure 4-4 is one of the underlying principles of the DPIV process. Each frame of camera video is illuminated with a single light pulse. This creates a single DPIV exposure. Subsequent pairs of DPIV images, denoted in the figure as "A" and "B," are then processed computationally to yield a two-dimensional velocity field.

4.3.4 Imaging and data storage

The current DPIV system uses imaging hardware and software developed for the PCI bus. The frame-grabbing board digitizes standard analog camera video at 640 × 480 resolution into 8 bits/pixel. The imaging software allows a sequence of frames to be digitized and stored to system memory (RAM) in real-time. The lab PC dedicated to imaging tasks is equipped with 64 Mb of RAM; this amount of memory can store 6.9 seconds of fully sampled camera video at the digitizing resolution of 640 × 480. Since a typical vortex ring–free surface interaction event lasts 4–5 seconds, this amount of data is adequate.

The task flow for a typical vortex ring experiment is given by figure 4-5. An experiment begins with the generation of a ring. The ring is created with the computer-controlled piston actuator arrangement described in § 3.3. Once the PC has given the command to generate a ring, it sends a TTL trigger to the frame grabber to commence digitization and storage. Simultaneously, the camera is continually providing its vertical drive signal to the timing PC which controls the laser shuttering. Camera video is sent to the frame grabbing board for storage and display. Shown in figure 4-6 is a sample DPIV image taken with the WHOI DPIV system.

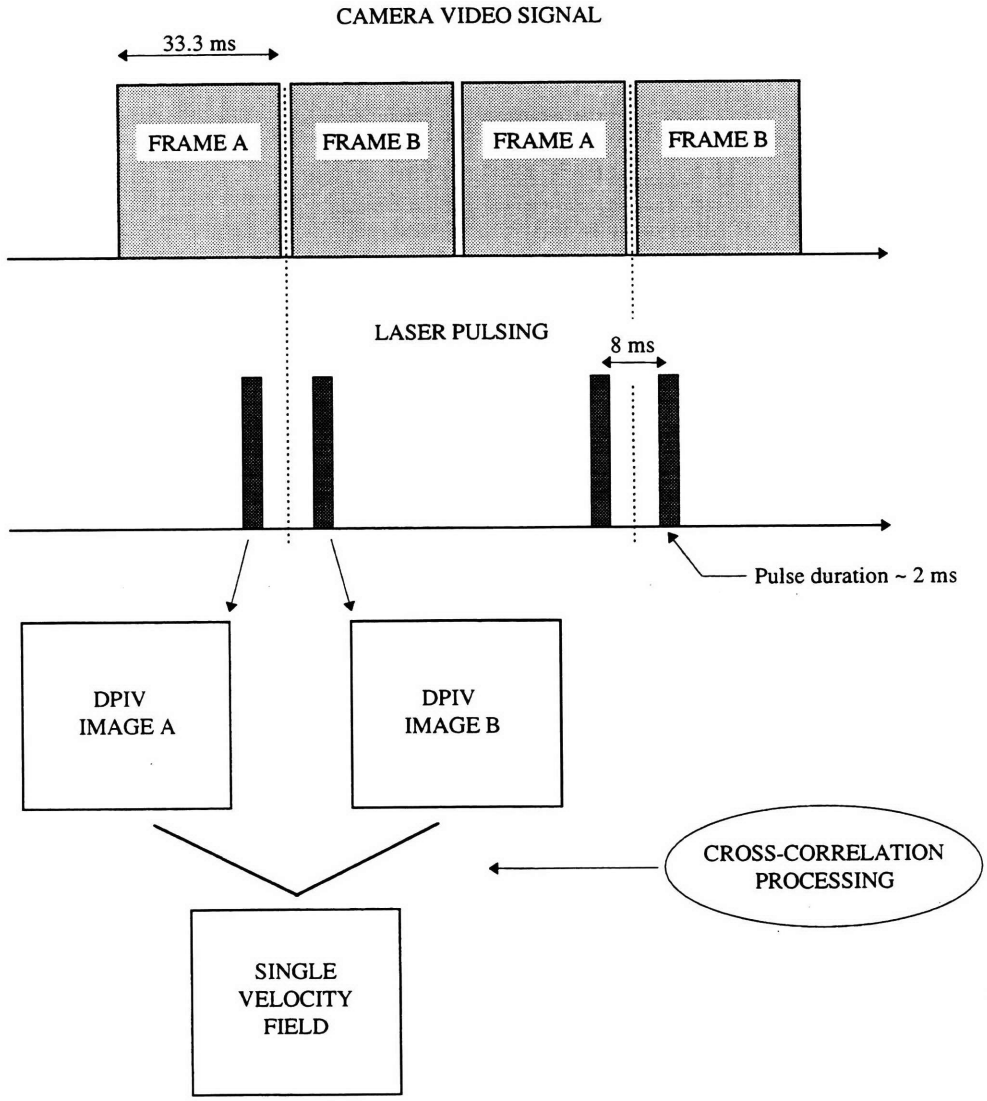

Figure 4-4: Schematic of laser pulse timing and DPIV process. Uppermost timeline shows camera video signal. Frames are arbitrarily designated as "A" and "B" for illustration. Frame rate is 30 Hz. The timeline below indicates a corresponding light pulsing example: 2 ms pulses are placed on either side of the frame markers (dotted lines) with 8 ms spacing. The illumination of each frame with a single light pulse yields one DPIV image. Subsequent pairs of DPIV images are processed to produce a two-dimensional velocity field.

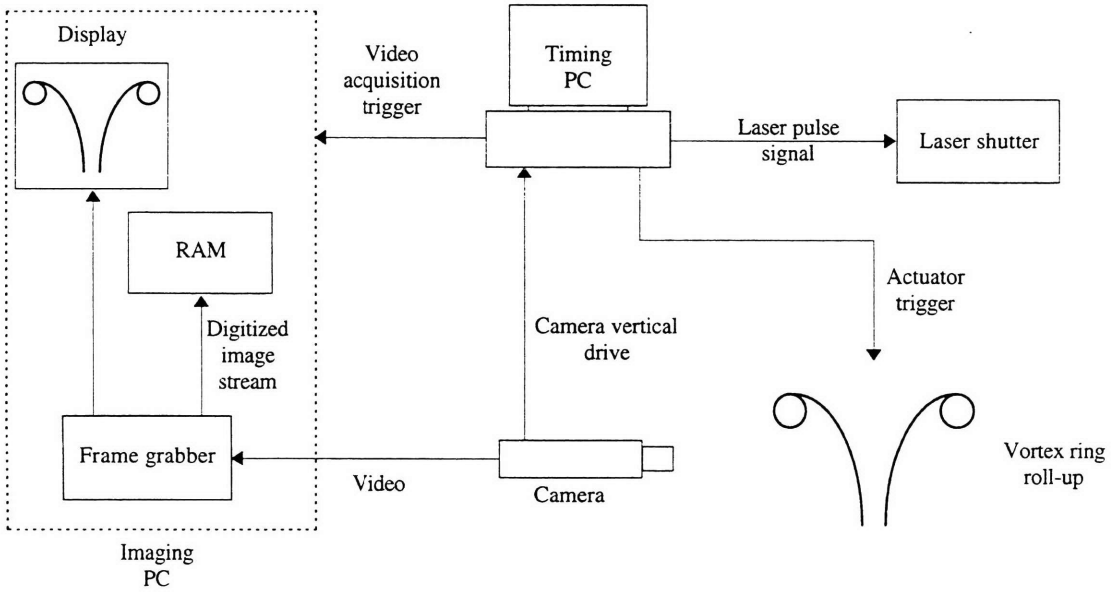

Figure 4-5: Task flow diagram for a typical vortex ring experiment.

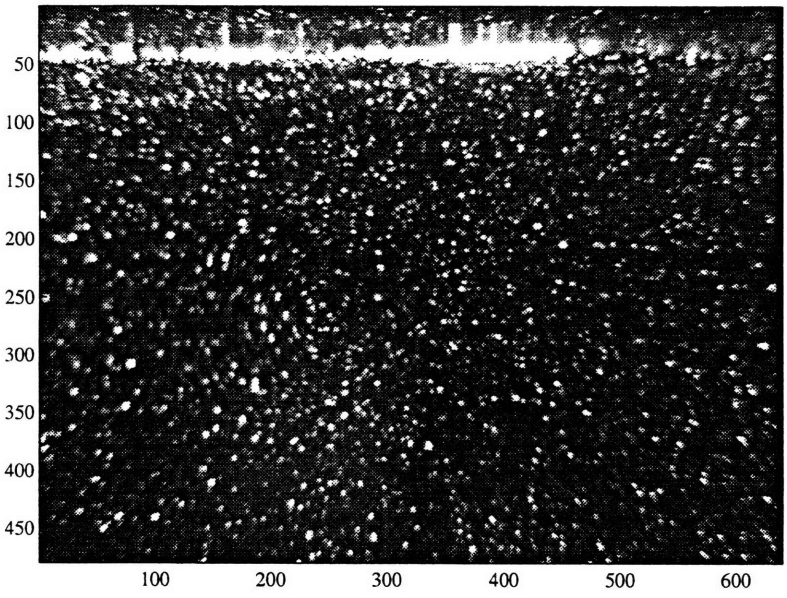

Figure 4-6: Sample DPIV image of vortex ring approaching the free surface. Only one half of the ring is being imaged. The bright area near the top indicates the free surface. The vortex core can be seen near pixel coordinates (240, 260). Image resolution is 640 $\times$ 480.

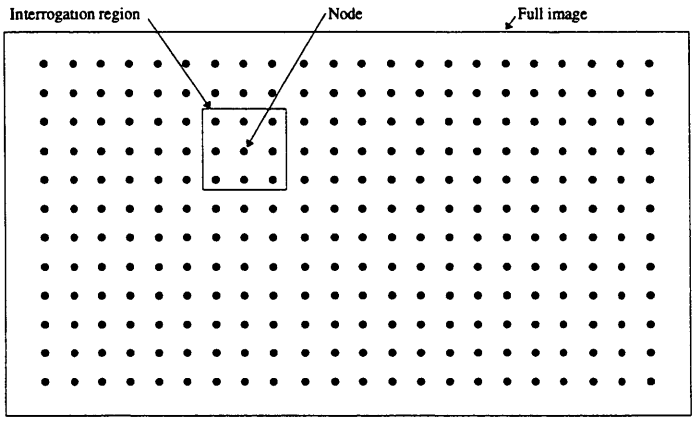

Figure 4-7: DPIV windowing scheme. A computational grid is created for the DPIV image and the full image is divided into many sub-images, or "interrogation regions," whose centers correspond to individual nodes. Local mean displacements are computed at each node using the information contained in A–B pairs of interrogation regions.

4.4 Analysis of image data using a cross-correlation method

4.4.1 The theory of statistical correlation

Once image pairs have been stored, they must be processed to yield velocity information. Computationally, the digitized images are considered two-dimensional arrays of integer values ranging from 0 to 255. As such, they can be treated in an analogous manner to other two-dimensional data arrays. The displacement field for the complete image is computed piecewise locally on a grid of nodes by examining smaller sub-images centered at each node. These sub-images are commonly referred to as "interrogation regions" or "windows." The windowing scheme is explained in figure 4-7, and § 4.4.2 outlines the grid generation methodology. Examining these sub-images, an average spatial shift of particles may be observed from one interrogation region (in image A) to its counterpart in the subsequent image (image B). Determining the pixel offset between A–B window pairs is accomplished using the statistical technique of cross-correlation. Cross-correlation is a mathematical measure of 'goodness of match' between two sets of data, in this case sub-images. Typically, cross-correlation techniques are used to locate a known image subset in a larger image (template matching). For example, if one was interested in finding the character ♣ in an image of text the template becomes the image of the symbol ♣. One then simply slides the template

over the image area to be searched, computing the correlation at each step. Positions with high correlation peaks indicate a match of the character ♣. DPIV uses cross-correlation in exactly the same manner: the template in this case is the interrogation window from image A, and the image to be searched is an appropriate sub-region of image B. In two dimensions, the discrete cross-correlation between two real-valued functions, $f(x,y)$ and $g(x,y)$, is given by Gonzalez [27] as

$$\Phi_{fg}(x,y) = f(x,y) \circ g(x,y) = \sum_{m=0}^{M-1} \sum_{n=0}^{N-1} f(m,n)g(x+m, y+n), \tag{4.2}$$

for $x = 0, 1, 2, \ldots, M-1$ and $y = 0, 1, 2, \ldots, N-1$. Equation 4.2 expresses the correlation between sampled regions, f and g, of dimensions $A \times B$ and $C \times D$ respectively. These regions are assumed extended and periodic with periods M and N in the x and y directions such that $M \geq A + C - 1$ and $N \geq B + D - 1$. In an image framework, the indices (x,y) and (m,n) refer to pixel coordinates. The actual implementation of the cross-correlation in the code written as part of this work uses a slightly modified version of (4.2) which does not enforce the strict rules of periodicity.

Cross-correlation can be performed in either the spatial domain or in the Fourier domain. Because of the substantial reduction in computational effort, the latter domain is often preferred. In frequency space, the double summation in (4.2) is replaced by a complex conjugate pointwise multiplication of the two-dimensional Fourier transformed image subsets. This is expressed by the correlation theorem

$$f(x,y) \circ g(x,y) \Leftrightarrow F(u,v)G^*(u,v), \tag{4.3}$$

where F denotes the Fourier transform of the function f, and G^* represents the complex conjugate Fourier transform of the function g.

In the spatial domain approach, in order to compute a meaningful measure of the correlation between two sub-regions, a correlation coefficient is employed. The coefficient has the effect of properly normalizing the correlation based on the functions f and g. Such normalization is critical when performing the correlation in the spatial domain since the function g takes on a different ensemble of values at each distinct (m,n) step. The cross-correlation

coefficient, C_{fg}, is given by

$$C_{fg}(x,y) = \frac{[f(x,y) - \bar{f}] \circ [g(x,y) - \bar{g}]}{\sqrt{\sum_{m=0}^{M-1} \sum_{n=0}^{N-1} [f(m,n) - \bar{f}]^2 [g(m,n) - \bar{g}]^2}}. \tag{4.4}$$

The quantities $\bar{f}$ and $\bar{g}$ are the respective subset means defined by

$$\bar{f} = \frac{1}{MN} \sum_{m=0}^{M-1} \sum_{n=0}^{N-1} f(m,n)$$

and,

$$\bar{g} = \frac{1}{MN} \sum_{m=0}^{M-1} \sum_{n=0}^{N-1} g(m,n).$$

The coefficient C_{fg} can range continuously from -1 to 1. A value of 1 indicates "complete positive correlation" and a value of -1 indicates "complete negative correlation." A correlation coefficient value of zero means the two regions are "uncorrelated." A high correlation coefficient near unity is observed where many particle images match up with their corresponding shifted partners. The strongest correlation peak is considered to represent the best match of particle images between regions f and g.

An example of the correlation process using a spatial domain correlation algorithm is illustrated in figure 4-8. Two sub-images are shown, and the resulting correlation surface is contoured. This surface was generated by correlating the template window in image A with $32^2 = 1024$ neighboring windows in image B (only one of which is shown in this figure—the window producing the peak correlation). Each computation yields a single coefficient value. (The result using an FFT approach is very similar.) The location of the peak maximum indicates the *mean* displacement of particles from window A to window B. In this particular case, the pixel shift is given by $dy = -3$, $dx = +2$. With the displacement vector components known, and assuming the Δt of the laser pulses is also known, (4.1) gives the velocity vector for that particular node.[5] The remainder of the image is processed identically.

There exist a few subtle, yet important, differences between correlation techniques in

[5]Also needed for proper calculation of a velocity vector are the camera video squareness ratio (which reflects the pixel aspect ratio) and a conversion between camera pixels to physical units.

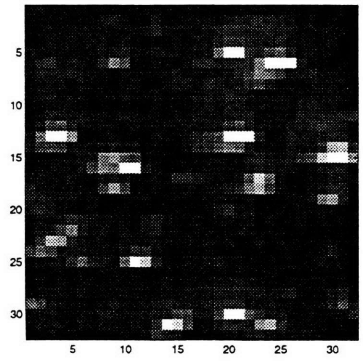

Window A

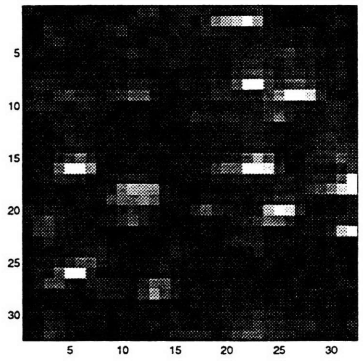

Window B

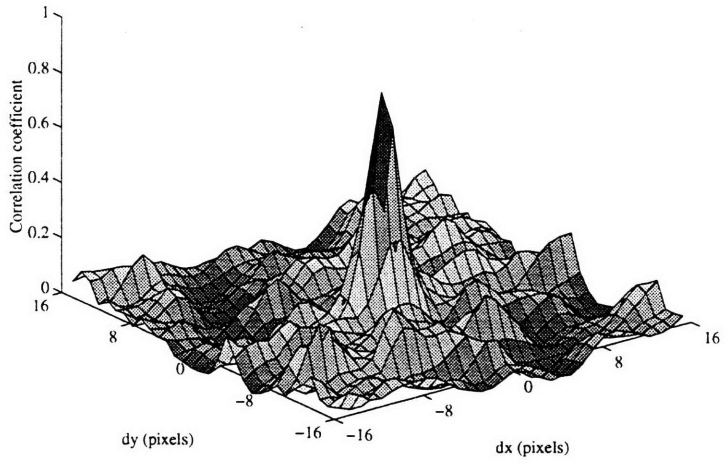

A-B Correlation

Figure 4-8: Spatial cross-correlation of two 32×32 sub-images (above). Correlation surface is shown below. The negative DC offset has been removed from the correlation surface—this is done in order to facilitate an accurate Gaussian curve fit to the peak (see § 4.4.3). The peak maximum indicates a mean particle displacement of $dy = -3$, $dx = +2$. Other smaller spurious peaks may be the result of particle pair mismatch, out-of-plane motion, and/or particles entering or leaving the interrogation windows.

the spatial domain and techniques in the frequency domain. First, typical canned Fast Fourier Transform (FFT) routines require array sizes which are powers of two. This forces the condition, $M = 2^{\alpha}$, $N = 2^{\beta}$, whereas in spatial routines, M and N may be arbitrary. Second, in order to correlate an $M \times N$ sub-image from image A, only the corresponding $M \times N$ sub-image in image B is used with an FFT implementation. A spatial domain approach requires a larger 'search' region in the second image to calculate the same correlation field. The 'brute force' searching within this larger region is what causes the spatial domain technique to be much more computationally intensive. Although slower, the spatial approach has its advantage in accuracy—since the FFT method uses only a single window from the second image, particles may enter/leave this region of interest and 'confuse' the FFT correlation result. However, by actually searching the surrounding region using many window pairs, the spatial domain method incorporates this additional information into the calculation, typically yielding a better result. More information on the accuracy and efficiency of the two methods is discussed in § 4.4.5.

4.4.2 Grid generation

The grid used in computing the displacement field is affected by the type of correlation routine being used. Spatial domain cross-correlation requires a search region in image B which is at least as large as the sub-image from image A so that this template can be 'tiled' up/down and left/right as individual correlations are computed. This requirement dictates how near the image edges nodes can be located. Correlation in the Fourier domain does not require such a search region in the second image, and as a consequence nodes may be located nearer the image borders. To locate node positions, several parameters must be considered: template window size, maximum expected particle displacement when using a spatial domain correlation algorithm (used to select search region size), vertical spacing between nodes, and horizontal spacing between nodes. Figure 4-9 shows two possible grids for a 768 $\times$ 480 image using a spatial domain correlation algorithm. In (a), the 32 pixel node spacing produces interrogation windows that do not overlap. The finer grid in (b) is the result of over-sampling the image by having interrogation regions overlap by half the window size. In both cases, by choosing the search box size twice that of the template, a

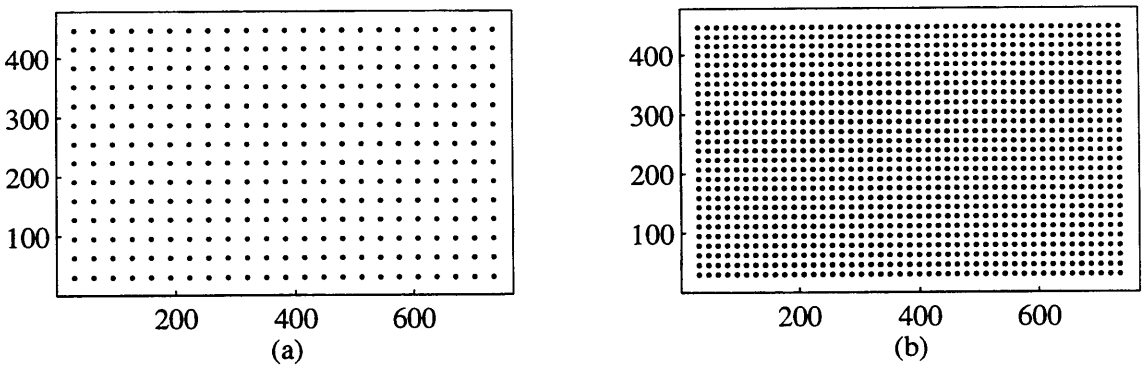

Figure 4-9: Two grid examples for a 768 × 480 image. The parameters used in (a) are: 32 × 32 template size, a search region in image B of dimensions 64 × 64, and node spacing of 32 pixels in both x and y directions. The parameters used in (b) are: 32 × 32 template size, a 64 × 64 search region, and node spacing of 16 pixels in both directions.

maximum pixel displacement of half the template size is able to be determined.

Window overlap leads to the issue of independent measurements. When overlapping is used, 'old' information is used to compute correlations, and in this way, not all measurements can be considered independent. The number of truly independent measurements for an image is the integer number of interrogation windows that can fit in the image with zero overlap. Figure 4-9 (a) contains $14 \times 23 = 322$ vectors, all of which are independent since overlap is avoided. Figure 4-9 (b) contains $27 \times 45 = 1215$ vectors. Of those 1215, only 322 are independent. Care must therefore be taken when interpreting fine grid output. Although they may produce attractive results, fine grids use the same amount of information as coarser grids. Furthermore, excessive window overlap can give the impression of false enhanced resolution (see § 4.4.5).

4.4.3 Improvements to the measurements

Sub-pixel accuracy

Once a displacement vector is determined for a local region of particles, this estimate can be improved by locating the center of the correlation peak to sub-pixel accuracy. As evidenced by figure 4-8, the resolution of x and y displacements is limited to an integer number of

pixels. In most instances, greater spatial precision is needed in order to avoid significant relative errors. The DPIV code used here fits a Gaussian shaped curve to the correlation peak, and locates the maximum of this curve-fit to sub-pixel accuracy. Specifically, a three-point Gaussian sub-pixel estimator is used separately in both directions, centered about the initial correlation peak estimate. In total, five values are used in locating the (x, y) sub-pixel center of the peak. The estimating function implemented in the present analysis is given below [14]:

$$x_i = \frac{(\xi_2^2 - \xi_1^2)\ln(\gamma_2/\gamma_3) - (\xi_3^2 - \xi_2^2)\ln(\gamma_1/\gamma_2)}{2[(\xi_2 - \xi_1)\ln(\gamma_2/\gamma_3) - (\xi_3 - \xi_2)\ln(\gamma_1/\gamma_2)]}, \tag{4.5}$$

where

$$\begin{aligned} x_i &= \text{the sub-pixel estimate of peak center,} \\ \xi_1, \xi_2, \xi_3 &= \text{the pixel locations of the left of peak, center, and right of peak intensity} \\ \gamma_1, \gamma_2, \gamma_3 &= \text{the intensity values at } \xi_1, \xi_2, \xi_3. \end{aligned}$$

The use of Gaussian shaped fits for DPIV has been successful, and this is not surprising since the particle image intensities are Gaussian distributions themselves. Consequently, the correlation peaks are expected to be Gaussian as well.

Post-processing the velocity data

In the DPIV code written for the present work, two optional operations that can be performed on the computed two-dimensional velocity field are (1) outlier removal, and (2) data smoothing. With the former, outlier data points in the velocity field are removed. In the actual computer code, this routine takes as an argument a pixel threshold value whose exceedance is used in determining outliers. For each point in the field, the velocity differences to each of the eight surrounding neighbors are computed. If the differences exceed the threshold for four of the eight neighbors, the data point is flagged as an outlier and is re-interpolated by linear interpolation.

The second operation uses a spatial filter that is passed over the entire data field to

remove high frequency jitter inherent to the DPIV processing. The routine takes two arguments, one specifying the filter size, the other specifying the filter type (average or weighted average). This filter does not remove any information if the data are sufficiently over-sampled to begin with, *i.e.*, the step size is at most half of the template window size [4].

4.4.4 The WHOI DPIV code

As part of this work, code was written in the C programming language that performs all the functions associated with the analysis of DPIV image data. Both a 'brute force' spatial cross-correlation algorithm and an FFT cross-correlation algorithm were implemented. The code takes as input the pair of images to be processed and a parameter file which drives the individual routines. Specified in this parameter file are values such as:

- Full image size
- Coordinates of the region to be processed
- Type of correlation algorithm flag
- Template and search window sizes
- Horizontal and vertical node spacing
- Outlier threshold
- Filter type flag and size
- Camera squareness ratio
- Physical length conversion factor
- Temporal spacing between image exposures

A flow chart diagramming the code execution is shown in figure 4-10. In operating the code, an attractive feature of a spatial domain correlation is the freedom it allows when choosing certain processing parameters. In the spatial domain, restrictions on window sizes do not exist, making this method adaptable to any number of correlation strategies.

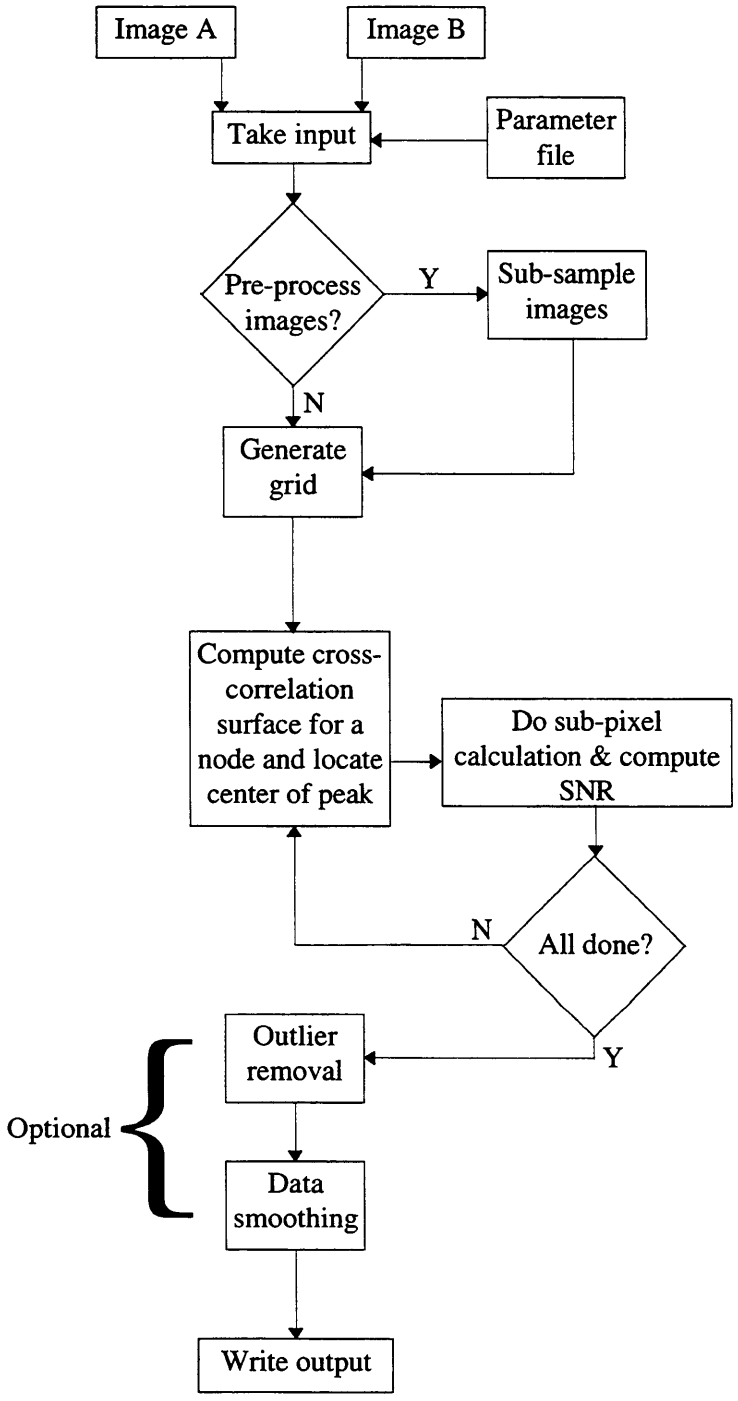

Figure 4-10: Flow chart showing WHOI DPIV code execution.

In addition to velocity and position data, the WHOI DPIV code produces a file which contains estimates of the local signal-to-noise ratio (SNR) for each velocity measurement. The local SNR provides a measure of the quality of the peak used in determining the mean particle displacement. For these purposes, the SNR has been defined

$$\mathrm{SNR} = 20 \log_{10} \frac{S_{2\sigma}}{N}. \tag{4.6}$$

In this definition, $S_{2\sigma}$ reflects the summated values of the peak surface contained within two standard deviations[6] of the peak center, normalized by the corresponding area. The term N accounts for the remaining peak surface values, normalized by the appropriate complementary area. Finally, shown in figure 4-11 is a vector plot of the velocity field corresponding to the image from figure 4-6.

4.4.5 DPIV resolution and uncertainty

Resolution

The temporal resolution of DPIV is fixed by the camera video rate. The camera utilized in this work, operated in dual-field mode, yields a video frame rate of 30 Hz. Since two frames are needed for each velocity field measurement, one can expect a 15 Hz data acquisition rate for fully-sampled-in-time camera video (*i.e.*, frames are not skipped during image acquisition).

DPIV spatial resolution is somewhat less straightforward. The size of the interrogation window has no direct effect on the spatial resolution of the technique. In fact, as with any flow measurement technique involving tracer particles, the best achievable spatial resolution is limited by the average spacing between particles. The effect of the DPIV windowing process is that of a spatial low-pass filter; spatial wavelengths smaller than the window dimensions are increasingly suppressed. This is problematic when the flowfield considered has fine scale motions or flow reversals such as near a vortex core. To properly resolve such small scale features, the camera view should be enlarged or the window size should be

[6] An axisymmetric Gaussian curve-fit is applied to the four points nearest the peak to determine an estimate of the two-dimensional standard deviation.

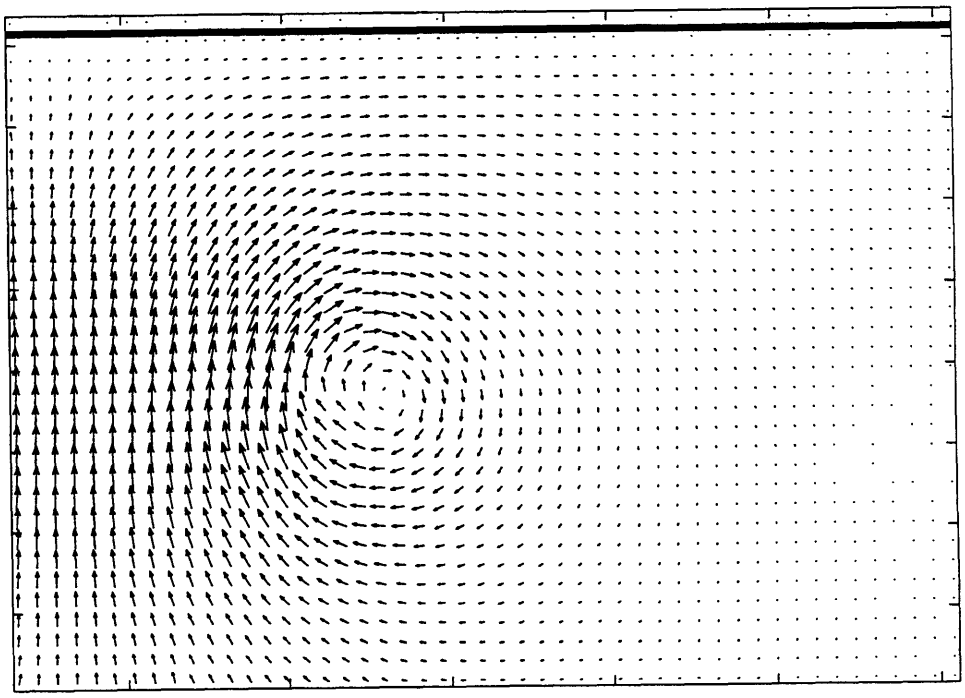

Figure 4-11: Velocity field corresponding to the image in figure 4-6. The thick solid line near the top indicates the position of the free surface.

reduced appropriately. Willert and Gharib [57] present an analysis of the spatial wavelength response of their technique (an FFT-based method). Examining a subset of their results, we observe a 40% attenuation of features on the order of 64 pixels when a 32×32 window is used in the processing. The attenuation is limited to approximately 10% for features nearing 160 pixels in size. Similarly, for a 16×16 processing window, features on the order of 32 pixels are attenuated by approximately 30%, and a 10% attenuation is realized for features near 75 pixels in size. These results must be kept in mind when interpreting DPIV data for scales less than twice the window size.

The lower bound on the stepping increment for the interrogation window should be no less than the mean particle separation. Stepping in increments smaller than this limit gives false enhanced resolution. For instance, if the mean separation between particles is 4 pixels, stepping the window by a single pixel is meaningless, since (on average) no new particles will enter the processing domain. New data is provided only when new particles enter the window. From Nyquist sampling theory, the finest scale spatial feature one can then resolve will be twice the stepping increment.

In summary, two key parameters will determine the degree and quality of spatial resolution possible with DPIV: (1) window size, and (2) step size. Both must be specified correctly if one is to resolve the desired scales of motion. Smaller window sizes *do* possess the ability to resolve larger wavenumber features, however caution must be taken here: as the window size becomes increasingly smaller, two negative effects begin to emerge. First, less particle information is being used in the processing statistics (smaller sample size). Second, a greater fraction of particles are being truncated at the window edges. Both of these factors result in additional errors. Therefore, the window size should be chosen such that it contains a sufficient number of particles and is robust to noise,[7] while still being small enough so as not to suppress/attenuate desired wavenumber features. High spatial resolution will necessarily require small stepping increments. Computation time allowing, the step size should follow the rule mentioned above: choose the step size equal to the mean particle spacing.

[7]DPIV noise in this case refers to particles leaving the window, out-of-plane particle motion, velocity gradients within the window, particle truncation, and poor image signal-to-noise ratio.

A final note on resolution involves the maximum particle displacement resolvable. In the frequency domain, due to the periodicity of the Fast Fourier Transform, the maximum resolvable displacement using a square processing window of size N pixels is given by $N/2$. Again, this limit arises from the Nyquist criterion. When using a spatial domain algorithm, the maximum resolvable displacement is determined by the dimensions of the search region relative to that of the template window, and can exceed $N/2$.

Uncertainty

DPIV is subject to many sources of error, both experimental and computational. The factors which contribute most to the displacement error are: particle image size, interrogation window size, seeding density, and flow gradients within the interrogation region. There must be enough particles inside a window in order to get a sharp correlation peak that is insensitive to noise from loss of particles out of the image plane and out of the interrogation region. Background image noise tends to attenuate the amplitude of the correlation peak, and spatial gradients inside the window will broaden the peak. Other lesser sources of error include instrument performance characteristics, quantization effects, and computational round-off error [4].

In order to quantify the errors associated with the DPIV implementation at WHOI (both the hardware and the software), a set of *simulated* DPIV images were collected. To accomplish this, two 'DPIV' images were created by speckling white paint on a black background. The resulting pattern resembled a DPIV image acquired using the complete system described previously. Each 'flow image' was individually mounted to the computer-controlled rotation stage discussed in § 2.4.1. The camera was set up to acquire static 'snapshots' of the speckle images. Each image was then rotated in various degree increments (0–2°) to effect the appropriate 'particle' displacements. This circular 'flow' therefore provided a range of particle displacements in a single instant, and avoided the need for collection of multiple linear translation image displacements. The results obtained from these rotations provide for the discussion below.

Willert and Gharib [57] estimate a statistical uncertainty using their DPIV technique of 0.01–0.03 pixels. The range indicated is determined by the degree of particle seeding

in the images. Statistical errors near 0.01 pixels were observed for 'good' seeding cases (greater than 20 particles per 32 × 32 interrogation window); errors nearing 0.03 pixels were observed for 'poor' seeding cases (less than 10 particles per 32 × 32 window). The analysis of the error associated with the WHOI DPIV code (operated in FFT mode for sake of comparison) indicated a statistical uncertainty of approximately 0.04–0.05 pixels for a seeding density of roughly 40 particles per 32 × 32 window. (A similar result was obtained for the case of a 16 × 16 window size.)

Using the Willert and Gharib results for 32 × 32 windows, we estimate a *mean* root-mean-square (RMS) relative error of 5–6% for particle displacements in the *range* of 0–9 pixels; absolute errors ranged from 0.01 pixels to 0.15 pixels. The relative error is quite large for the small pixel displacements (on the order of 20%), while it is significantly reduced for the larger displacements (less than 2%). These values correspond to seeding densities between 20 and 70 particles per 32 × 32 window. Increased seeding densities beyond 20 particles per 32 × 32 window show no marked improvement in uncertainty. The WHOI DPIV code, using the FFT correlation routine, yields slightly worse results for mean RMS relative error for a range of displacements: 8.5% for a 0–5 pixel range, and 7.6% for a 0–8 pixel range. (For the case of a 16 × 16 window, mean RMS relative errors were found to be 16.8% for a 0–5 pixel displacement range.) When a spatial domain correlation is employed, the uncertainty is reduced by roughly a factor of two: 5.2% for the 0–5 pixel range, and 3.3% for the 0–8 pixel range using a 32 × 32 window. (For the case of a 16 × 16 window, mean RMS relative errors were found to be 5.6% for the 0–5 pixel displacement range.)

These results would seem to indicate a somewhat poor performance by the WHOI DPIV code. The differences in the test images used by Willert and Gharib and in the present analysis most likely accounts for this. For an improved comparison, we were able to acquire a DPIV software package from the MIT Ocean Engineering Testing Tank. This package was developed by Willert and Gharib, and is closely based on the code used in their 1991 work. Tables 4.1 and 4.2 reflect a comparison between the WHOI DPIV code (using both implementations of cross-correlation) and the MIT DPIV code (FFT implementation). Both codes processed the same test images.

RMS relative errors were obtained by determining the theoretical displacements for the

Image 1: 34 particles per 32 × 32 window			RMS relative error (pixels)		
Window size	Rotation (deg)	Displ. range (pixels)	FFT	Spatial	MIT DPIV
16 × 16	1.0	0–6.3	0.3000	**0.0442**	0.3038
32 × 32	1.0	0–6.3	0.0822	**0.0413**	0.0836

Table 4.1: Comparison of DPIV algorithm results for test image 1. The columns for FFT and spatial results correspond to the WHOI code performance. Values in bold indicate the smallest error.

Image 2: 54 particles per 32 × 32 window			RMS relative error (pixels)		
Window size	Rotation (deg)	Displ. range (pixels)	FFT	Spatial	MIT DPIV
16 × 16	0.5	0–2.6	0.1089	**0.0690**	0.1253
32 × 32	0.5	0–2.6	0.0947	**0.0683**	0.1086
16 × 16	1.0	0–5.6	0.0936	**0.0549**	0.0958
32 × 32	1.0	0–5.6	0.0780	**0.0465**	0.0813
32 × 32	2.0	0–10.3	0.0735	**0.0199**	0.0742

Table 4.2: Comparison of DPIV algorithm results for test image 2.

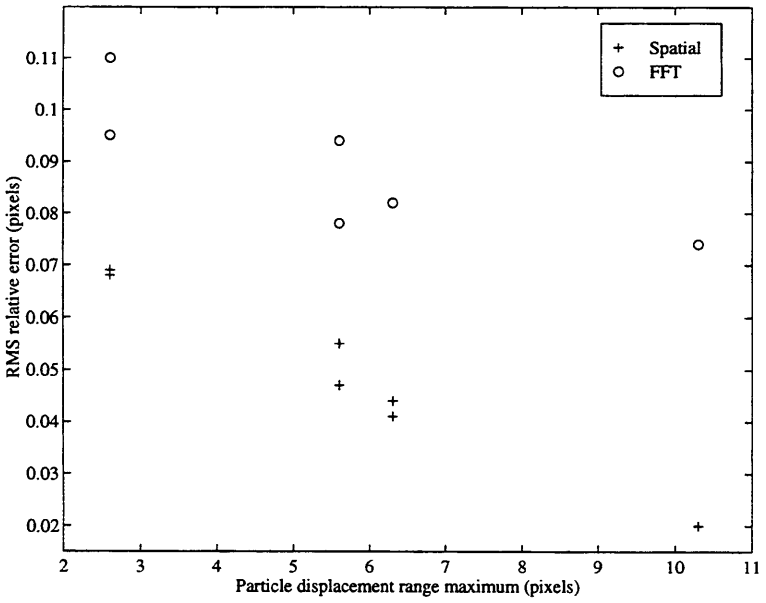

Figure 4-12: Relative displacement error as a function of particle displacement range for the WHOI spatial and FFT correlation algorithms. Results from both processing window sizes shown.

individual image sub-regions based on the amount of rotation and distance from the origin. The spatial mean of the RMS relative errors for each case is reported in these two tables. The most dramatic aspect of these results is the significant gain in accuracy that is realized with the WHOI spatial correlation method. Relative errors are reduced by nearly 50% in all cases when the spatial technique is chosen over the two FFT-based routines. The results for the two WHOI correlation schemes are shown in figure 4-12. The virtually identical results of the WHOI FFT code and the MIT DPIV code provided verification for the WHOI code. As expected, relative errors are observed to decrease with increasing particle displacements (see figure 4-12). For both simulated particle seeding densities considered here, the uncertainty associated with the technique was reduced when using the larger of the two processing windows. The effect of seeding density was not apparent from this set of results.

Rotational errors were also estimated by Willert [56] and in the present study; this was another benefit to using rotated images rather than translated images. The errors

under circular flow conditions were considered to be important to this work because of the type of fluid structure being investigated—the vortex ring. Using the statically rotated images, the vorticity, $\omega = 2\theta$, where θ is the amount of rotation in radians, was computed theoretically and then estimated from the DPIV velocity data. Willert reports relative errors in this measurement of 5–10% for rotations of 0.0 to 0.3 radians. Tests of the WHOI code were able to reveal errors for two rotations: 0.01745 and 0.03491 radians (1 and 2 degrees respectively). The relative errors observed were slightly lower: 4–6% for both methods of correlation—the results provided by the spatial domain correlation were marginally better than the FFT correlation results. These tests were performed with 32 $\times$ 32 windows and 75% oversampling (*i.e.*, 8 pixel shifts between nodes).

Based on these results, it can be argued that a spatial domain cross-correlation scheme is to be preferred over an FFT approach because of the improved accuracy such a scheme provides. A separate set of tests (using numerically translated actual DPIV images) which examined the relative accuracy of the FFT method versus the spatial domain method revealed that the FFT correlation technique consistently underpredicts the particle displacements. This discrepancy owes to the fact that the FFT algorithm does not actively 'search' for template matches, and consequently particles tend to leave (and enter) the FFT interrogation window. This has the effect of limiting the offset of the correlation peak, thus underpredicting the mean particle displacement.

The major drawback to a spatial domain technique, however, is the severe computational cost involved. For example, processing a 640 $\times$ 480 image with 16 $\times$ 16 windows consumes 61 seconds[8] with a spatial domain algorithm and only 4.5 seconds with an FFT algorithm (approximately 13 times faster). In the case of a 32 $\times$ 32 window, the FFT algorithm becomes 25 times more efficient! Because of this accuracy–speed dilemma, one must determine which aspect is more important when selecting a processing method.

[8]The computational times reported here are the result of processing with a 100 MHz Pentium PC.

4.5 Summary

This chapter has described the technique of digital particle image velocimetry and its implementation for the present work. Two methods of performing the spatial cross-correlation operations that are intrinsic to the analysis of the DPIV image data were examined for accuracy and efficiency. One method employs the numerically intensive two-dimensional correlation directly in the spatial domain, while the other performs the correlation in the Fourier domain using an FFT routine. It is shown that the spatial domain approach yields results that are more accurate (by a factor of 2) when compared to the FFT method. The FFT routine, however, is substantially more efficient (by an order of magnitude). While in earlier years this time savings necessitated the analysis be done in the Fourier domain, the computing power of today's machines can begin to make spatial domain correlation a viable alternative that produces higher quality results.

Chapter 5

Near-surface vortical interactions

5.1 Framework of the results

In this chapter, we report the near-surface interactions of a vortex ring as observed using the DPIV technique. The same group of free-surface conditions described in § 3 were also studied here; wave measurements were conducted immediately following each vortex ring interaction experiment in order to characterize free-surface behavior. An additional interfacial condition, that of a solid boundary, was also examined for comparison. Hereafter, the various interfaces are referred to as: "clean," "monolayer 1" ($c = 1.8\times10^{-10}$ mol/cm^2), "monolayer 2" ($c = 3.5\times10^{-10}$ mol/cm^2), and "solid." The monolayer with $c = 4.4\times10^{-10}$ mol/cm^2 was not chosen for analysis since the vortical interaction results it produced were very similar to those of monolayer 2.

A two-dimensional vertical cross-section passing through the ring axis was investigated exclusively. Because of the flow symmetry, one half of the ring was imaged to increase spatial resolution. The camera, positioned normal to the illuminated measurement plane, recorded a field of view that included the free surface and the 'right-half' of the vortex ring (see figure 5-1). The resulting measurement domain dimensions were 6.14 cm × 4.61 cm. For each interfacial condition, five vortex ring evolutions were recorded and analyzed. This provided for a small base of statistical information. Sufficient time was allowed between each experimental run (approximately 10 minutes, or until the tank was observed quiescent). Continuous image sequences ranging from 2.6 s to 4.0 s were collected in real-time in the

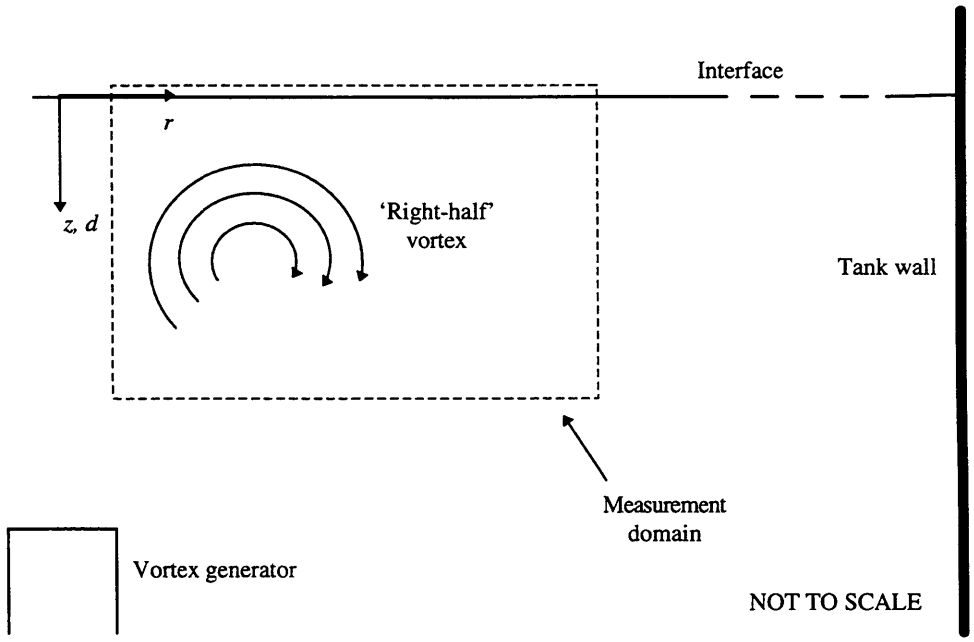

Figure 5-1: Observed measurement plane. The coordinate d measures vertical distance from the interface; r measures radial distance outward from the main axis of the vortex ring. Tank wall effects were nonexistent.

manner outlined in § 4.3.4. The temporal spacing between successive image exposures was 9.3 ms; the duration of each light pulse was 4.6 ms.

Vortex rings were generated as discussed in § 4. The Re_o, based on the piston characteristics, was determined to be 3080. The velocity field induced by the motion of the vortex ring was obtained by processing the image data with the WHOI DPIV code, which was used in the spatial, rather than FFT, mode. Velocity vectors were computed on a regularly spaced grid with a spacing between nodes of 12 pixels. This spacing was determined by estimating the mean particle separation in the DPIV images collected in the present arrangement. This nodal spacing corresponded to a spatial resolution of 1.1 mm. All images were interrogated using 32 $\times$ 32 correlation windows. Since the scale of the main vortex core was near 200 pixels ($\simeq$ 2 cm), attenuation effects due to the low-pass spatial filtering process were less than 10%. The combination of the nodal spacing and window sizing yielded a 62.5% oversampling of the image data. Individual particle displacements ranged from 0–15 pixels; based on these large excursions, the relative error associated with these

measurements is estimated at less than 2%. All successive image pairs in each evolution sequence were processed yielding a temporal resolution of 15 Hz.

In order to nondimensionalize the observed quantities, appropriate scales were chosen. All velocities are scaled by the vertical propagation speed of the vortex ring, U. The mean vertical propagation velocity of the rings was estimated using the DPIV data to be approximately 4.55 cm/s. (This velocity was determined by tracking the progress of the vortex core over time.) All lengths are normalized by the major diameter of the ring (distance between observed vortex cores) before surface interaction, D. Additionally, the dimensionless vorticity and enstrophy are defined as

$$\omega^* \equiv \frac{\omega D}{U},$$

$$\varepsilon^* \equiv \frac{\varepsilon}{U^2}.$$

In all the experimental runs, time was treated in the following manner: $t = 0$ corresponded to the point in time when the vortex ring core passed through the depth $d = 6.4$ cm, or $d/D = 1.6$. At this stage, the ring had propagated $2.1D$ from its inception at the pipe orifice. Saffman [44] suggests that vortex ring roll-up is completed several ring diameters from the generating orifice. Other workers have suggested $3D$ is sufficient. The water depth in the visualization tank was held at a level that allowed for $3.5D$ of propagation before the interface was reached. Visual inspection of the flow indicated that vortex roll-up was complete before surface interaction. The time t is made dimensionless using the chosen length and velocity scales as

$$\tau \equiv \frac{tU}{D}.$$

The ratio U/D is near unity in all cases, therefore both τ and ω^* are approximately equal to the actual magnitudes of their respective dimensional quantities.

5.2 Flow parameters

Based on velocity field estimates of the vortex circulation, Re was computed to be approximately 4200. Circulation was determined by numerically implementing (3.4) for a

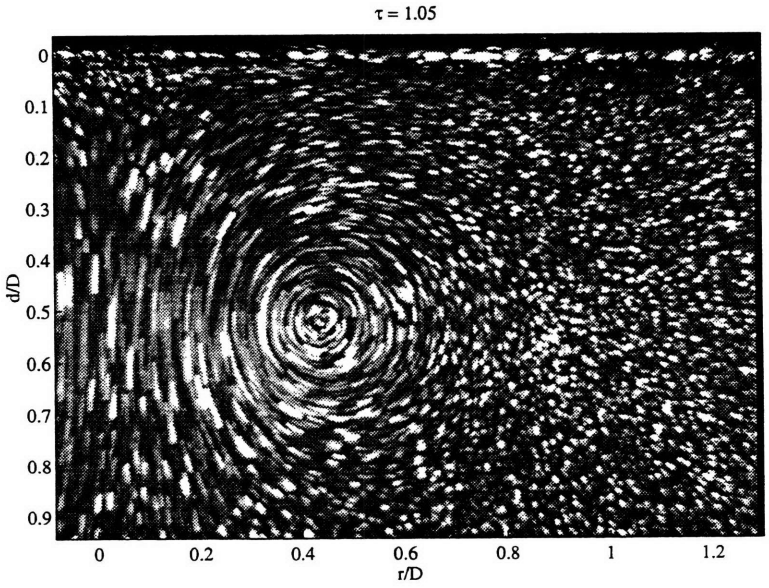

Figure 5-2: Flow visualization of vortex approaching the interface (clean case).

representative collection of vortex cores. With this measure of circulation, $Fr = 0.17$, and $We = 6.1$. At this low Fr, the free-surface deformations are small during vortex interaction.

5.3 Flow visualization

In addition to the five DPIV runs for each interfacial condition, a sixth run was performed for all cases, except the monolayer 1 case, that was used for flow visualization purposes. In order to visualize the flow, the laser was operated in continuous (CW) mode; this resulted in particle streaking that provided excellent imagery of the vortex ring flow. Sample images are given by figures 5-2, 5-3, 5-4, and 5-5. The features observed in these visualizations are discussed in the sections that follow.

5.4 Velocity and vorticity fields

The DPIV results provided spatially intensive velocity information about the vortex surface interaction. Vorticity fields were derived from the velocity data by computing the local

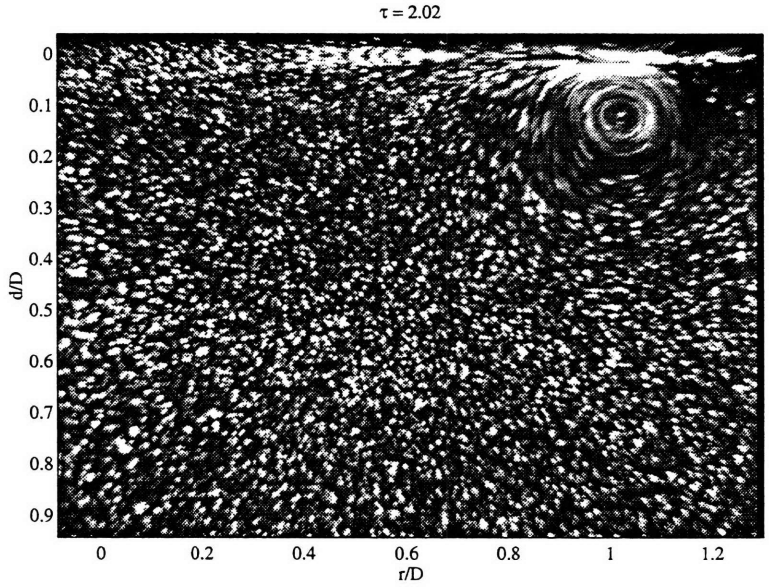

Figure 5-3: Flow visualization of vortex propagating outward just below clean interface.

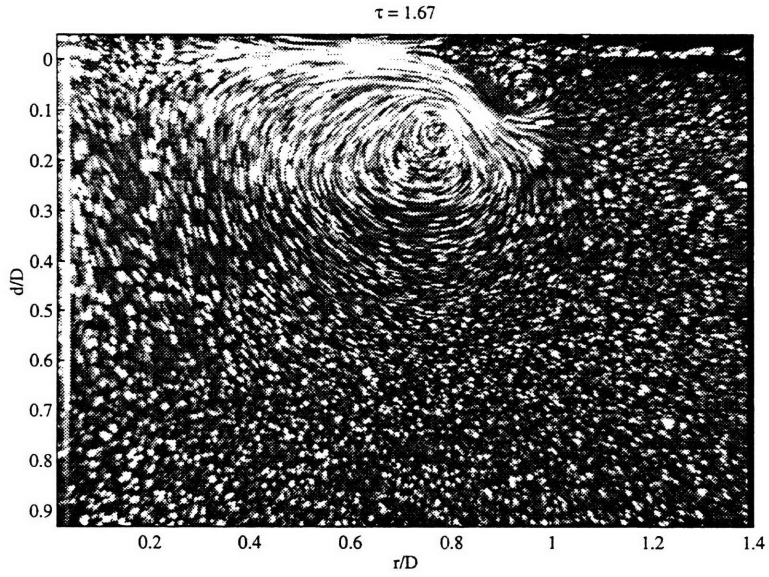

Figure 5-4: Flow visualization of vortex interacting with monolayer 2. A second vortex of opposite spin is seen to develop outboard of the main vortex core.

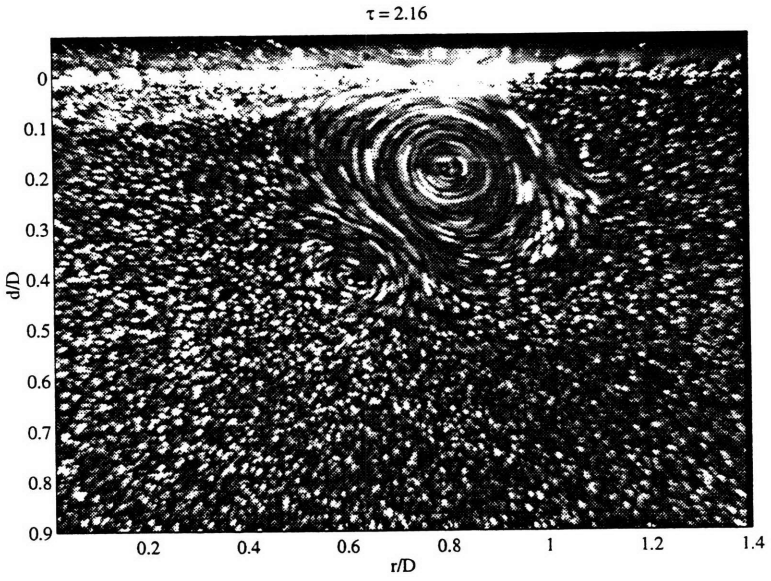

Figure 5-5: Flow visualization of vortex interacting with a solid boundary. Two newly formed vortices are observed.

circulation about each node, rather than differentiating the velocity field directly. As such, the local fluid vorticity at node (i, j) was computed as

$$\omega_{i,j} = \frac{\Gamma_{i,j}}{dA}, \tag{5.1}$$

where $dA = 4\delta r \delta z$ is the enclosed area of the circulation contour. The local circulation at node (i, j) (positive clockwise) is given by

$$\begin{aligned} \Gamma_{i,j} \;=\; & (u_{i-1,j-1} + 2u_{i-1,j} + u_{i-1,j+1})\frac{\delta r}{2} + \\ & (w_{i-1,j+1} + 2w_{i,j+1} + w_{i+1,j+1})\frac{\delta z}{2} - \\ & (u_{i+1,j+1} + 2u_{i+1,j} + u_{i+1,j-1})\frac{\delta r}{2} - \\ & (w_{i+1,j-1} + 2w_{i,j-1} + w_{i-1,j-1})\frac{\delta z}{2}. \end{aligned} \tag{5.2}$$

Figures 5-6, 5-8, 5-10, and 5-12 show velocity fields at three different times for the four interfacial conditions examined. Figures 5-7, 5-9, 5-11, and 5-13 show the corresponding

vorticity fields. The contour levels on the vorticity fields are common for all cases. Each figure represents a single experimental run.

There are several features that are evident in these plots. One is the distinctly different paths followed by the vortex over time. A second feature is the presence of ancillary vorticity that is opposite in sign to that of the primary vortex core. Both of these factors are influenced by the nature of the interface. In an ideal scenario with a free-slip interface and potential flow, a vortex ring nearing the surface will tend to dilate. This can be thought of by constructing an 'image' vortex ring reflected about the interface and approaching from the opposite direction. When a no-slip, or intermediate-slip interface is present, this dilation of the ring major diameter is altered, as is the trajectory subsequent to surface interaction. Our solid boundary represents a no-slip interface, and the two monolayer conditions represent intermediate-slip interfaces. The reason the monolayers constitute intermediate-slip conditions is due to the Marangoni effect. Owing to Marangoni stresses, these interfaces can support a finite surface shear, whereas a perfectly clean surface cannot. These Marangoni stresses arise as a result of the vortex-induced surface velocities which act to redistribute surfactant and compress the monolayer as the ring interacts with the surface. Such compression is resisted by a viscoelastic surface, and a thin near-surface boundary layer can form, which can have strong implications for the bulk flow. Vorticity, opposite in sign to that of the primary vortex cell, can be generated in this near-surface layer. In all the cases studied here, save for the clean case, coherent secondary and tertiary vortex rings were formed as a result of this newly generated vorticity. Figure 5-14 outlines the sign conventions and terminology used in this discussion.

In the clean case, some secondary vorticity, outboard of the primary vortex, is generated near the surface, however, it fails to develop into a coherent vortex. It remains as only a 'patch' and its convected outward by the main vortex. Consequently, the primary vortex proceeds uninhibited beyond the measurement domain until it breaks down into turbulence. This behavior is very similar to what theory would predict for a free-slip interface. We also note the reduced core diameter as the vortex moves outward. This must be the case in order for the total vorticity of the ring to be conserved. When the interface is monolayer 1, we observe a somewhat different behavior. The rate at which the primary vortex propagates

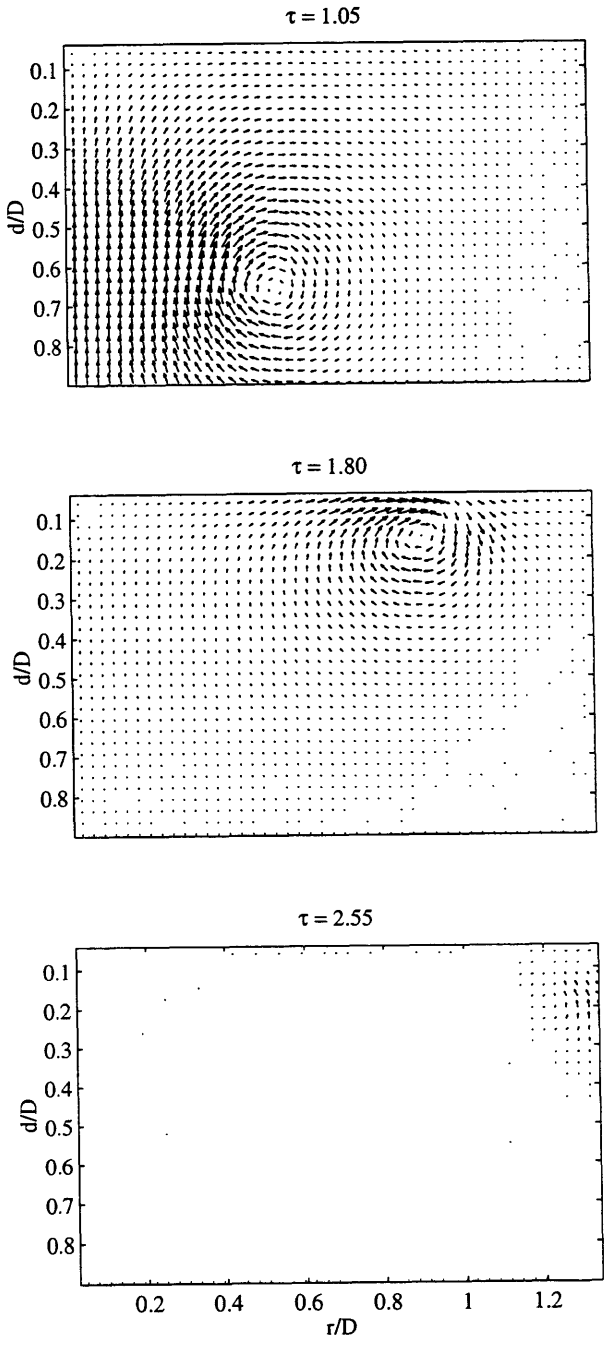

Figure 5-6: Evolution of velocity field for clean interface.

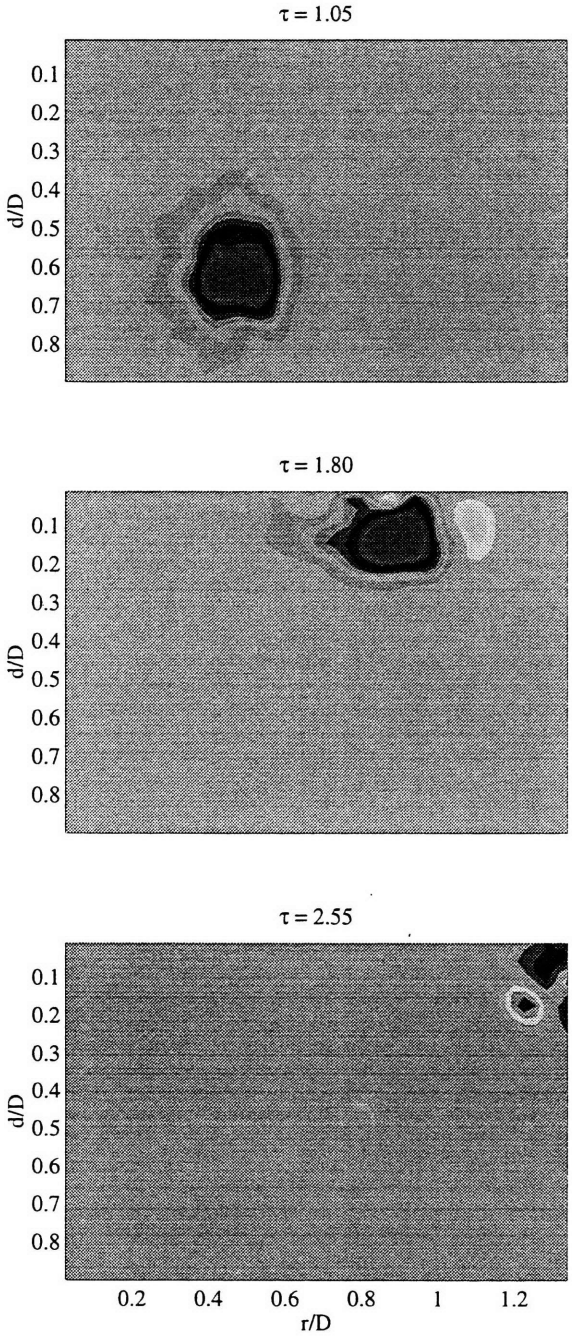

Figure 5-7: Evolution of vorticity field for clean interface. Each panel uses the same contour levels.

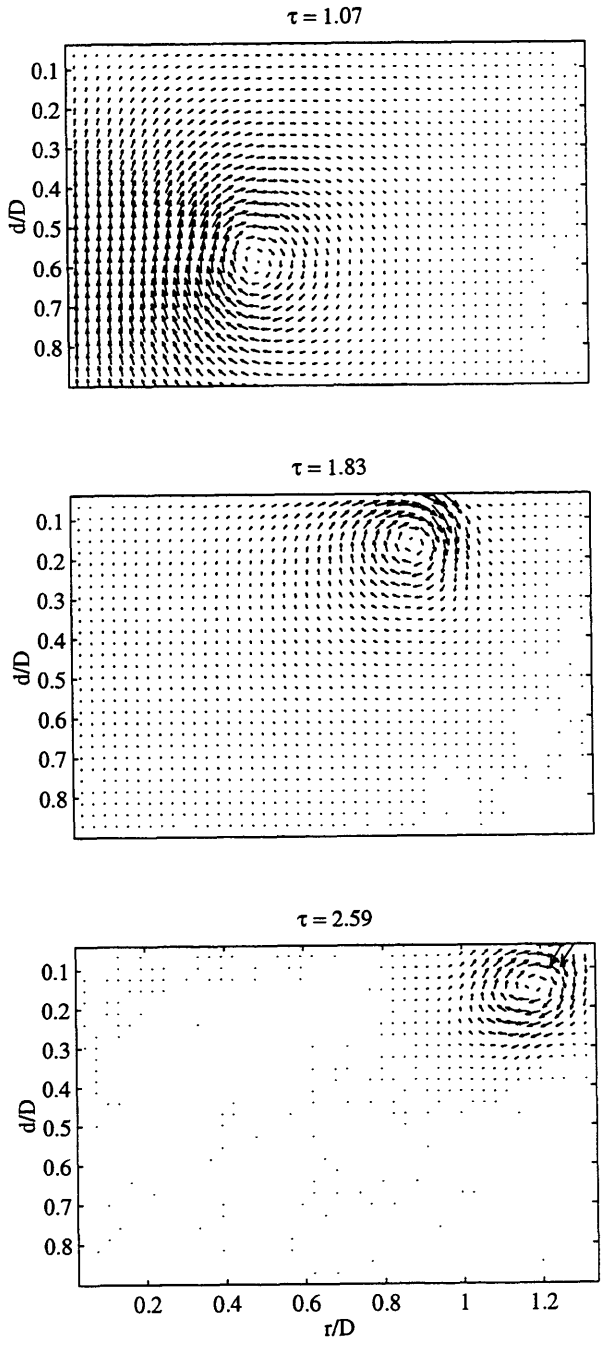

Figure 5-8: Evolution of velocity field for monolayer 1.

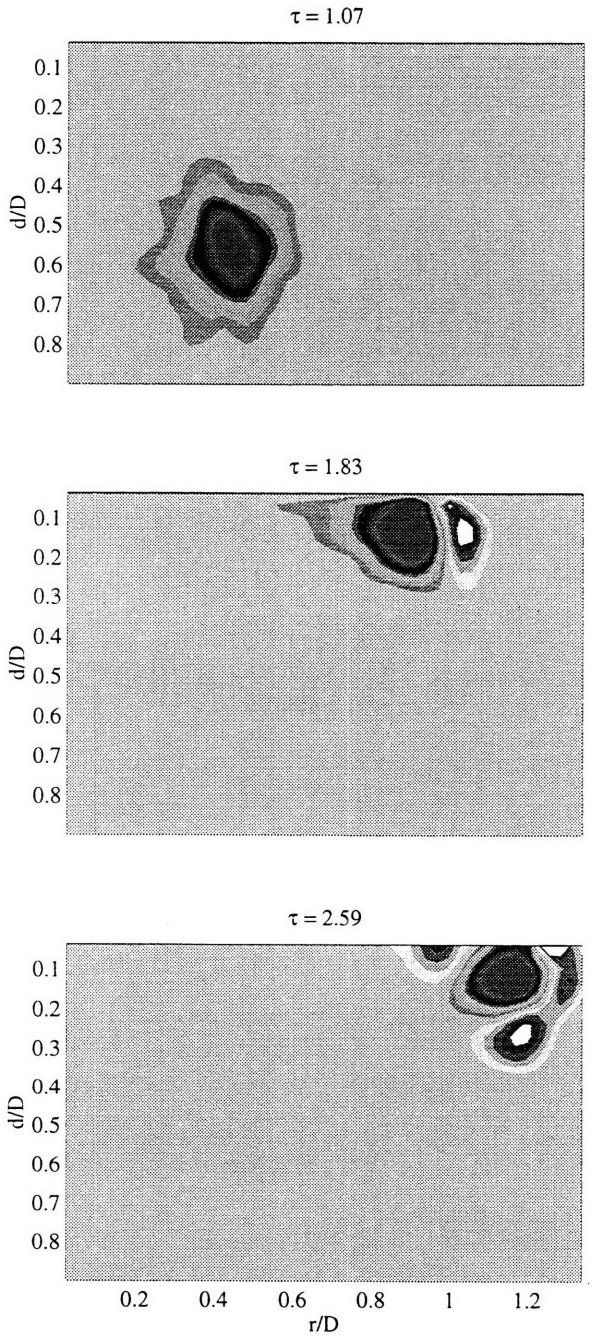

Figure 5-9: Evolution of vorticity field for monolayer 1. Each panel uses the same contour levels.

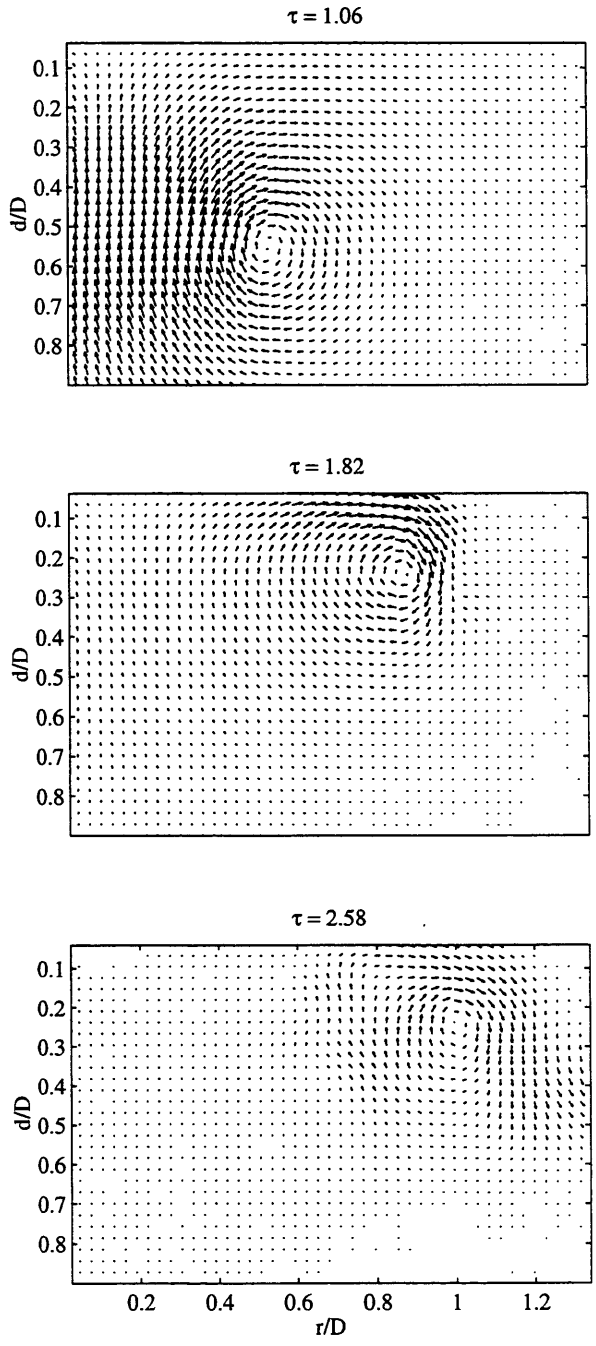

Figure 5-10: Evolution of velocity field for monolayer 2.

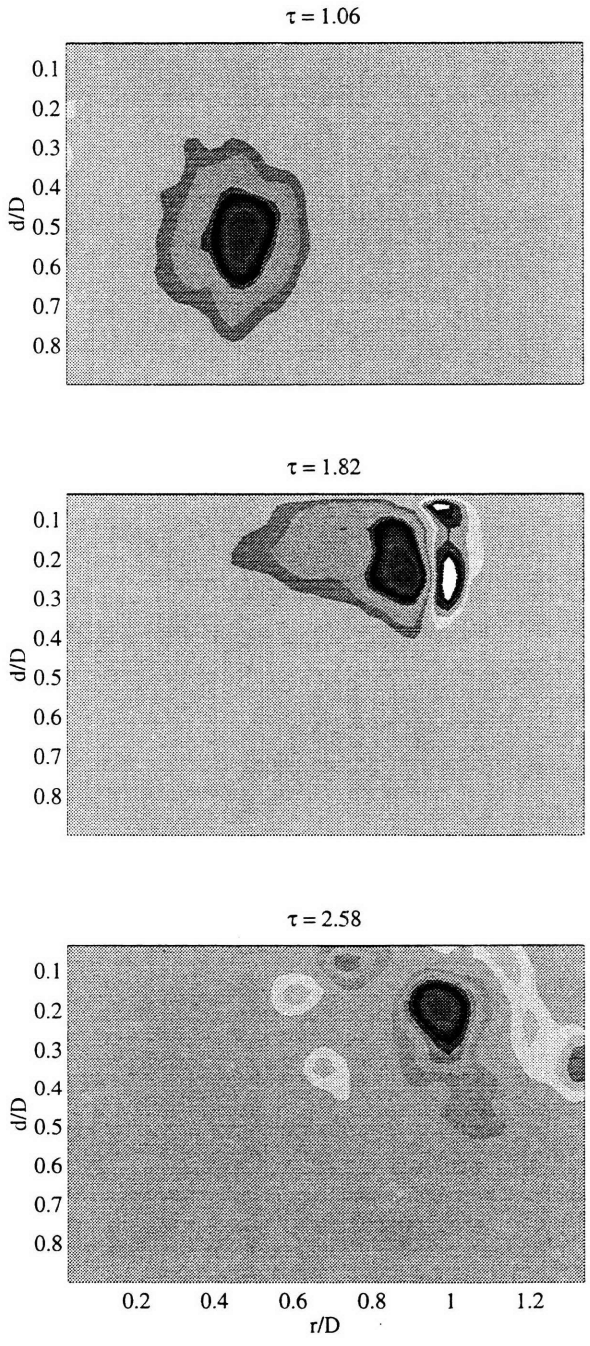

Figure 5-11: Evolution of vorticity field for monolayer 2. Each panel uses the same contour levels.

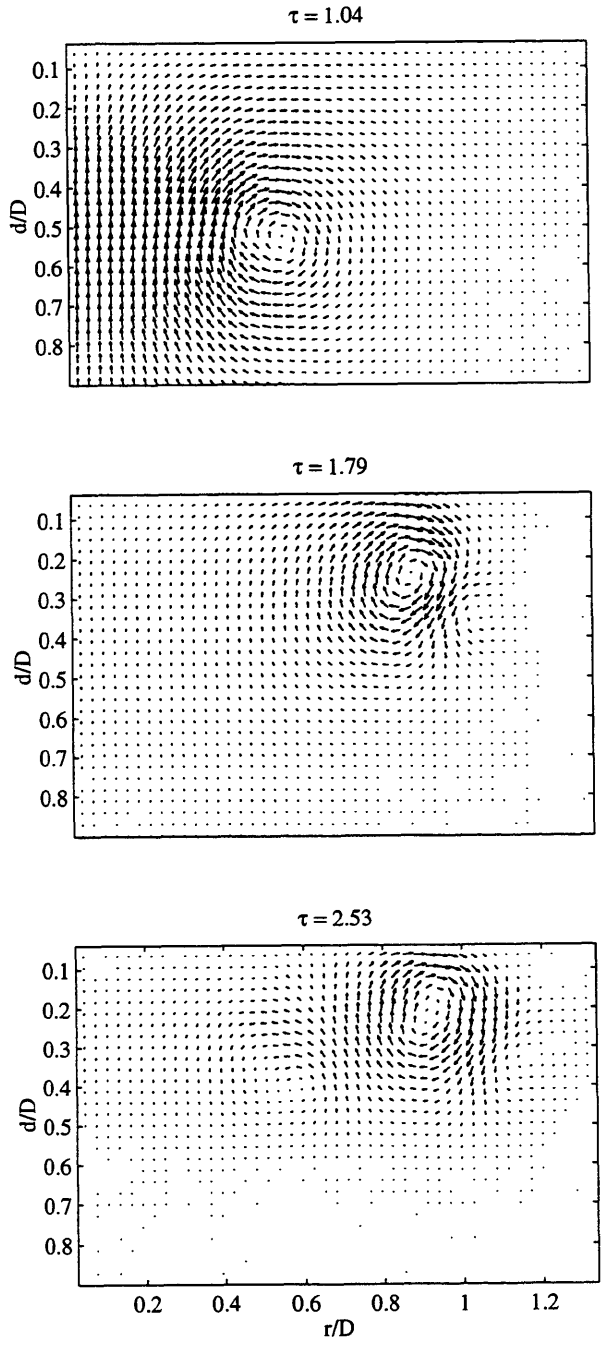

Figure 5-12: Evolution of velocity field for a solid boundary.

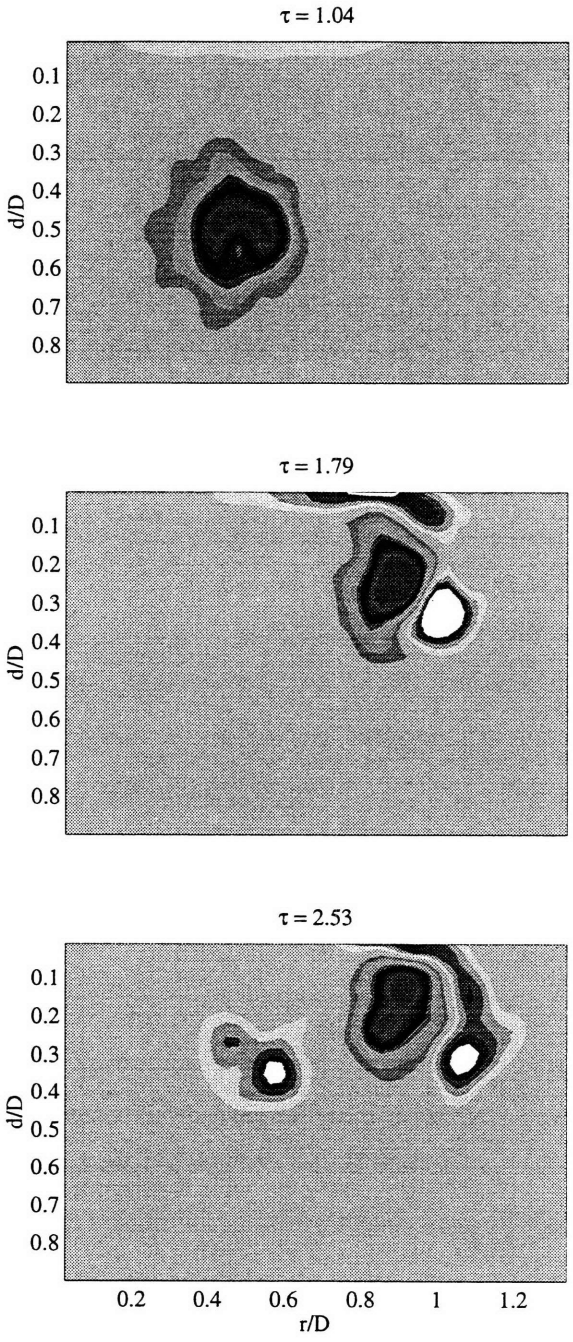

Figure 5-13: Evolution of vorticity field for a solid boundary. Each panel uses the same contour levels.

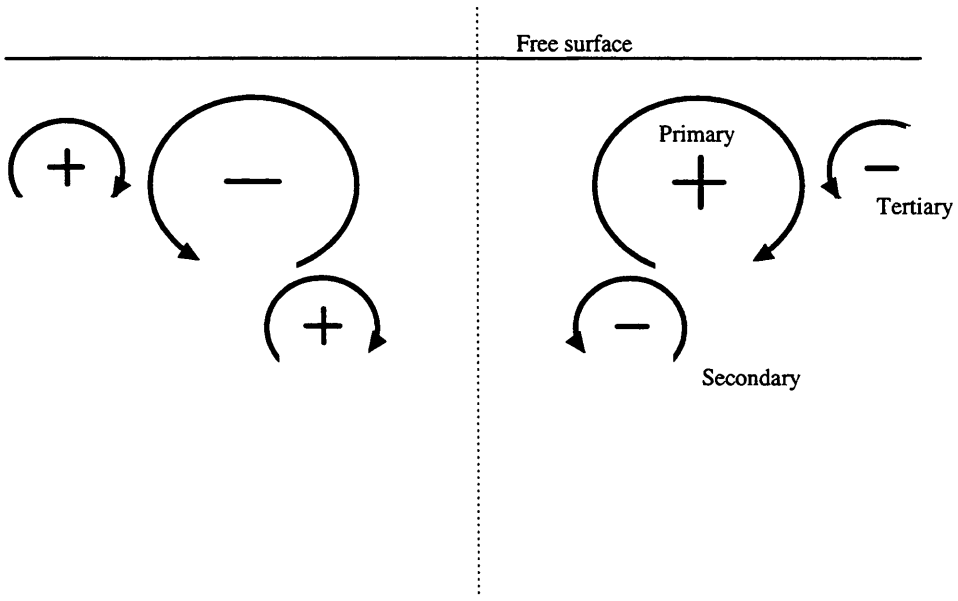

Figure 5-14: Conventions and terminology used for near-surface vorticity/vortices.

outward is retarded as evidenced by its position at $\tau = 2.59$. Additionally, more induced secondary vorticity is formed, which the primary vortex then draws downward. This vorticity begins to wrap around the primary core, preventing further outward motion. The effects of the induced surface vorticity are even more evident in the monolayer 2 case. For that interfacial condition, we observe vortex rebound away from the free surface. Along with this rebound, the outward propagation of the primary vortex core is reduced noticeably. At $\tau = 2.58$, several weaker areas of vortical flow, in addition to the secondary and tertiary flows, are seen to have developed. In the limiting case of a no-slip interface, the interaction of a vortex flow with a solid boundary is the most dramatic of all four conditions. All of the events described above occur on a more intense level. Strong secondary and tertiary vorticity is generated which coalesces into two additional coherent vortical ring structures. Each newly formed ring is whipped violently about the main core and eventually detaches from the primary cell. The secondary vortex then propagates inward until it dissipates. The tertiary core follows a more meandering path where it travels both inward and away from the interface. We show results of the various vortex trajectories in the following section.

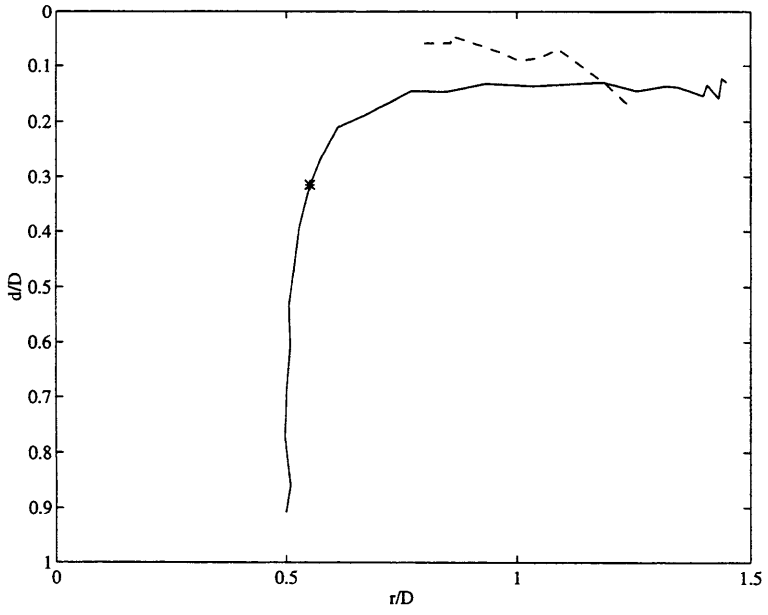

Figure 5-15: Trajectories of primary (—) and secondary (– –) vorticity extrema for clean interface. The * symbol denotes the position of the primary vortex when secondary vorticity is first noticed.

5.5 Vortex trajectories

A striking differences between vortex ring interactions for the various interfacial conditions is the modification (or lack thereof) of the vortex path. To elucidate these differences, we show pathlines of the primary, secondary, and tertiary areas of vorticity. Pathlines were generated by locating and following the points of maximum (positive or negative) vorticity in the three structures over time for each run. Ensemble mean paths were then computed for each interface. Figure 5-15 show the trajectories observed for the clean interface. No measurable tertiary vorticity was detected. The path of the primary vortex is very similar in the clean and monolayer 1 cases. Figure 5-16 shows a unique characteristic of the monolayer 1 case; the two regions of induced vorticity that form orbit the primary vortex as it moves outward. The trajectories for the monolayer 2 case are closely related to the solid boundary interface. In both instances, the primary vortex rebounds significantly, while the secondary and tertiary cells are jettisoned off, away from the interface. Once rebounding is complete, the two cases diverge. In the solid boundary interaction, the primary vortex stagnates,

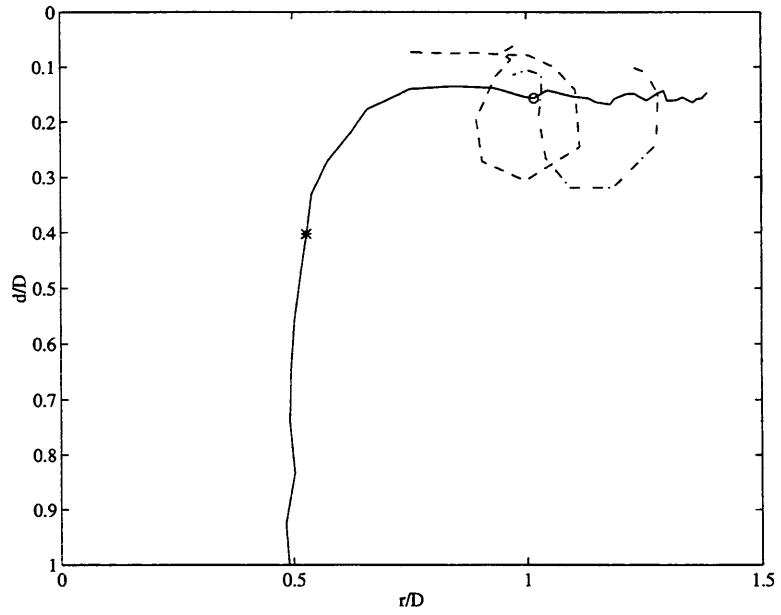

Figure 5-16: Trajectories of primary (—) , secondary (– –), and tertiary (– · –) vorticity extrema for monolayer 1. The $*$ and $\circ$ symbols denote the positions of the primary vortex when secondary and tertiary vorticity, respectively, is first noticed.

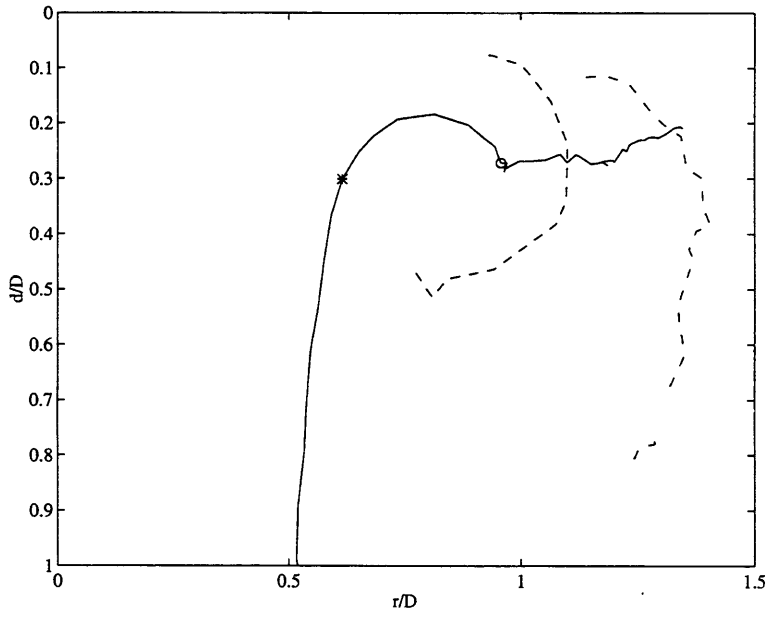

Figure 5-17: Trajectories of primary (—), secondary (– –), and tertiary (– · –) vorticity extrema for monolayer 2. The $*$ and $\circ$ symbols denote the positions of the primary vortex when secondary and tertiary vorticity, respectively, is first noticed.

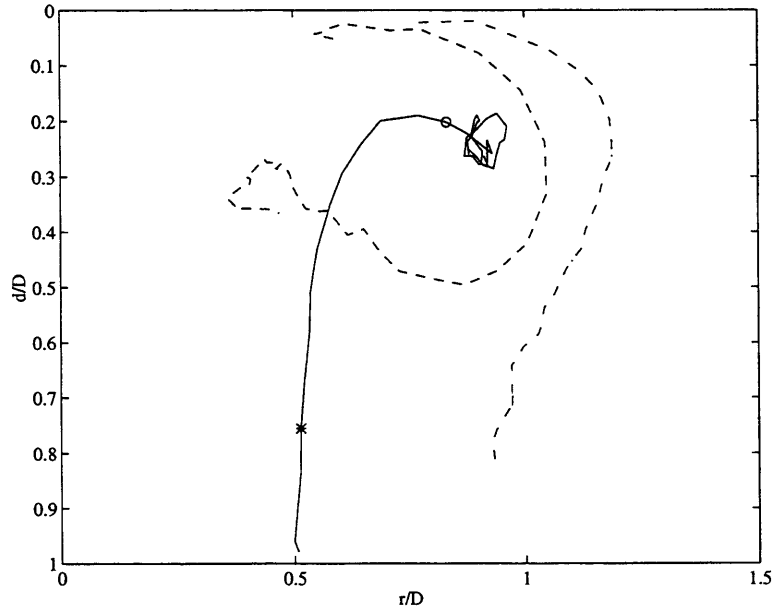

Figure 5-18: Trajectories of primary (—), secondary (– –), and tertiary (– · –) vorticity extrema for a solid boundary. The * and o symbols denote the positions of the primary vortex when secondary and tertiary vorticity, respectively, is first noticed.

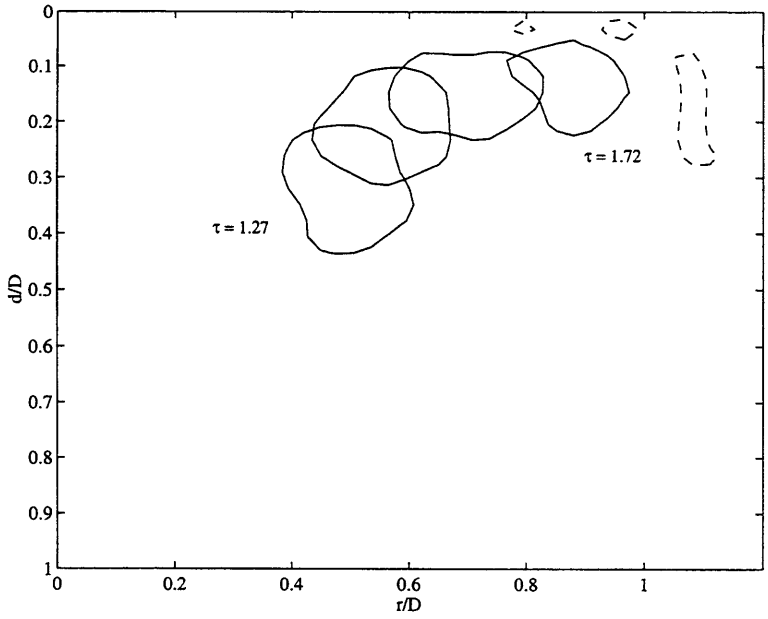

Figure 5-19: Contours of equivorticity for clean interface. The solid line contours correspond to $\omega^* = +20$. The broken contours correspond to $\omega^* = -8$. Temporal spacing between contours, $\Delta\tau = 0.15$.

and spins down until it completely decays to incoherent motion. During the monolayer 2 interaction following rebound, the primary vortex arcs back up toward the surface and resumes its outward propagation at a much reduced rate. A final interesting feature that is shown by these plots is the time of onset of secondary vorticity. Most remarkable is the early indication of induced vorticity at the solid boundary interface. This is attributable to the condition of zero velocity at the interface, which causes a near-surface shear layer to develop, which is observed as vorticity.

Both trajectory modification and induced surface vorticity can be illustrated further by tracking equivorticity contours (lines of constant vorticity) during the interaction process. This is done in figures 5-19, 5-20, and 5-21 for single representative runs of the clean, monolayer 2, and solid cases respectively. Immediately evident in the clean case is the reduction in core size as the vortex expands radially outward. The weak patch of secondary vorticity is also apparent. The vorticity contours for the monolayer interaction illustrate the rebound effect as well as the wrapping of the induced vorticity around the main vortex

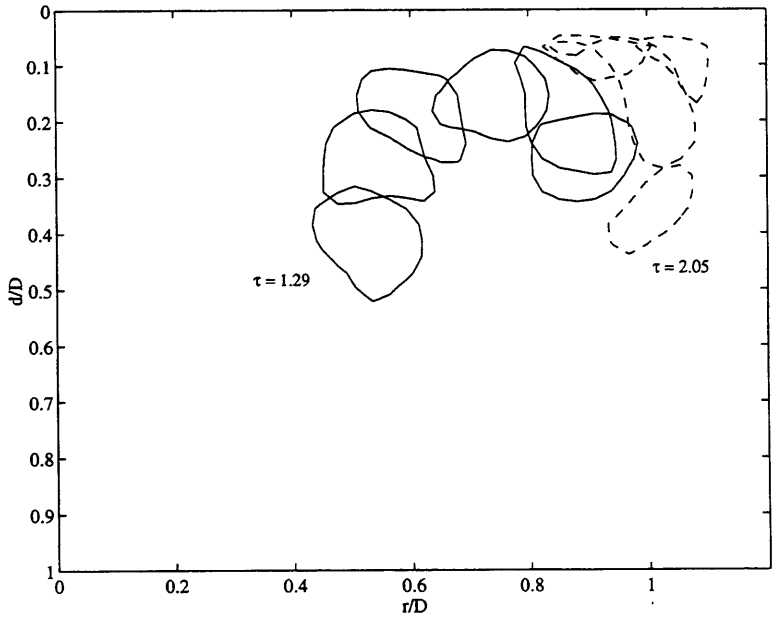

Figure 5-20: Contours of equivorticity for monolayer 2. The solid line contours correspond to $\omega^* = +20$. The broken contours correspond to $\omega^* = -8$. Temporal spacing between contours, $\Delta\tau = 0.15$.

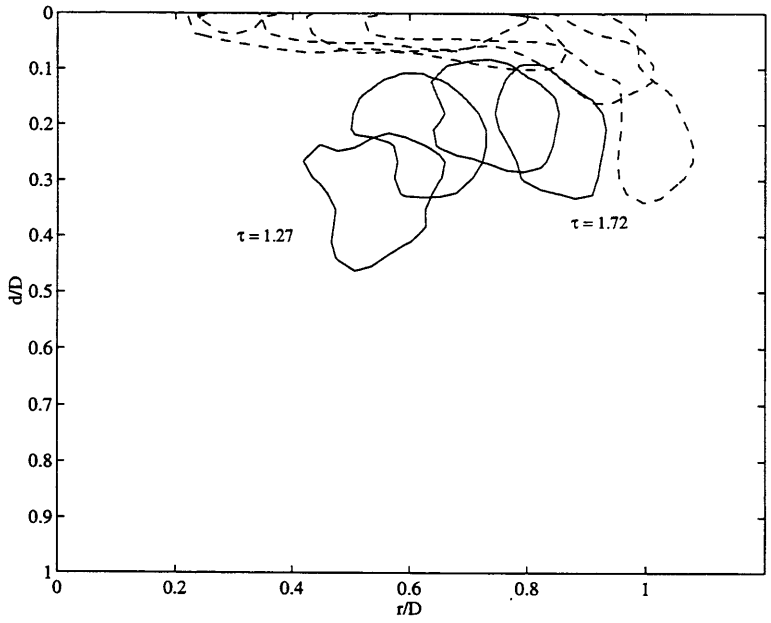

Figure 5-21: Contours of equivorticity for a solid boundary. The solid line contours correspond to $\omega^* = +20$. The broken contours correspond to $\omega^* = -8$. Temporal spacing between contours, $\Delta\tau = 0.15$.

core. In the solid boundary interaction, the secondary vorticity appears as a thin band initially at the interface that is then drawn down into the bulk. The distortion of the primary vortex core shape is also visible. We note that these experimental results compare well with the numerical study of Tsai and Yue [52]. Although their simulations stop short of full secondary vortex roll-up, they do predict accurately the laminar events leading up to such development.

5.6 Near-surface velocities

As the vortex ring advances toward each surface, its circulatory motion begins to accelerate the fluid at the surface radially outward, except in the case of the solid boundary where all motion vanishes at the interface. The effects of the intermediate-slip and no-slip conditions can be seen by examining the near-surface radial component of velocity for the different conditions. Figures 5-22, 5-23, and 5-24 show the spatial variation of the near-surface radial velocity component at several instances in time for the clean, monolayer 2, and solid cases. Each curve is the ensemble mean of all runs for each case. The velocities at the interfaces were unable to be determined due to the limitations of the DPIV technique. Nevertheless, these results are in excellent qualitative agreement with the numerical predictions of Tsai and Yue [52]. In all three cases, the outward propagation of the primary vortex is indicated by the progressive shift in the velocity peak over time. The salient feature of these curves is the effective vanishing of radial velocity at sufficient r/D for the monolayer and solid interfaces. The velocity is driven to near zero by the induced Marangoni forces that act to oppose the surface dilation due to the vortex ring.

5.7 Temporal evolution of vorticity

In order to gain insight into the relative strengths of the primary, secondary, and tertiary vorticity, the values of extremum vorticity in each region were tracked over time. These results comprise figures 5-25, 5-26, 5-27, and 5-28. All curves represent the ensemble mean for each interface. Before discussing these results, we point out certain critical stages during the evolution: at $\tau = 0.7$, the core of the primary ring vortex has entered the measurement

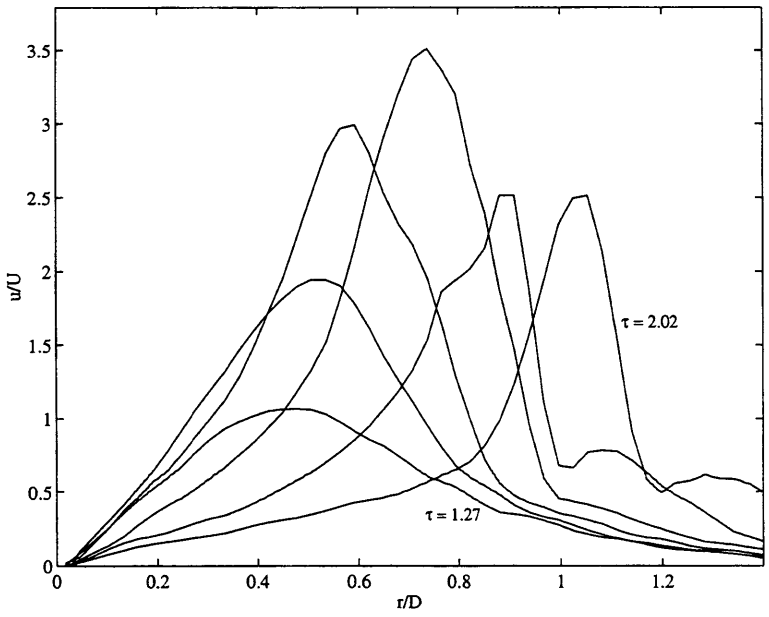

Figure 5-22: Variation of near-surface radial component of velocity for clean interface. Velocities are taken along a horizontal section at a depth, $d/D = 0.03$ (0.125 cm). $\Delta\tau = 0.15$

domain; near $\tau = 1.1$, the primary vortex is at mid-depth in the domain; near $\tau = 1.4$, the main vortex is at the surface; at $\tau = 2.1$ for the clean case, significant motion associated with the vortex has begun to exit the measurement domain; and beyond $\tau = 2.6$ for the clean case, virtually all vortex motion has left the field of view.

Examining the evolution of vorticity for the clean case we see that the induced vorticity is weak relative to that of the primary core vortex; during its short-lived presence, the secondary vorticity is, at peak, 20% that of the primary. The vorticity associated with the primary circulation appears to vary over the duration of the interaction. After passing through a local maximum at mid-depth in the domain, the vorticity levels off as it nears the surface. Near $\tau = 1.4$, the vorticity intensifies somewhat for a brief period and then falls off sharply. This is most likely due to the vortical motion escaping the measurement domain. The cause of the peak near $\tau = 2.3$ is not clear. Similar trends for the primary vortex are apparent in the monolayer 1 case. The initial peak in primary vorticity is realized, as is the levelling off period. At approximately the time when surface effects begin to be

influential ($\tau \simeq 1.3$), the primary vorticity begins to steadily increase. This also appears to correlate with the onset of secondary vorticity. All three regions of vorticity pass through their maxima at nearly the same time ($\tau \simeq 2.1$), after which each decays toward zero. The primary vorticity peak for monolayer 1 condition is the largest of all cases. The behavior of the two ancillary vortices is quite similar in terms of their vorticity evolution; both regions are of equal strength and duration. Additional similarity is noticed in their orbital paths around the main vortex (see figure 5-16). We note that in this case, the induced vorticity is roughly 1/3 that of the primary. A similar result was also observed experimentally by Hirsa and Willmarth [31], where they note a 1/3 relationship between the primary circulation and that of the secondary vortices.

Monolayer 2 exhibits a like evolution. Although the overall primary vorticity is slightly weaker, the secondary vortex is more intense (approximately 50% of the primary). The tertiary intensity is about half that of the secondary, which is quite different from the monolayer 1 interface. Also, the decay rates of all three vortical regions is lessened when compared to the previous two cases. In the final case, which corresponds to the solid boundary, the presence of ancillary vortical features is most dramatic. At its peak, the secondary vorticity is more than 1/2 that of the primary. Both it and the tertiary vortex persist for longer time as well. The correlation between primary vorticity and the onset of secondary vorticity that was observed for monolayer 1 can also be detected for the latter two interfacial conditions. We also note that the significant decay of primary vorticity begins at or near the point where tertiary vorticity is generated.

The total vortical energy associated with these interactions can be estimated by computing the fluid enstrophy as defined by (3.6). The mean temporal evolutions of enstrophy for all four cases studied are shown in figure 5-29. As might be expected, the solid interface generates the greatest amount of fluid enstrophy, which also persists for the longest amount of time. The peak in the solid case enstrophy (at $\tau \simeq 1.5$) is attributed to the primary and secondary vorticity only; tertiary vorticity is not present at this stage. In terms of enstrophy, the clean and monolayer 1 cases behave almost identically through $\tau = 1.6$. At that point, the clean case falls off drastically while the monolayer persists some time longer. Again, this is most likely due to fluid motion leaving the field of view and should not be

considered solely vortex decay. Somewhat intriguing is the small resurgence in energy for both the clean and monolayer 1 interfaces as they decay: near $\tau = 2.25$ for the clean case, and near $\tau = 2.5$ for the monolayer. The behavior of monolayer 2 appears counterintuitive. It does not seem to act intermediate between the monolayer 1 and solid cases. Instead it exhibits the least amount of rotational energy for a large portion of the interaction, excluding the clean surface which drops off for the reason mentioned above. The degree to which the primary and induced vortical features interact in a constructive, or destructive, manner may explain this, but such an explanation is purely speculative. One might also attempt to explain this anomaly by considering the wave damping results of § 2. In the case of capillary–gravity waves, the impact of a surface film is most prominent at an intermediate surfactant concentration. A similar phenomenon may be present in the near-surface vortex interaction events. This reasoning is also highly speculative and would necessitate further scientific inquiry.

5.8 Summary

This chapter has presented the experimental results of near-surface vortical interactions for several different interfacial conditions. Clean, monolayer, and solid interfaces were studied in these laboratory experiments. The DPIV technique has been used effectively to quantify the observed velocity fields in a two-dimensional plane of a vortex flow. These results have been used to qualitatively describe the flow characteristics associated with each interfacial condition. Additionally, quantitative estimates of the temporal evolution of vorticity and enstrophy were obtained.

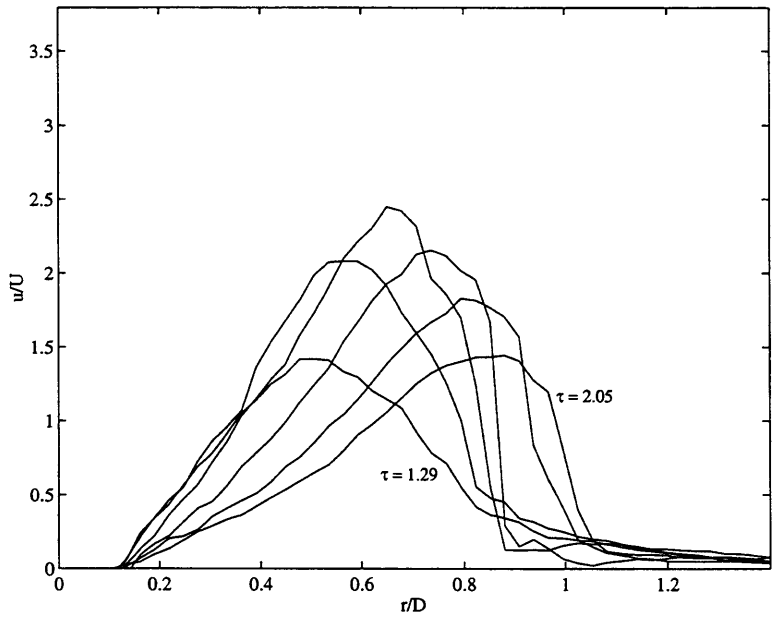

Figure 5-23: Variation of near-surface radial component of velocity for monolayer 2. Velocities are taken along a horizontal section at a depth, $d/D = 0.03$ (0.125 cm). $\Delta\tau = 0.15$

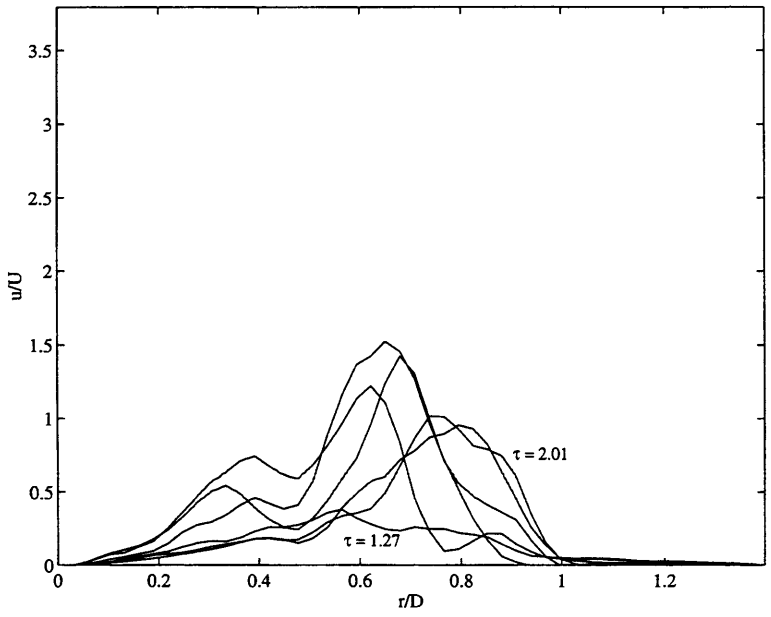

Figure 5-24: Variation of near-surface radial component of velocity for a solid boundary. Velocities are taken along a horizontal section at a depth, $d/D = 0.04$ (0.154 cm). $\Delta\tau = 0.15$

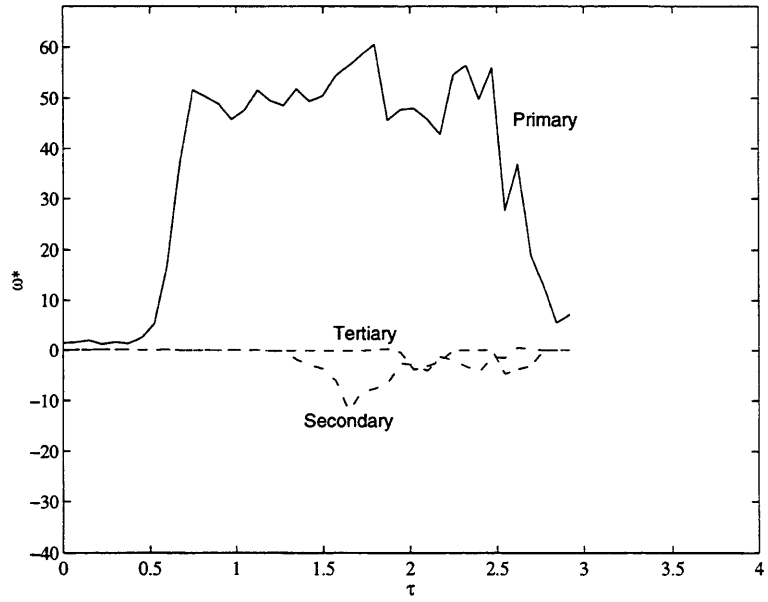

Figure 5-25: Temporal evolution of primary, secondary, and tertiary vorticity extrema for clean interface.

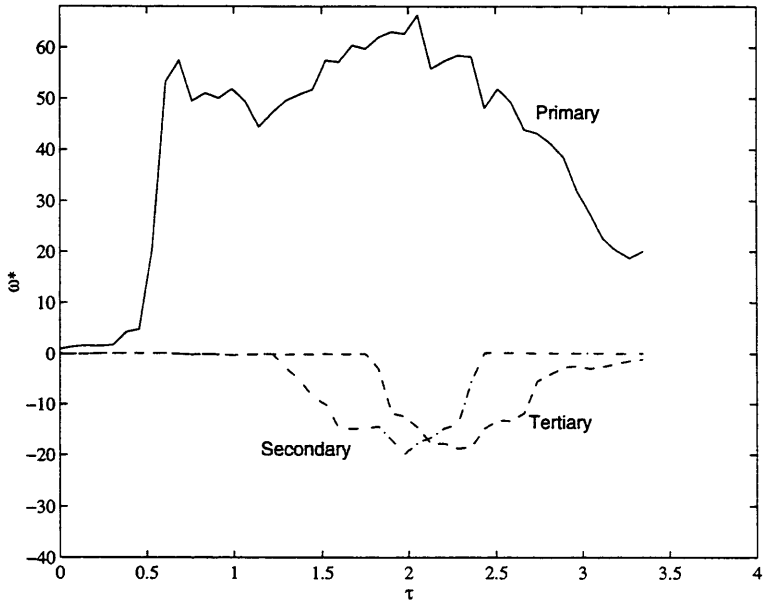

Figure 5-26: Temporal evolution of primary, secondary, and tertiary vorticity extrema for monolayer 1.

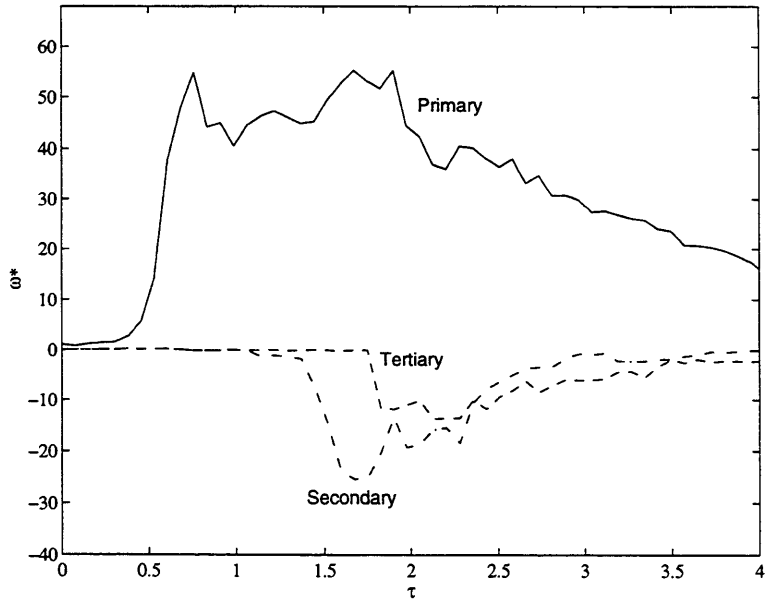

Figure 5-27: Temporal evolution of primary, secondary, and tertiary vorticity extrema for monolayer 2.

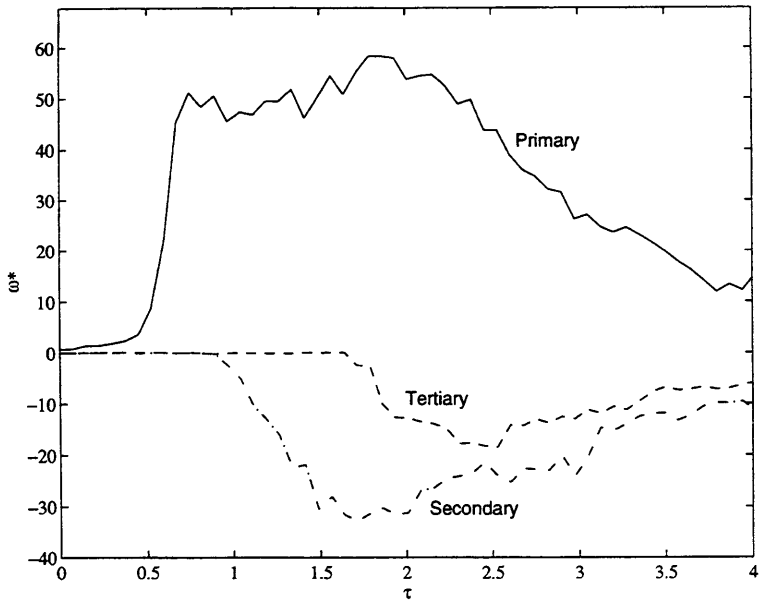

Figure 5-28: Temporal evolution of primary, secondary, and tertiary vorticity extrema for solid boundary.

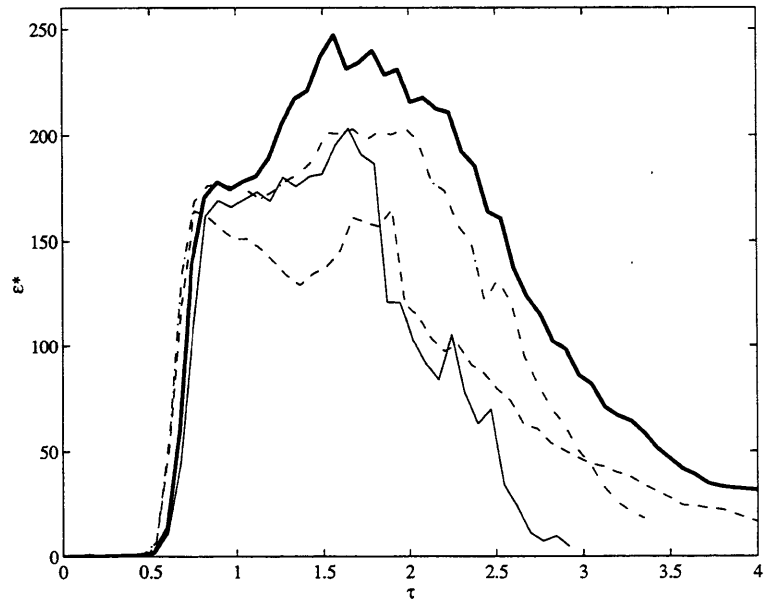

Figure 5-29: Temporal evolution of enstrophy for clean (thin —), monolayer 1 (– · –), monolayer 2 (– –), and solid (thick —) interfaces.

Chapter 6

Concluding remarks

6.1 Summary

In this thesis, we have explored the effects of surface films on two canonical near-surface flows: capillary–gravity waves and vortex impingement on a free surface. An understanding of the influence of surface films on these interfacial flows in important to several different air–sea interaction processes. The fact that a surface film, whether in the laboratory or in the ocean environment, exhibits a finite viscoelasticity is fundamental to explaining the resulting hydrodynamic behavior of both short waves and vortex flow near an interface.

Our discussion of capillary–gravity waves led to the derivation of a complete two-phase dispersion relation that governs the propagation of small scale waves at the interface of two viscous media having an interfacial dilational elastic modulus. Upon probing this relation, the enhanced wave damping due to a viscoelastic surface was shown. It was also shown theoretically that the maximum in this damping occurs at an intermediate value of the elastic modulus. Experimental results collected as part of this work supported these analytic predictions, and also provided *in vitro* measurements of the characteristics of the various surfaces investigated during the complimentary vortex ring laboratory experiments.

Studies of the interactions between a vortical flow and interfaces with varying degrees of surface viscoelasticity illustrated, both qualitatively and quantitatively, the dramatic effect a small amount of surface contamination can have on the bulk flow properties. These effects were observed in vortex trajectory modification and production of near-surface vorticity,

which in all but the cleanest surface condition, formed secondary and tertiary coherent vortex structures. This induced vorticity was shown to influence the flow of the primary vortex significantly as the interfacial more closely resembled a no-slip boundary.

6.2 Discussion

A direct connection between the dynamical behavior of capillary–gravity waves and near-surface vortex interaction is not clear at this point. What is evident is the generation of a more dissipative flow regime under interfacial viscoelastic conditions. This is reflected by the enhanced damping in the case of capillary–gravity waves, and in the increased near-surface vorticity production in the case of vortex flow. A relationship between these two observed phenomena may exist, however, further study is required to determine if such a correlation is present. We do point out an intriguing similarity that was revealed in the studies of the two flows: in both the small scale waves and in the vortex flow, the enhancement in the two primary measured quantities, wave damping and fluid vorticity, indicated a critical maximum at an intermediate surface condition. It may therefore be possible to relate these two flows in terms of these enhancement quantities.

Other possible aspects of this problem, such as Reynolds number dependence, or the effects of soluble surfactants could be investigated by extending the concepts and methods outlined in this thesis in a straightforward manner. An element of this work that could be improved involves the complex wavenumber measurements. Examining the dispersion relation, it was found that for a viscoelastic surface, the accuracy and precision of the experimentally determined values for the wavenumber and decay parameter need be on the order of 1 in 1000 to correctly estimate an elastic modulus. However, the ultimate utility of such an estimate is questionable since measurements of viscoelasticity are not made in the field. The wave decay (or enhanced wave decay) may be a more useful measurement.

References

[1] N. K. Adam. *The Physics and Chemistry of Surfaces.* Oxford University Press, New York, NY, 1930.

[2] R. J. Adrian. Multi-point optical measurements of simultaneous vectors in unsteady flow—a review. *Int. J. Heat Fluid Flow*, 7:127–145, 1986.

[3] J. Aitken. On the effect of oil on a stormy sea. *Proc. Roy. Soc. Edinb.*, 12:56–75, 1883.

[4] J. M. Anderson. *Vorticity control for efficient propulsion.* PhD dissertation, Massachusetts Institute of Technology, Cambridge, MA, 1996.

[5] S. J. Barker and S. C. Crow. The motion of two-dimensional vortex pairs in a ground effect. *J. Fluid Mech.*, 89:659–671, 1977.

[6] G. K. Batchelor. *An Introduction to Fluid Dynamics.* Cambridge University Press, New York, NY, 1967.

[7] L. P. Bernal, A. Hirsa, J. T. Kwon, and W. W. Willmarth. On the interaction of vortex rings and pairs with a free surface for varying amounts of surface active agent. *Phys. Fluids A1*, 12:2001–2004, 1989.

[8] E. J. Bock. On ripple dynamics IV. Linear propagation of plane-wave packets: Observation. *J. Colloid Interface Sci.*, 131:38–46, 1989.

[9] E. J. Bock. On ripple dynamics V. Linear propagation of cylindrical waves on liquids with and without a surface dilational viscoelastic response. *J. Colloid Interface Sci.*, 147:422–432, 1991.

[10] E. J. Bock and N. M. Frew. Static and dynamic response of natural multicomponent oceanic surface films to compression and dilation: laboratory and field observations. *J. Geophys. Res.*, 98:14599–14617, 1993.

[11] E. J. Bock and J. A. Mann. On ripple dynamics II. A corrected dispersion relation for surface waves in the presence of surface elasticity. *J. Colloid Interface Sci.*, 129:501–505, 1989.

[12] R. Cini and P. P. Lombardini. Experimental evidence of a maximum in the frequency domain of the ratio of ripple attenuation in monolayered water to that in pure water. *J. Colloid Interface Sci.*, 81:125–131, 1981.

[13] R. Cini, P. P. Lombardini, and H. Hühnerfuss. Remote sensing of marine slicks using their influence on wave spectra. *Intl. J. Remote Sensing*, 4:101–110, 1983.

[14] E. A. Cowen and S. G. Monismith. A hybrid digital particle tracking velocimetry technique. Submitted, 1996.

[15] J. T. Davies and E. K. Rideal. *Interfacial Phenomena.* Academic Press, New York, NY, 1963.

[16] M. D. DeGrandpre, W. R. McGillis, N. M. Frew, and E. J. Bock. Laboratory measurements of seawater CO_2 gas fluxes. In B. Jähne and E. Monahan, editors, *Air-Water Gas Transfer*, pages 375–383. AEON Verlag, 1995.

[17] R. Dorrestein. General linearized theory of the effect of surface films on water ripples. *Proc. K. Ned. Akad. Wet. Ser. B*, 54:260–272, 350–356, 1951.

[18] J. C. Earnshaw and A. C. McLaughlin. Waves at liquid interfaces: coupled oscillators and mode mixing. *Proc. R. Soc. Lond. A*, 433:663–678, 1991.

[19] D. A. Edwards, H. Brenner, and D. T. Wasan. *Interfacial Transport Processes and Rheology.* Butterworth-Heinemann, Boston, MA, 1991.

[20] B. Franklin. Of the stilling of waves by means of oil. *Philos. Trans. Roy. Soc. London*, 64:445–460, 1774.

[21] N. M. Frew. The role of organic films in air–sea gas exchange. In P. S. Liss and R. A. Duce, editors, *The Sea Surface and Global Change*, pages 121–172. Cambridge University Press, New York, NY, 1997.

[22] N. M. Frew, E. J. Bock, W. R. McGillis, A. V. Karachintsev, T. Hara, T. Münsterer, and B. Jähne. Variation of air-water gas transfer velocity with wind stress and surface viscoelasticity. In B. Jähne and E. Monahan, editors, *Air-Water Gas Transfer*, pages 529–541. AEON Verlag, 1995.

[23] N. M. Frew, J. C. Goldman, M. R. Dennett, and A. S. Johnson. Impact of phytoplankton-generated surfactants on air-sea gas exchange. *J. Geophys. Res.*, 95:3337–3352, 1990.

[24] M. Gharib and A. Weigand. Experimental studies of vortex disconnection and connection at a free surface. *J. Fluid Mech.*, 321:59–86, 1996.

[25] C. H. Giles. Franklin's teaspoonful of oil. *Chem. Ind.*, 1:1616–1624, 1969.

[26] A. Glezer and D. Coles. An experimental study of a turbulent vortex ring. *J. Fluid Mech.*, 211:243–283, 1990.

[27] R. C. Gonzalez and P. Wintz. *Digital Image Processing.* Addison-Wesley, Reading, MA, 1987.

[28] F. C. Goodrich. On the damping of water waves by monomolecular films. *J. Phys. Chem.*, 66:1858–381, 1962.

[29] T. Hara. Personal communication.

[30] A. Hirsa, G. M. Korenowski, L. M. Logory, S. Kim, and C. D. Judd. Surfactant effects on vortex flows at a free surface and the relation to interfacial gas transfer. In B. Jähne and E. Monahan, editors, *Air-Water Gas Transfer*, pages 649–663. AEON Verlag, 1995.

[31] A. Hirsa and W. W. Willmarth. Measurement of vortex pair interaction with a clean or contaminated free surface. *J. Fluid Mech.*, 259:24–45, 1994.

[32] H. Lamb. *Hydrodynamics.* Dover Publishing, New York, NY, 1945.

[33] V. G. Levich. *Physicochemical Hydrodynamics.* Prentice-Hall, Inc., Englewood Cliffs, NJ, 1962.

[34] J. Lucassen. Longitudinal capillary waves. *Trans. Faraday Soc.*, 64:2221–2235, 1967.

[35] J. Lucassen and R. S. Hansen. Damping of waves on monolayer-covered surfaces. *J. Colloid Interface Sci.*, 22:32–44, 1966.

[36] E. H. Lucassen-Reynders and J. Lucassen. Properties of capillary waves. *Advan. Colloid Interface Sci.*, 2:347–395, 1969.

[37] J. T. Mass. Dynamic properties of seawater surfactants. Master's thesis, Massachusetts Institute of Technology, Cambridge, MA, 1995.

[38] T. Maxworthy. Some experimental studies of vortex rings. *J. Fluid Mech.*, 81:465–495, 1977.

[39] S. P. McKenna, W. R. McGillis, and E. J. Bock. The influence of surface films on near-surface vortical flows. *Colloids Surfaces A: Physicochem. Eng. Aspects*, 118:263–272, 1996.

[40] S. Ohring and H. J. Lugt. Interaction of a viscous vortex pair with a free surface. *J. Fluid Mech.*, 227:47–70, 1991.

[41] Plutarch. *Moralia*, volume 11. Harvard University Press, Cambridge, MA, 1949. Translation by F. H. Sandbach. Original text dates back to c. 100 A.D.

[42] A. Pockels. Surface tension. *Nature*, 43:437–439, 1891. This text appears as a letter to Lord Rayleigh.

[43] R. H. Sabersky, A. J. Acosta, and E. G. Hauptmann. *Fluid Flow: A First Course in Fluid Mechanics.* Macmillan Publishing Company, New York, NY, 1989.

[44] P. G. Saffman. On the formation of vortex rings. *Stud. Appl. Maths*, 54:261–268, 1975.

[45] T. Sarpkaya and D. O. Henderson. Free surface scars and striations due to trailing vortices generated by a submerged lifting surface. Technical Report 85-0445, AIAA, 1985.

[46] J. C. Scott. Flow beneath a stagnant film on water: the reynolds ridge. *J. Fluid Mech.*, 116:283–296, 1982.

[47] C. P. Secundus. *Natural History*, volume 1. Harvard University Press, Cambridge, MA, 1958. Translation by H. Rackham. Original text dates back to 77 A.D.

[48] R. B. Stull. *An Introduction to Boundary Layer Meteorology.* Kluwer Academic Publishers, Norwell, MA, 1988.

[49] D. Tabor. Babylonian lecanomancy: An ancient text on the spreading of oil on water. *J. Colloid Interface Sci.*, 75:240–245, 1980.

[50] M. Van Den Tempel and R. P. Van de Riet. Damping of waves by surface-active materials. *J. Chem. Phys.*, 42:2769–2777, 1965.

[51] G. Tryggvason, J. Abdollahi-Alibeik, W. W. Willmarth, and A. Hirsa. Collision of a vortex pair with a contaminated free surface. *Phys. Fluids*, A4:1215–1229, 1992.

[52] W. T. Tsai and D. K. P. Yue. Effects of soluble and insoluble surfactant on laminar interactions of vortical flows with a free surface. *J. Fluid Mech.*, 289:315–349, 1995.

[53] J. D. A. Walker, C. R. Smith, A. W. Cerra, and T. L. Doligalski. The impact of a vortex ring on a wall. *J. Fluid Mech.*, 181:99–140, 1987.

[54] H. T. Wang and R. I. Leighton. Direct calculation of the interaction between subsurface vortices and surface contaminants. In *Proc. 19th Intl. Conf. Offshore Mechanics and Arctic Engineering*, pages 271–277, Houston, TX, 1990.

[55] A. Weigand and M. Gharib. Turbulent vortex ring/free surface interaction. *J. Fluids Engrng.*, 117:374–381, 1995.

[56] C. E. Willert. *The interaction of modulated vortex pairs with a free surface.* PhD thesis, University of California, San Diego, 1992.

[57] C. E. Willert and M. Gharib. Digital particle image velocimetry. *Exps. Fluids*, 10:181–193, 1991.

[58] D. Yu and G. Tryggvason. The free-surface signature of unsteady, two-dimensional vortex flows. *J. Fluid Mech.*, 218:547–572, 1990.